2002-11

Applied Computational Electromagnetics Society Journal / Volume 17, Number 3

Elsherbeni, Atef Z.

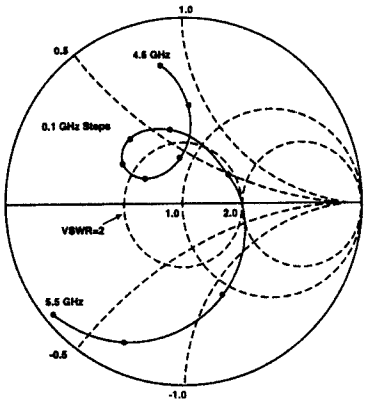

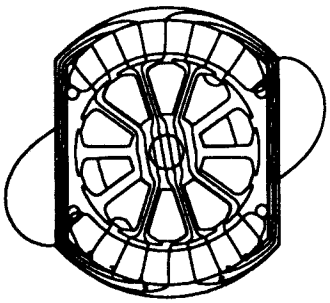

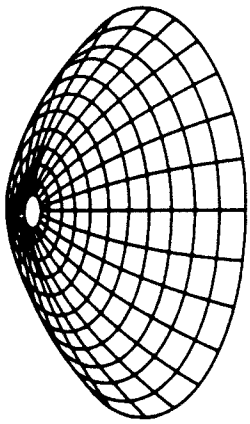

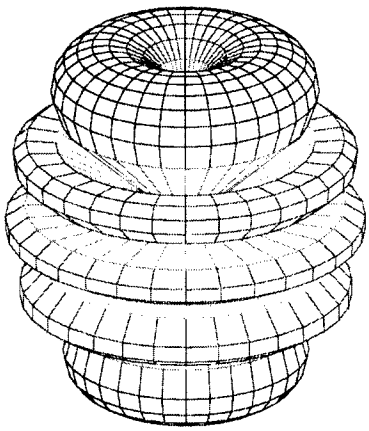

Applied Computational Electromagnetics Society Journal

Editor-in-Chief
Atef Z. Elsherbeni

November 2002
Vol. 17 No. 3
ISSN 1054-4887

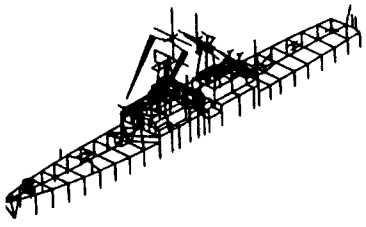

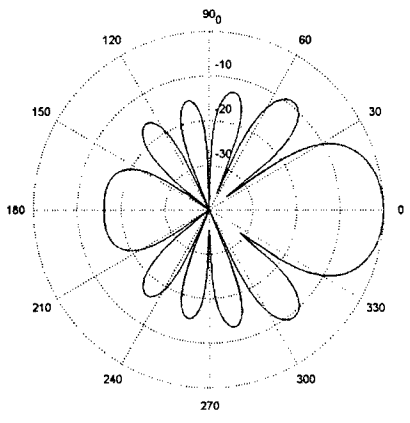

GENERAL PURPOSE AND SCOPE: The Applied Computational Electromagnetics Society *(ACES)* Journal hereinafter known as the ***ACES Journal*** is devoted to the exchange of information in computational electromagnetics, to the advancement of the state-of-the art, and the promotion of related technical activities. A primary objective of the information exchange is the elimination of the need to "re-invent the wheel" to solve a previously-solved computational problem in electrical engineering, physics, or related fields of study. The technical activities promoted by this publication include code validation, performance analysis, and input/output standardization; code or technique optimization and error minimization; innovations in solution technique or in data input/output; identification of new applications for electromagnetics modeling codes and techniques; integration of computational electromagnetics techniques with new computer architectures; and correlation of computational parameters with physical mechanisms.

SUBMISSIONS: The ***ACES Journal*** welcomes original, previously unpublished papers, relating to applied computational electromagnetics. Typical papers will represent the computational electromagnetics aspects of research in electrical engineering, physics, or related disciplines. However, papers which represent research in applied computational electromagnetics itself are equally acceptable.

Manuscripts are to be submitted through the upload system of ***ACES*** web site http://aces.ee.olemiss.edu See "Information for Authors" on inside of back cover and at ***ACES*** web site. For additional information contact the Editor-in-Chief:

Dr. Atef Elsherbeni
Department of Electrical Engineering
The University of Mississippi
University, MS 386377 USA
Phone: 662-915-5382 Fax: 662-915-7231
Email: atef@olemis.edu

SUBSCRIPTIONS: All members of the Applied Computational Electromagnetics Society who have paid their subscription fees are entitled to receive the ***ACES Journal*** with a minimum of three issues per calendar year and are entitled to download any published journal article available at http://aces.ee.olemiss.edu.

Back issues, when available, are $15 each. Subscriptions to ***ACES*** is through the web site. Orders for back issues of the ***ACES Journal*** and changes of addresses should be sent directly to ***ACES*** Executive Officer:

Dr. Richard W. Adler
ECE Department, Code ECAB
Naval Postgraduate School
833 Dyer Road, Room 437
Monterey, CA 93943-5121 USA
Fax: 831-649-0300
Email: *rwa@attglobal.net*

Allow four week's advance notice for change of address. Claims for missing issues will not be honored because of insufficient notice or address change or loss in mail unless the Executive Officer is notified within 60 days for USA and Canadian subscribers or 90 days for subscribers in other countries, from the last day of the month of publication. For information regarding reprints of individual papers or other materials, see "Information for Authors".

LIABILITY. Neither ***ACES***, nor the ***ACES Journal*** editors, are responsible for any consequence of misinformation or claims, express or implied, in any published material in an ***ACES Journal*** issue. This also applies to advertising, for which only camera-ready copies are accepted. Authors are responsible for information contained in their papers. If any material submitted for publication includes material which has already been published elsewhere, it is the author's responsibility to obtain written permission to reproduce such material.

APPLIED COMPUTATIONAL ELECTROMAGNETICS SOCIETY JOURNAL

Editor-in-Chief
Atef Z. Elsherbeni

November 2002
Vol. 17 No. 3

ISSN 1054-4887

The ACES Journal is abstracted in INSPEC, in Engineering Index, and in DTIC.

The first, fourth, and sixth illustrations on the front cover have been obtained from the Department of Electrical Engineering at the University of Mississippi.

The third and fifth illustrations on the front cover have been obtained from Lawrence Livermore National Laboratory.

The second illustration on the front cover has been obtained from FLUX2D software, CEDRAT S.S. France, MAGSOFT Corporation, New York.

THE APPLIED COMPUTATIONAL ELECTROMAGNETICS SOCIETY

JOURNAL

Vol. 17 No. 3 November 2002

TABLE OF CONTENTS

USING ADAPTIVE ESTIMATION TO MINIMIZE THE NUMBER OF SAMPLES NEEDED TO DEVELOP A RADIATION OR SCATTERING PATTERN TO A SPECIFIED UNCERTAINTY

Edmund K. Miller, Los Alamos National Laboratory (retired)
3225 Calle Celestial
Santa Fe, NM 87506-1213
ekmiller@prodigy.net

ABSTRACT

Obtaining far-field patterns in electromagnetics or acoustics, although generally not as computationally expensive as solving for the sources induced on an object, can none-the-less at times be a substantial fraction of the overall computer time required for some problems. This can be especially the case in determining the monostatic radar cross section of large objects, since the current distribution must be computed for each incidence angle, or when computing the radiation patterns of large reflector antennas using physical optics. In addition, when employing the point sampling and linear interpolation of the far field that is most often used to develop such patterns, it can be necessary to sample very finely in angle to avoid missing fine details such as nulls. A procedure based on model-based parameter estimation is described here that offers the opportunity of reducing the number of samples needed while developing an easily computed and continuous representation of the pattern. It employs windowed, low-order, overlapping fitting models whose parameters are estimated from the sparsely sampled far-field values. The fitting models themselves employ either discrete-source approximations to the radiating currents or Fourier models of the far field. For the cases investigated, as few as 1.5 to 2 samples per far-field lobe are found to be sufficient to develop a radiation-pattern estimate that is accurate to 0.1 dB, and 2.5 samples per lobe for a simple scatterer. In general, however, the sampling density is not determined by the lobe count alone, but by the effective rank of the field over the observation window, which in turn is a function of both the aperture size and the spatial variation of the source distribution within that aperture.

1. INTRODUCTION

An important goal of all numerical modeling is that of minimizing the number of samples needed of the relevant observables and equations so as to minimize the total computer operation count (OC) (or the computer cost) while achieving a desired accuracy, or equivalently reducing the uncertainty to a specified level, in the computed results. This topic is considered below in the context of computing radiation and scattering patterns in electromagnetics. The goal of particular interest here concerns minimizing the number of far-field pattern samples that are required to represent a radiation pattern and/or the number of incidence angles that are required to develop a monostatic backscatter radar-cross section (RCS) pattern. An added benefit of the procedure described below is that of obtaining an estimate of the uncertainty in the pattern that is developed.

The approach taken employs model-based parameter estimation (MBPE) [1]. This is a procedure that uses reduced-order, physically based fitting models (FMs) whose parameters are computed from samples of first-principles generating models (GMs) such as Maxwell s Equations. Computation of a FM sample is trivial compared with one evaluated from a GM for large, complex problems, potentially requiring orders-of-magnitude less computing time. This makes it possible, using the FM, to develop an essentially continuous representation of physical observables of interest as opposed to the pointwise characterization that is usually accepted when the cost of each GM evaluation is large. A list of acronyms used in the article follows the references.

2. BACKGROUND

One of the most frequently encountered problems in electromagnetic field computations is that of determining a radiation or scattering pattern from a current distribution(s) known over some surface. For antenna applications, usually a single current distribution is of interest, while for RCS computations, a new current distribution arises for each incidence angle of a plane-wave exciting field. In either case, the far field is usually needed at enough points to develop a smooth, in effect continuous, approximation of the overall pattern in one or more planes. The required number of radiation-pattern samples and resulting OC are proportional to the maximum body dimension, L, in the plane in which the pattern is being computed. Furthermore, the number of current samples on the surface, S, is itself is proportional to the body s surface area, i.e., $S \propto L^2$. As L, and therefore S, increases, the far-field computation can become a significant cost in obtaining radiation and scattering patterns. Thus, reducing the number of angle samples could be worthwhile in terms of reducing the overall computer cost of obtaining the radiation pattern(s) of a large antenna or RCS of a large scatterer

Some previous work by the author [2,3] and others [4,5] has described an approach that uses MBPE to decrease the number of samples that are needed to determine a far-field pattern. The work presented in [2,3], is briefly summarized and extended here, especially with respect to how the errors in the pattern can be estimated and controlled and how the pattern itself is modeled. Further examples of efficient pattern computation can be found in the work of Bucci and his various collaborators who have developed signal-processing-like techniques for computing far-field patterns [see for example 6, 7, and 8].

3. CHOOSING THE QUANTITY TO MODEL

Estimating a far-field pattern using MBPE requires choosing the kind of reduced-order FM that is to be used and to what observable that FM is to be applied. Two obvious choices for minimizing the number of pattern samples or incidence angles are available: 1) to model the current distribution; or 2) to model the far-field pattern. Furthermore, there are two ways in which the current distribution itself might be modeled. These various choices are briefly summarized below.

3.1 Modeling a Current (or Aperture) Distribution

The two approaches to be discussed here for modeling the current (or aperture) can be best described as Discrete-Source Approximations (DSAs). The current over the surface of the object under consideration or field over an aperture is replaced by a

linear array of discrete, or point, sources aligned in space as is described below. (Other point-source geometries might also be used; attention is limited here to a linear geometry). The parameters of the DSA model are obtained by fitting it to far-field samples obtained from the usual integration of the actual current distribution. The DSA is then used to approximate the pattern between these samples to thereby obtain a continuous estimate of the pattern without requiring additional current integrations.

3.1.1 Using A Prony Model

Prony s method (or its equivalent) can be used for the DSA computation, using as a FM [9]

$$F(\theta)=\sum_{\alpha=1}^{P} S_\alpha e^{ikd_\alpha \cos(\theta)} \tag{1}$$

which involves P point sources of strengths S_α located at positions d_α along the axis of the DSA˚ array, with θ the angle to the far field measured from that axis. There being 2N unknown parameters in Eq. 1, the Prony DSA (PDSA) thus requires 2N far-field samples of the actual pattern. Furthermore, these 2N samples need to be spaced uniformly in cos(θ), a feature that makes PDSA less suitable for the adaptive-sampling approach described next. A possible advantage, however, of finding the locations of the discrete sources is the possibility of developing an approximate image of the source whose far field is being sampled.

There are two different candidate DSA geometries that might be considered. In the first, shown in Fig. 1a, the DSA axis is fixed and a sequence of angle windows are rotated about this axis over the complete range of observation angles of interest. In the second, shown in Fig. 1b, the DSA axis is itself rotated to be perpendicular to the angle that defines the midpoint of each angle window used for the successive DSA computations. Note that L varies in proportion to the length of the object as seen from the center of the observation window when using the approach of Fig. 1b whereas L is fixed at the maximum linear dimension of the object in the observation plane for approach 1a.

3.1.2 Using A Specified DSA

The specified DSA (SDSA) model is the same as Eq. 1 except that, since the source locations are now specified, only the N source strengths S_α are unknowns. As for the Prony DSA, samples of the actual far-field are used to obtain the discrete-source strengths. In contrast to the Prony model, however, the pattern samples are not constrained in their placement but can be arbitrarily located in angle and only N are needed, two distinct over the Prony model. For the SDSA results presented here, the sources are equally spaced along the array axis, with the source numbers 1 and N located at the ends of the aperture L using the configuration shown in Fig. 1a. As the order, i.e., number of sources used in a particular SDSA FM, is increased, the source spacing is therefore systematically decreased in proportion to the number of sources that are used.

3.2 Modeling the Pattern

An alternative to using a DSA for the pattern estimation is to model the pattern itself, using a Fourier series, an approach denoted as the Fourier Series Pattern Model (FSPM). In this case the FM can be developed as [2]

$$F(\theta)=\sum_{\alpha=S}^{F} R_\alpha e^{i\alpha\theta}+\sum_{\alpha=S'}^{F} R'_{-\alpha} e^{-i\alpha\theta} \tag{2}$$

where we set F equal to Int(L + 1), with Int(X) denoting the value of X rounded off to the nearest lower integer. Also, 2F - S - S = N with N the total number of terms in the FM, S † S † S + 1, and R_α and $R_{-\alpha}$ are the amplitudes of the positive and

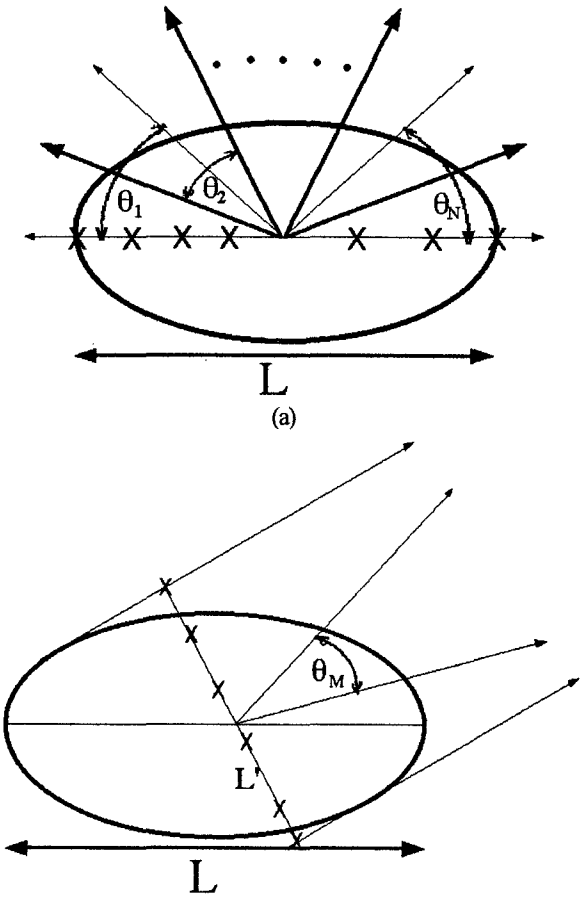

Figure 1. Two ways of implementing the Discrete-Source Array Fitting Model. In (a) the sampling window (denoted by alternately light and heavy lines) rotates in angle about the long axis of the object while the DSA FM axis remains fixed along which the discrete sources are located. In (b), on the other hand, the sampling aperture L' is rotated with respect to the long axis of the object and the sampling window is bisected by a line perpendicular to it. For the case of the PDSA, an N-source FM requires a minimum of 2N field samples. Both the source locations (indicated by the X's) and their strengths are determined by sampling the far field as a function of cos(θ), where generally the sources will be non-uniformly spaced. Alternatively, for the SDSA used to obtain the results presented here, the configuration (a) was used with N sources uniformly spaced along the array axis, thus requiring only N field samples for computation of their strengths.

negative modes respectively. As for the specified DSA, N far-field samples are required to quantify the parameters of the FSPM. Note that the Fourier approach yields estimates of the far-field Fourier components directly, as contrasted with either of the DSA FMs where the source strengths, and locations as well for the PDSA, are the parameters being computed. Ultimately, however, the differences between the SDSA and the FSPM are rather slight, differing most in the former having an observation-angle dependence given by exp[ikdcos(θ)] while the latter depends on exp(iαθ).

3.3 Adaptive Estimation Using Windowed, Overlapping Fitting Models

To be effectively implemented, any adaptive numerical procedure requires an error estimate. For the specific problem of adaptive pattern estimation, the error estimate is used to determine whether a given FM is accurate enough, and if not, where in angle a new sample should be located. Various FM configurations might be considered in this application. For example, a single FM might be used to span the entire angle window of interest with an initial set of sample angles, S, chosen for GM evaluation. A subset of these GM samples, S-1, could be used to obtain the S-1 parameters of FM(S-1) while all S GM samples could be similarly used to find the S parameters of FM(S). These two FMs could then be sampled more finely, by a factor of 10 or so, in angle than was used for the initial GM sampling, with the difference between them serving as an error measure. If the error measure exceeds the allowable uncertainty specified by the modeler, the S+1 th GM sample would be added at the angle where the difference between FM(S-1) and FM(S) is greatest. The parameters of FM(S+1) could then be computed and the difference between FM(S) and FM(S+1) obtained. The process would be systematically continued until the maximum difference between FM(S+k-1) and FM(S+k) satisfies the uncertainty specification, with S+k the total number of GM samples required. The initial number of GM samples to be used, S, would be chosen to be proportional to the number of pattern lobes expected over the observation window.

Using a single FM to cover an entire pattern would generally not be the best approach, however, partly due to the growing cost of the FM computation itself, but more importantly due to the fact that the condition number of the data matrix needing solution for the FM parameters may increase unacceptably, especially for a large number of pattern lobes. Instead, as is done here, a number of windowed, lower-order (i.e., fewer parameters) overlapping FMs are used. Each FM shares two or more GM samples with its neighbors, as is illustrated conceptually in Fig. 2 where there are a total of N FMs. As above, after their parameters have been evaluated, the FMs are evaluated more finely in angle than was the GM pattern initially, and the differences between the sets of overlapping FMs are computed. A new GM sample then is added where the maximum difference between all sets of overlapping FMs is found to occur. The respective parameters of the affected FMs (i.e., those whose windows contain the new sample angle) are then updated, with the process of computing FM differences and new GM samples continuing until the specified uncertainty is satisfied over the entire pattern window.

An appropriate choice for the number of FMs for a given problem might require some experimentation. If it s desired to keep the order of all FMs below some specified value, then based on the computer experiments done in getting the results presented below, each FM should have an angle window that spans just a few pattern lobes, say three or four at most. The number of lobes to be expected can generally be estimated from the size of the aperture whose pattern is being modeled. However, it may happen that adding a new GM sample to a FM causes its to rank exceed some specified limit. By dividing such a FM into two lower-order, overlapping ones, the problem of excess FM rank can be avoided and the initial number of FMs will not be so important.

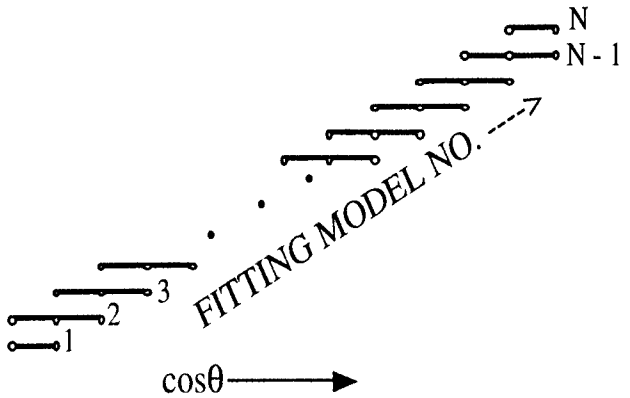

Figure 2. A conceptual illustration of the use of overlapping fitting models for adaptive sampling of a far-field pattern. The horizontal lines indicate the angular extent of each FM with the open circles showing where the pattern (or GM) is initially sampled. In this particular case, all interior FMs begin with three GM samples while those at either end use only two, for a total of N + 1 starting samples. Additional GM samples are systematically located where the maximum difference occurs between two overlapping FMs until a specified convergence criterion has been satisfied. Only two FMs overlap in any of the observation windows here, but other overlap arrangements could be used as well.

3.4 Specification of the Fitting-Model Error and Computing the Final Pattern Estimate

In contrast to specifying a fixed FM difference, or fitting-model error (FME), between overlapping FMs as was done in [2,3], the maximum FME can also be scaled relative to how the magnitudes of the far-field samples vary. For example, as the magnitude decreases the FME might be proportionately increased to accommodate the fact that side-lobe maxima may not be needed to the same accuracy as the main lobe. In the results to follow, the maximum permitted FME at the observation angle θ is given by

$$\mathrm{FME}(\theta) = A_1 + A_2\left[\left|\mathrm{GM}(\theta_{max}) - \frac{1}{M}\sum_{\alpha=1}^{M}\mathrm{FM}_\alpha(\theta)\right|\right] \tag{3}$$

where A_1 and A_2 are specified parameters, $\mathrm{GM}(\theta_{max})$ is the maximum value of the pattern being modeled, and $\mathrm{FM}_\alpha(\theta)$ is the value of the a th FM at θ where a total of M FMs overlap. The parameter A_1 determines the maximum acceptable FME in the vicinity of the peak(s) of the GM. The parameter A_2 increases the allowable FME in proportion to the decrease in the FM values relative to $\mathrm{GM}(\theta_{max})$. For the results that follow, the nominal values for A_1 and A_2 were 0.1 and 0.05 dB, respective-

ly, but FME(θ) limited to a maximum value of 3 dB. There are many possible variations that might be used for setting the acceptable error or uncertainty, among which would be relaxing the desired accuracy in certain angular regions or increasing it in others consistent with the requirements of a particular application.

The final pattern estimate is then obtained by computing the average of the successively overlapping FMs as the observation angle is scanned over the angle pattern. Thus, for M overlapping FMs at angle θ we would have

$$F_{ave,M}(\theta) = \frac{1}{M}[F_i(\theta) + F_{i+1}(\theta) + \cdots + F_{i+M-1}]. \quad (4)$$

For the results presented below, M = 2 was used.

Note that in addition to controlling the adaptation process, the error specification provides a measure of the uncertainty in the average FM values of Eq. 4. Since Eq. 3 gives the maximum variation permitted between the FMs that overlap at a given angle, it s proposed that

$$F_{ave,M\pm}(\theta) = F_{ave,M}(\theta) \pm \frac{1}{2}FME(\theta) \quad (5)$$

will yield realistic upper and lower error-bound estimates for the average pattern values. That Eq. 5 does indeed provide a realistic error bound relative to the FM estimates of GM is demonstrated in the following examples.

It s worth emphasizing that, in contrast to using an entire-domain basis for the far field, cylindrical- or spherical-wave expansions, for example, the windowed approach employed here together with discrete point sources can be applied to smaller, or limited, angular sectors with no computational penalty. Also observe that in implementing the SDSA, angle sampling is done in terms of cos(θ) rather than θ. This is because the pattern lobes tend to be distributed uniformly in terms of the former variable.

To summarize then, the following steps are involved in the MBPE modeling of radiation and scattering patterns:

1) The quantity to be modeled, i.e., the source distribution or pattern itself, is first selected.

2) The total angle window over which the pattern is to be estimated is specified.

3) The number of pattern lobes, L, that are anticipated over the angle window of interest, considering the aperture size in wavelengths whose pattern is to be found, is estimated.

4) The number, N, of initial fitting models to be used then needs to be chosen. Choosing a value for N between L/2 and 2L/3, with L expressed in wavelengths, should provide a reasonable starting point, noting that the smaller the value of N that is used the larger will be the required FM order.

5) The configuration of the FM overlap then needs to be selected. This can be fairly flexible. Arranging each window to be half overlapped with its nearest neighbors seems to be a good choice. Note that using half-overlapped FMs leads naturally to a minimum of 3 initial GM samples per FM window as shown in Fig. 2.

6) Finally, the kind of FM error to be used and its numerical parameters, as in Eq. (3), must be specified.

4. USING THE SPECIFIED DISCRETE-SOURCE APPROXIMATION

In previous work [2,3] the FSPM approach was described and some initial results presented, demonstrating that the far-field pattern could be estimated to an amplitude uncertainty of 0.01 (about 0.05 dB) using only ~ 3 to 3.5 samples per lobe. Several results obtained using the alternate SDSA model are presented here together with an illustration of how the model performance depends on the uncertainty specification. The particular patterns used for testing the MBPE approach here were chosen as being representative of the kinds of patterns encountered in typical applications, as well as their having closed-form analytical expressions, except for the last example of the random-source array.

4.1 The Far Radiated Field of the Uniform Current Filament

The far field, $F(\theta)_{UCF}$, of a uniform current filament (or uniform aperture) is proportional to [10]

$$F(\theta)_{UCF} = L\frac{\sin[\pi L\sin(\theta)]}{\pi L\sin(\theta)} \quad (6)$$

where the filament length L is expressed in wavelengths and the observation angle θ is measured from the filament axis. A total of N = 13 FMs was used for an L = 20-wavelength UCF, arranged as shown in Fig. 2, with the parameters of Eq. 3 given by A_1 = 0.1 and A_2 = 0.05 dB. Thus, all FMs initially have three GM samples except for those on either end, which have only two. This results in each FM sharing two samples with its nearest neighbors except for those on the end, which overlap with one adjacent FM. Applying the SDSA to GM samples of Eq. 6 yields the results of Fig. 3, normalized to a maximum of 0 dB, where the upper and lower error-bound estimates for the pattern peaks, using Eq. 5, and the actual pattern from Eq. 6 are plotted. The actual pattern is seen to lie between the upper- and lower-bound peaks throughout the entire window. In Fig. 4 the average values of the overlapping FMs from Eq. 4, FM_{ave}, are compared with the actual pattern, where 34 of the 35 GM samples used for computing the final FM parameters are also shown. The maximum difference between the actual pattern and FM_{ave} is consistent with the error specification of Eq. 4 and the numerical values used for its parameters. With 35 samples needed to estimate a pattern having 20 lobes or maxima, 1.75 samples are required per lobe for the UCF.

The behavior of three different error measures for the L = 20 UCF is presented in Fig. 5 as a function of the number of GM samples used for computing the FM parameters. The upper plot on this graph shows the maximum difference between all pairs of the 13 finely sampled, overlapping FMs as a function of the number of GM samples used for their computation. The middle plot exhibits the difference between all pairs of overlapping FMs averaged over the angles they commonly sample. The bottom

plot displays the angle-averaged difference between FM_{ave} and the actual pattern, or the GM. Of these three, only the first two would be available in actual application since the GM samples needed to compute the last error measure would be limited to those available up to that point in the adaptation process. It s useful to include the latter error measure, however, as the difference between the FM_{ave} and the GM provides a reality check on the MBPE performance.

Observe that the difference between the overlapping FMs for this example always exceeds the corresponding FM_{ave} - GM difference. This shows that the FM-FM error measure provides a conservative, or high-side, estimate of the error (or uncertainty) in FM_{ave} relative to the true GM values. Note also that the maximum FM difference does not decline monotonically. This is because updating two FMs can at times increase the maximum differences that then results with their overlapping neighbors.

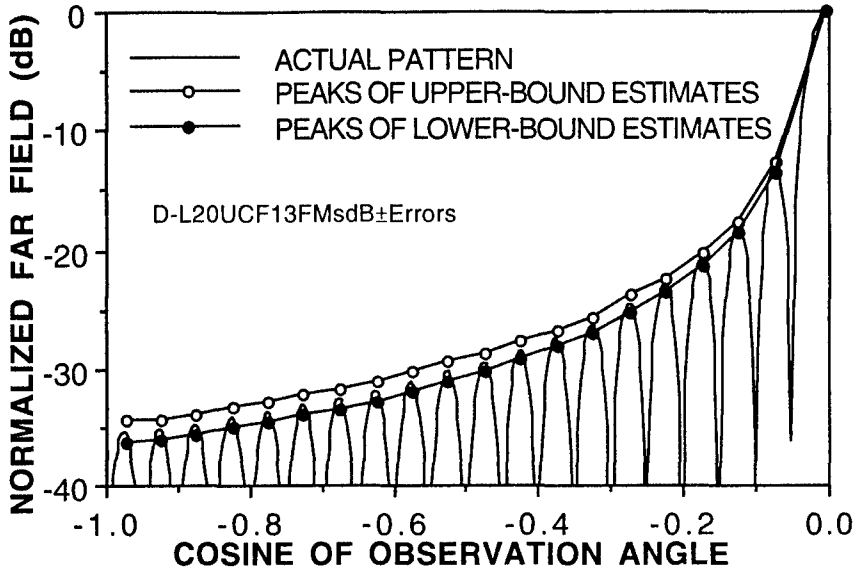

Figure 3. One quadrant of the normalized radiation pattern for the field of an L = 20 (wavelengths) UCF as obtained using the specified discrete-source approximation. The lower- and upper-bound peaks estimated from Eq. 5 are shown together with the actual pattern from Eq. 6. The pattern is cut-off at -40 dB to show the difference between the various plots more clearly.

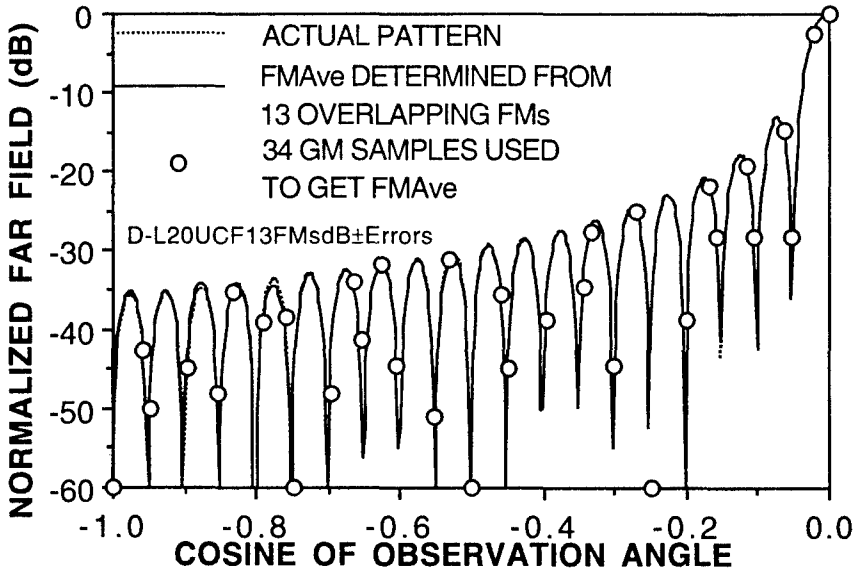

Figure 4. One quadrant of the normalized, actual field of the 20-wavelength UCF compared with FM_{ave}. The circles indicate 34 of the 35 GM samples computed from Eq. 6 (one is below -60 dB), that were used in the estimation process. Because the cosine-angle values used to obtain the average and actual patterns do not always precisely match those used to obtain the original GM samples, some of the latter do not coincide with the pattern plots.

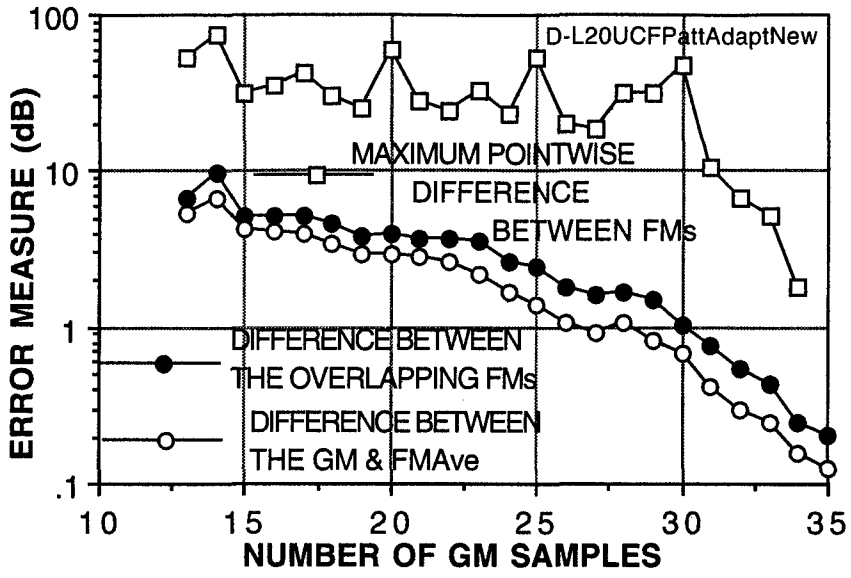

Figure 5. Three error measures discussed in the text for the UCF shown as a function of the number of GM samples used up to that point in the adaptation process over an observation window -90 to 0 deg, with the parameters in Eq. 3 given by A_1 = 0.1 dB and A_2 = 0.05 dB. The open squares denote the maximum pointwise difference between all pairs of overlapping FMs with the addition of a new GM sample. The closed and open circles exhibit the angle-averaged difference between the overlapping FMs and between the average FM and the GM itself. The fact that the latter is smaller than the former shows that the FM difference provides a conservative measure of the accuracy of FM_{ave}.

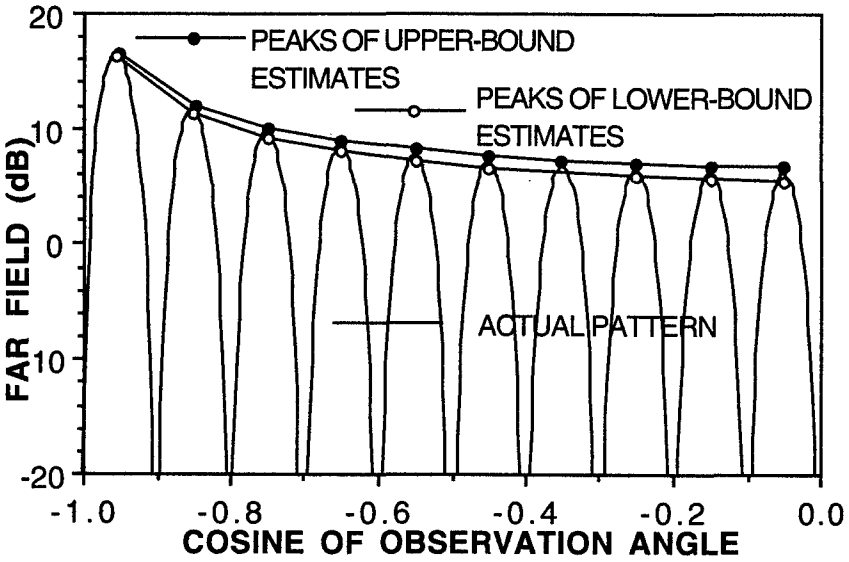

Figure 6. One quadrant of the normalized radiation pattern for the field of an L = 20 (wavelengths) SCF as obtained using the SDSA. The lower- and upper-bound peaks estimated from Eq. 5 are shown together with the actual field from Eq. 7. The pattern is plotted over a limited dB range to show the difference between the various plots more clearly.

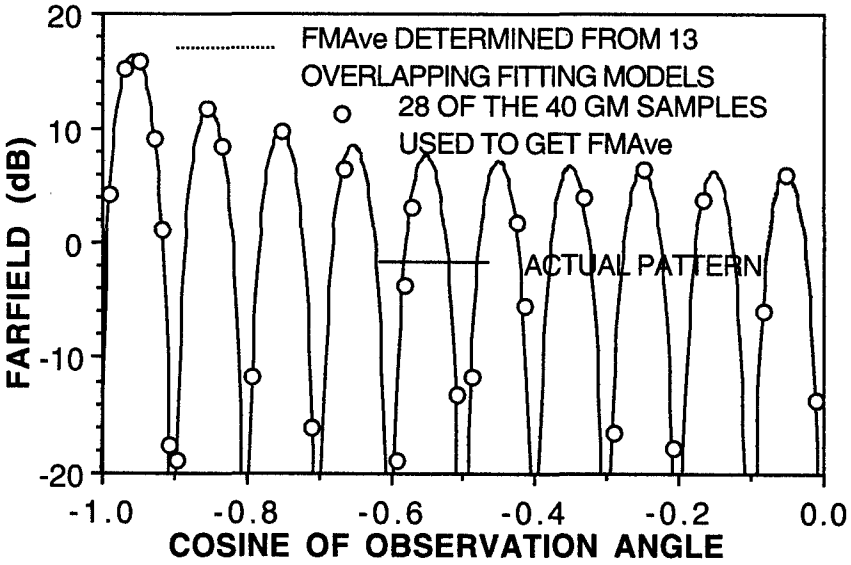

Figure 7. One quadrant of the actual field of the 20-wavelength SCF compared with FM_{ave}. The circles indicate 28 of the 40 GM samples, computed from Eq. 7, that were used in the estimation process.

4.2 The Far Radiated Field of the Sinusoidal Current Filament

The normalized far field of a center-fed sinusoidal current filament (SCF)°L wavelengths long is proportional to [10]

$$F_{SCF}(\theta) = \frac{\cos(\pi L\cos\theta) - \cos(\pi L)}{\sin\theta} \quad . \tag{7}$$

Application of adaptive MBPE to an L = 20-wavelength SCF using N = 13 overlapping FMs as shown in Fig. 2 leads to the upper- and lower-bound estimates for the far field shown together with the actual pattern in Fig. 6. Again, the actual field values are seen to lie between the bounding curves provided by MBPE adaptive sampling. A comparison of FM_{ave} with the actual pattern is presented in Fig. 7 where most of the 40 GM samples used for the FM computation are also shown (some fall below -20 dB). The actual and FM_{ave} curves are essentially graphically indistinguishable on the scale used. The 20-wavelength SCF has only 10 lobes rather than the 20 lobes of the 20-wavelength UCF over the same -1 to 0 cos(θ) interval, but requires 6 more unknowns to achieve the same estimation uncertainty, or 4 samples per lobe. This indicates that the number of GM samples needed to achieve a given pattern-estimation uncertainty is sensitive not only to the lobe structure of the pattern itself, but also to the spatial variation of the source distribution that produces that pattern.

4.3 The Far Field Scattered from a Thin, Circular Cylinder

The GM here is the approximate far, scattered field of a thin, circular cylinder L wavelengths long, which is proportional to [11]

$$RCS \propto F_{CYL}^2(\theta) = \left[\cos\theta_i \frac{\sin(2\pi L\sin\theta_i)}{2\pi L\sin\theta_i} \right]^2 \tag{8}$$

for which MBPE adaptive sampling produces the results shown in Figs. 8 and 9 for L = 10 wavelengths with 7 FMs being used. In contrast with an L-wavelength SCF, where the number of lobes over a -1 to 0 interval in cos(θ) is ~ L/2 and the UCF which has ~ L lobes over that same interval, the L-wavelength scatterer has ~ 2L lobes, 20 in this example. As for the previous cases, the FM_{ave}, as obtained from 48 GM samples, and a finely sampled GM plot for the scatterer are graphically indistinguishable. The number of samples required per lobe for the 10-wavelength cylinder scatterer is thus 2.4, greater than the 1.75 needed for the UCF even though their patterns are quite similar, as can be seen by comparing Figs. 4 and 9.

4.4 The Far Radiated Field of a Randomized Array of Point Sources

The last example considered here is a linear array of 21, isotropic point sources having random amplitudes varying between -1 and +1 and located randomly within a 10-wavelength aperture. Results for cos(θ) varying from -1 to 0 are shown in Figs. 10 and 11, again using 13 FMs. A total of 26 GM samples is needed to achieve the same specified estimation error as used for the previous cases. Since there are on the order of 8.5 maxima in the pattern, this works out to about 3 samples per lobe, midway between that required for the scatterer and the SCF. The number of samples needed per lobe or per wavelength of aperture to achieve the same specified estimation accuracy (as given by Eq. 3 with A_1 and A_2 0.1 dB and 0.05 dB, respectively) for the various sources considered here is summarized in Table I below.

5. CONCLUDING OBSERVATIONS CONCERNING ESTIMATION UNCERTAINTY AND SAMPLING

The preceding examples demonstrate that adaptive sampling of radiation and scattering patterns using MBPE with discrete-source-approximation FMs can be effective in not only reducing the number of samples needed to obtain a reduced-order, continuous representation of a pattern, but also in constraining the estimated pattern to satisfy an uncertainty specification. Some additional computations are included here to shed further light on the sampling requirements. The L = 20 UCF problem was repeated using A_1 = 0.05 and A_2 = 0 dB to reduce the estimation uncertainty to a smaller, and constant, value compared with the criterion used in obtaining the previous results. Using these coefficient values in the FME given by Eq. 3 results in a maximum acceptable difference between overlapping FMs, and hence, a maximum estimation error, of no more than 0.05 dB. This is much less than might normally be sought in practice but provides a more stringent test of the MBPE procedure. It should be noted that if the GM samples are of limited accuracy, for example being derived from a numerical first-principles model for a complex problem, then seeking an accuracy in the pattern estimate that the GM samples cannot provide might result in stagnating the estimation process, i.e., convergence may not occur. But when using an analytical expression for a pattern, as is done here, this will not be a problem. It s also worth noting that the variational relationship between the far fields and the sources that produce them results in errors in the latter not translating into comparable errors in the former.

Upon running the L = 20-wavelength UCF problem using these new values for the FME coefficients and plotting the same error measures as for Fig. 5, the results shown in Fig. 12 are obtained. Also included in Fig. 12 are lines of the form Aexp(-Bx) where x is the number of GM samples and A and B are best-fit parameters. It s interesting to see that the three best-fit lines are nearly parallel, with all decreasing exponentially as a function of the number of GM samples. This behavior is similar to the convergence of numerical solutions for various wire geometries as the number of unknowns in a moment-method solution is increased. A 0.1 dB in the angle-averaged FM difference and the difference between the FM_{ave} and the actual pattern is achieved using about 37 GM samples.

This computation was repeated for UCFs having lengths of L = 10, 15 and 25 wavelengths, yielding the results of in Fig. 13 where, for clarity, only the FM-FM differences are plotted. The data for each of these UCF°lengths are found to be fit comparably well by exponentials having different slopes. This is an expected result since the number of GM samples needed to achieve a given uncertainty for a specified source distribution is expected to be related to the number of pattern lobes which are, in turn, proportional to the aperture size. When the latter effect is removed by replotting the data of Fig. 13 as a function of the number of GM samples per wavelength of aperture, the results shown in Fig. 14 are obtained. The best-fit lines for the various

UCF lengths are nearly coincident, shifting to the left slightly with increasing L and exhibiting slopes that are within about 1.5%. A 0.1 dB angle-averaged FM difference is seen to require about 2 samples per wavelength of aperture.

Since a UCF L-wavelengths in extent produces L lobes per 90 deg in its pattern, this sampling density translates to about 2 samples per lobe as well. As can be deduced from Table I, it s clear that the far-field sampling density depends on more than just the lobe count in the pattern.

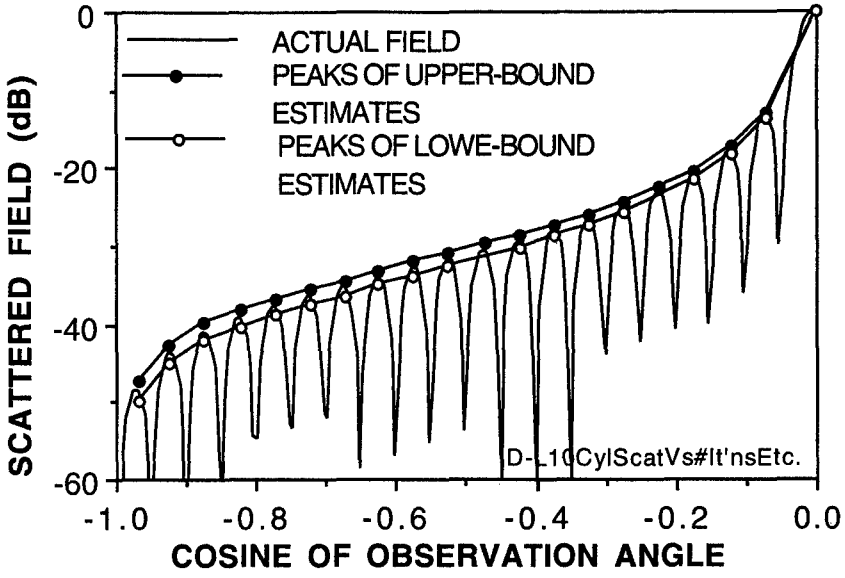

Figure 8. One quadrant of the normalized scattering pattern for the field of an L = 10 wavelengths thin cylinder as obtained using the SDSA. The lower- and upper -bound peak estimates of the far field from Eq. 5 are shown together with the actual field from Eq. 8.

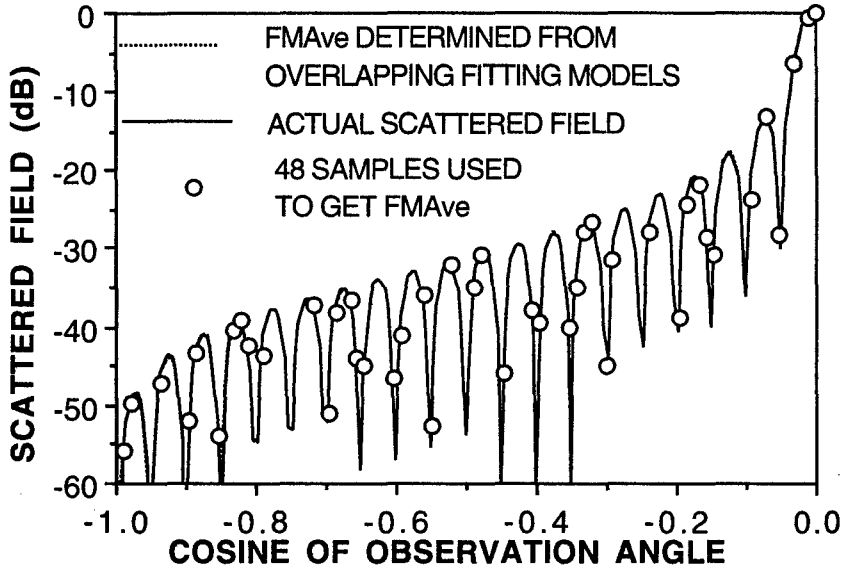

Figure 9. One quadrant of the actual scattered field of the 10-wavelength cylinder compared with FM_{ave}. The circles indicate some of the 48 GM samples, computed from Eq. 8, that were used in the estimation process.

How this sampling density might generalize to 2D or 3D source distributions needs to be considered. First note that the sampling density of 2 per wavelength of aperture for the UCF applies to a pattern symmetric about broadside where an angle-observation window of only 90 deg needs to be sampled. For a non-symmetric, but otherwise equivalent, linear source distribution this would then work out to 4 samples per wavelength since a far-field window of 180 deg would then need to be sampled. For a true 2D source whose pattern has to be sampled over 360 deg, this would imply that 8 samples per wavelength of its maximum linear aperture are needed to achieve a comparable pattern accuracy of 0.1 dB. This measure would seem to hold in planar cuts for the radiation patterns of 3D source distributions as well.

Results obtained for the cylinder scatterer indicate, on the other hand, that nearly 5 samples per wavelength of cylinder length are required for the same kind of pattern-estimation accuracy for a 90-deg sector of the scattered field to be estimated. Following the same line of reasoning as above for a general 2D scatterer, or for planar cuts of 3D objects, sampling over 360 deg can be estimated to require on the order of 20 samples per wavelength. One obvious question arises about why a greater sampling density is apparently needed for a scattering pattern as compared with a radiation pattern when the two are similar-appearing, as exhib-

ited by Figs. 4 and 9? Perhaps the answer is that for the latter situation a single current distribution produces the entire radiated field. For the former, on the other hand, the current distribution, being a function of the angle of incidence, changes with every viewing angle when determining the monostatic radar cross section.

It would also seem to follow then that the number of GM samples needed to achieve a specified estimation uncertainty must depend on both the aperture size and spatial variation of the source within it, a dependence that ultimately is exhibited by the pattern rank (R) or the number of degrees of freedom of the pattern, over the chosen observation window. As a specific example of how the source characteristics and aperture might influence the rank, consider an aperture L-wavelengths long having N point sources uniformly spaced within it.

For the simplest case of two point sources, as L is increased, the number of pattern lobes over 360 deg in an observation plane containing the sources will be of order 4L. However, R, as determined by eigenvalue analysis of the data matrix that arises when using Prony s method remains fixed at two when L exceeds 0.5, regardless of how large the aperture is made and how many lobes are in the pattern. On the other hand, if L is fixed and the number of point sources is systematically increased, R will increase proportionately until N > 2L whereupon R remains fixed at ~ 2L since only about 2 source/wavelength can be resolved in the far field. Because it can model such point-source arrays, a Prony-based procedure can exploit the reduced rank of such special problems, but the discrete-source approximation and a Fourier model of the far field are not as well-suited for doing so. Generally speaking, with everything else being equal, the best pattern estimator would be one for which the number of GM samples can be reduced to as close to R as possible. More investigation is needed to settle these issues, and to generalize the results beyond the simple cases considered here.

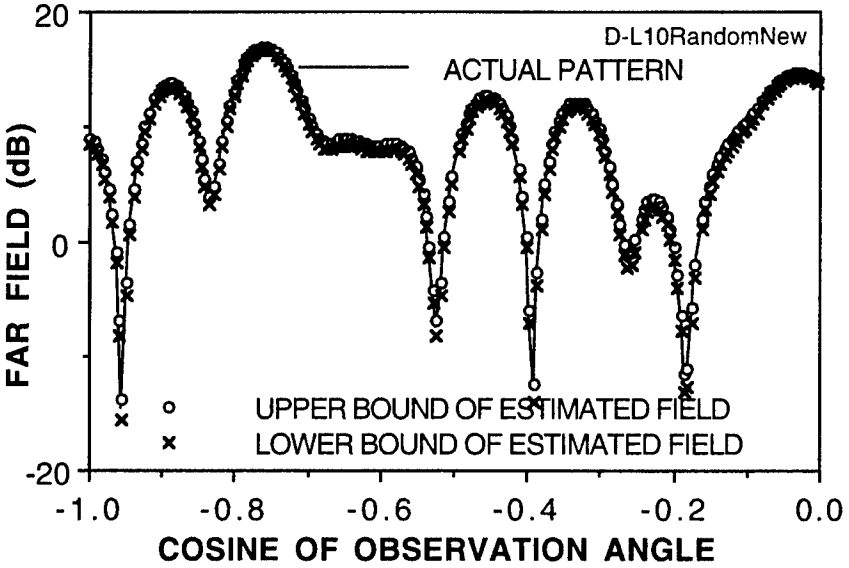

Figure 10. One quadrant of the radiation pattern for the field of 21 isotropic point sources having random amplitudes between -1 and + 1 and randomly located along a an L = 10 wavelengths linear array. Upper-bound estimates of the pattern are shown by the x's and the lower-bound estimates by the open circles with the actual pattern shown by the solid line.

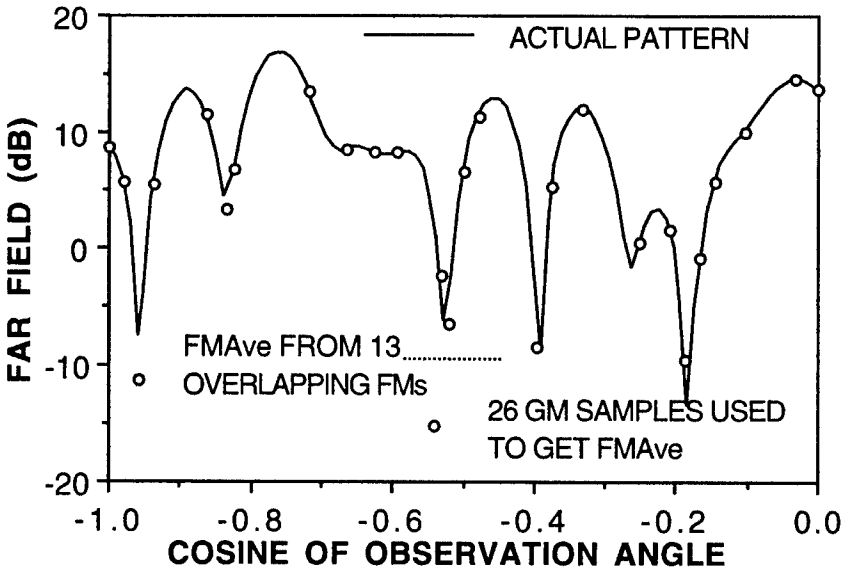

Figure 11. The actual pattern of 21 isotropic sources having random amplitudes and located at random positions along a 10-wavelength aperture compared with FM_{ave}. The circles indicate the 26 GM samples used in the estimation process.

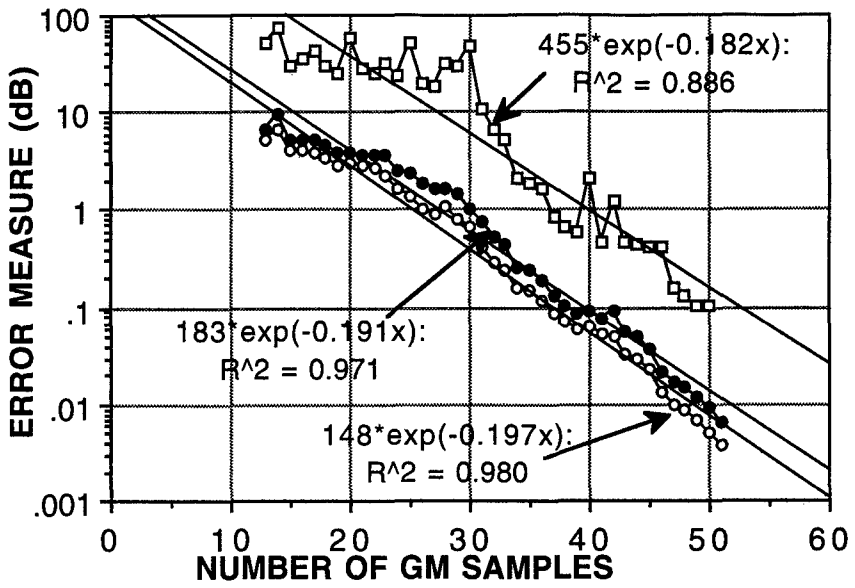

Figure 12. The three error measures shown in Figure 6 are plotted here for the 20-wavelength UCF but with $A_1 = 0.05$ and $A_2 = 0$ in Eq. 3 to obtain an estimate that is both more accurate and remains constant over the dynamic range covered by the pattern sampled in a -90 to 0 deg observation window. A best-fit straight line is computed for all three, where R^2 is the square of the correlation coefficient. All three best-fit lines are seen to be nearly parallel on this log-linear plot, being well-described as exponential functions of the number of GM samples.

Figure 13. The angle-averaged FM-FM differences for a UCF varying from 10 to 25 wavelengths using $A_1 = 0.05$ and $A_2 = 0$ in Eq. 3 yields the results shown here, again for a -90 to 0 deg observation window. Best-fit straight lines are also shown together with their respective correlation coefficients. The constants in the exponentials for the best-fit lines are seen to decrease with increasing filament length. The exponential decrease of the error measures as the number of GM samples increases is a very beneficial attribute of a numerical process.

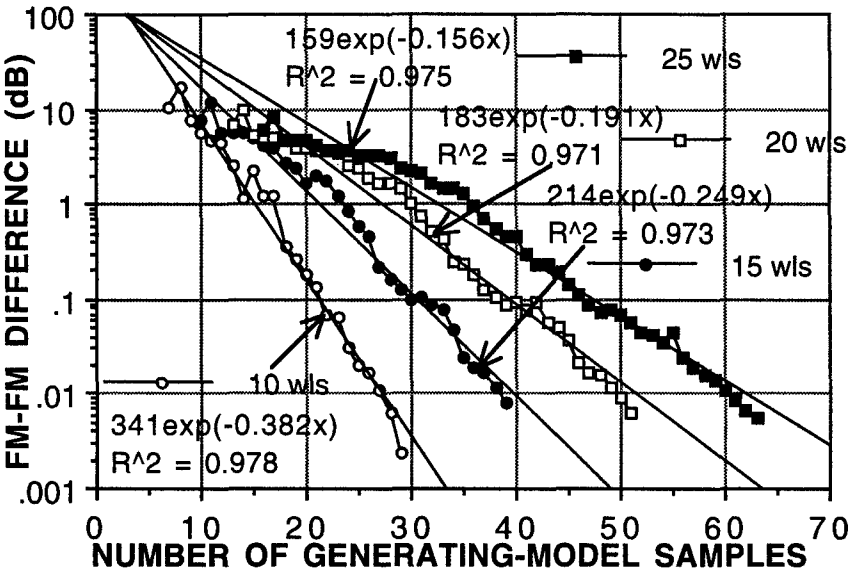

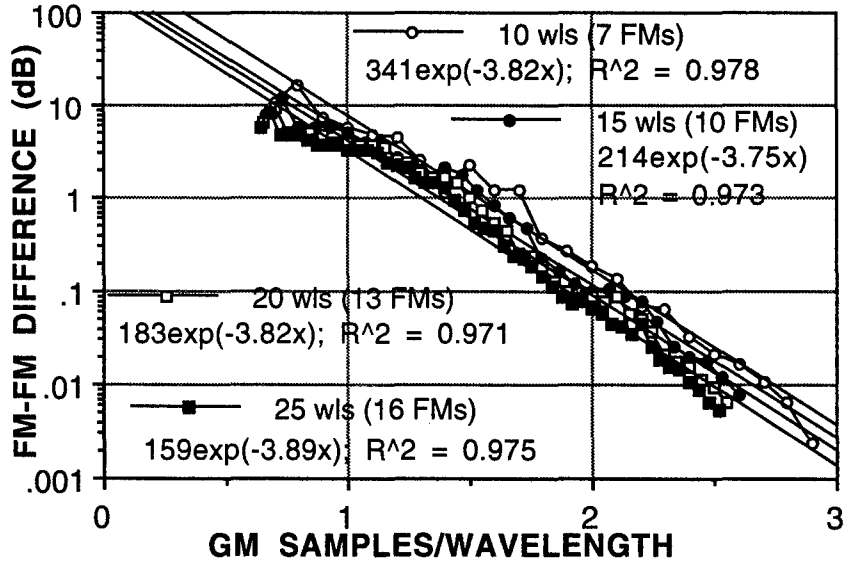

Figure 14. Upon replotting the results of Fig. 13 but with the number of GM samples/wavelength as the independent variable, the best-fit angle-averaged FM-FM differences become nearly coincident. These results show that for this particular case the number of GM samples needed for a specified angle-averaged FM difference in the pattern is linearly proportional to the filament length. They also show that the sampling density required for a given value of error measure decreases somewhat as the UCF increases in length.

TABLE I: FAR-FIELD SAMPLING REQUIRED OVER A 90-deg WINDOW FOR SOURCES TESTED USING $A_1 = 0.1$ AND $A_2 = 0.05$ dB in Eq. 3.

SOURCE TYPE TESTED	NUMBER OF SAMPLES	FAR-FIELD SAMPLES/ LOBE	FAR-FIELD SAMPLES/ WAVELENGTH OF APERTURE
20-WL SINUSOIDAL CURRENT FILAMENT	40	4	2
10-WL RANDOMIZED ARRAY	26	3	2.6
10-WL CYLINDER SCATTERER	48	2.4	4.8
20-WL UNIFORM CURRENT FILAMENT	35	1.75	1.75

5. REFERENCES

1. E. K. Miller (1995), Model-Based Parameter Estimation in Electromagnetics: I--Background and Theoretical Development, *Applied Computational Electromagnetics Society Newsletter*, 10 (3), November, pp. 40-63; (1996), II--Applications to EM Observables, 11 (1), pp. 35-56; (1995), III--Applications to EM Integral Equations, *Applied Comptational Electromagnetics Society Journal*, 10 (3), pp. 9-29.

2. E. K. Miller (1998), Computing Radiation and Scattering Patterns Using Model-Based Parameter Estimation, *IEEE AP-S International Symposium*, Renaissance Waverly Hotel, Atlanta, GA, June 21-26, pp. 66-69.

3. E. K. Miller and T. K. Sarkar (1999), An Introduction to the Use of Model-Based Parameter Estimation in Electromagnetics, in *Review of Radio Science*, 1999 URSI General Assembly, pp. 139-174.

4. R. J. Allard, D. H. Werner, J. S. Zmyslo, and P. L. Werner, "Spectral Domain Interpolation of Antenna Radiation Patterns Using Model-Based Parameter Estimation and Genetic Algorithms", *Proceedings of the 14th Annual Review of Progress in Applied Computational Electromagnetics (ACES)*, Vol. 2, pp. 964-971, 1998.

5. D. H. Werner and R. J. Allard, "The Simultaneous Interpolation of Antenna Radiation Patterns in Both the Spatial and Frequency Domains Using Model-Based Parameter Estimation", *IEEE Transactions on Antennas and Propagation*, Vol. 48, No. 3, pp. 383-392, 2000.

6. O. M. Bucci and G. Franceschetti, On the Degrees of Freedom of Scattered Fields, *IEEE Antennas and Propagation Society Transactions*, Vol. 37, No. 7, pp. 918-929, July 1989.

7. O. M. Bucci, C. Gennarelli and C. Savarese, Optimal Interpolation of Radiated Fields Over a Sphere, *IEEE Antennas and Propagation Society Transactions*, Vol. 39, No. 11, pp. 1633-1643, November 1991.

8. O. M. Bucci, C. Gennarelli and C. Savarese, Representation of Electromagnetic fields Over Arbitrary Surfaces by a Finite and Nonredundant Number of Samples, *IEEE Antennas and Propagation Society Transactions*, Vol. 46, No. 3, pp. 315-359, March 1998.

9. R. W. Hamming, *Numerical Methods for Scientists and Engineers*, Dover Publications, Inc., New York, 1962.

10. C. A. Balanis, *Antenna Theory: Analysis and Design*, Harper & Row, Publishers, New York, 1982.

11. E. G. Knott, J. F. Shaeffer and M. T. Tuley, *Radar Cross Section*, 2nd Edition, Artech House, Boston, 1993.

ACRONYMS

DSA--Discrete-Source Approximation
FM--Fitting Model
FME--Fitting-Model Error
FSPM--Fourier Series Pattern Model
GM--Generating Model
MBPE--Model-Based Parameter Estimation
OC--Operation Count
PDSA--Prony Discrete-Source Approximation
R--Rank
RCS--Radar Cross Section
SCF--Sinusoidal Current Filament
SDSA--Specified Discrete-Source Approximation
UCF--Uniform Current Filament

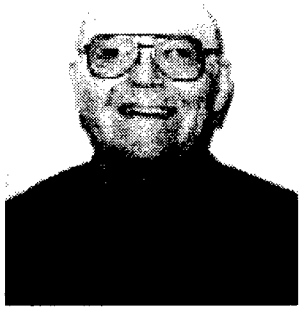

Edmund K. Miller earned a B.S.E.E. at Michigan Technological University and an M.S.Nuc.E., an M.S.E.E. and a Ph.D.E.E. at the University of Michigan. His work experience includes the Radiation and High Altitude Engineering Laboratories of the U. of Michigan, Lawrence Livermore and Los Alamos National Laboratories, and MBAssociates, Rockwell International Science Center and General Research Corporation. He has been a physics instructor at Michigan Technological University, a Regents-Distinguished Professor at the University of Kansas and a Stocker Visiting Professor at Ohio University. He has also been a Guest Scientist at the University of Pretoria and University of Stellenbosch, both in the Republic of South Africa. Dr. Miller is presently actively retired in Santa Fe, NM.

He has served two terms on IEEE AP-S AdCom and has been an AP-S Distinguished Lecturer. He was elected IEEE Fellow in 1994 and received the IEEE Third Millennium Medal in 2000. He was the recipient (with co-authors) of the 1988 Best Paper Award from the IEEE Education Society. He has served on the Editorial Board of IEEE student magazine *POTENTIALS* since 1985 and was its Editor 1992-1995. Dr. Miller served as the first President of ACES and two terms on the ACES Board of Directors. His primary interests remain focused on computational electromagnetics, applied signal processing, visual electromagnetics, and promoting the incorporation of accuracy statements in CEM numerical results.

SOLUTION OF THE GENERAL HELMHOLTZ EQUATION STARTING FROM LAPLACE'S EQUATION

Tapan K. Sarkar and Young-seek Chung
Department of Electrical Engineering and Computer Science
121 Link Hall
Syracuse University
Syracuse, New York 13244-1240.
Phone: 315-443-3775, Fax: 315-443-4441.
Email: tksarkar@syr.edu, Homepage: http://web.syr.edy/~tksarkar

Magdalena Salazar Palma
Grupo de Microondas y Radar, Dpto. Senales, Sistemas y Radiocomunicaciones
ETSI Telecomunicacion, Universidad Politecnica de Madrid
Ciudad Universitaria, 28040 Madrid, Spain.
E-mail: salazar@gmr.ssr.upm.es

ABSTRACT: In this paper we illustrate how to solve the general Helmholtz equation starting from Laplace's equation. The interesting point is that the Helmholtz equation has a frequency term whereas Laplace's equation is the static solution of the same boundary value problem. In this new formulation the frequency dependence is manifested in the form of an excitation. A new boundary integral method for solving the general Helmholtz equation is developed. This new formulation is developed for the two-dimensional Helmholtz equation with the method of moments Laplacian solution. The main feature of this new formulation is that the boundary conditions are satisfied independent of the region node discretizations. The numerical solution of the present method is compared with finite difference and finite element solutions of the same problem. Application of this method is also presented for the computation of cut-off frequencies for some canonical waveguide structures.

I. INTRODUCTION

The two dimensional Helmholtz's equation is an important equation to be solved in many numerical electromagnetics problems such as waveguide related problems and appears in a variety of physical phenomena and engineering applications, such as, acoustic radiation [1], heat conduction [2], and water wave propagation [3]. In semiconductor device modeling, Helmholtz's equation arises frequently as an intermediate step in the solution of the nonlinear Poisson's problem. To solve these problems diverse numerical methods have been reported which include finite difference [4], finite element [5], and boundary integral methods (BIM) [6-8]. Using these conventional methods, it has been found that fine grids and a large number of elements must be employed to get satisfactory accuracy [3]. This requires large computer core storage, and more computational time especially for the iteration scheme of the nonlinear Poisson's problem where the value at each grid point needs to be updated at each step of the iteration. Further, the BIM formulations are in most cases limited to homogeneous Helmholtz equation and tied closely to the particular problem at hand [6]. In this paper, a simple approach to solve the homogeneous and nonhomogeneous Helmholtz equations is proposed. The technique is based on the computation of Laplacian potential by the method of moments (MoM) [9], without resorting to different formulations using Hankel functions as it is commonly done in BIM [10]. Besides its generality to solve Laplace's, Poisson's, and Helmholtz's equations in one single code implementation, the present method will considerably reduce the number of domain grids compared to the finite difference methods and does not require any interpolation. The accuracy of the MOM solution from this new formulation will be compared with the solutions of fine difference method (FDM) and finite element method (FEM), using the ELLPACK implementation [4].

II. MATHEMATICAL FORMULATION

Consider the following two-dimensional elliptic equation for a smooth function Ψ defined in a 2-D region defined by $\Re$ which is bounded by a contour C so that

$$\nabla^2\Psi(x,y)+\lambda(x,y)\Psi(x,y)=F(x,y) \qquad (1)$$

where λ and F are known functions in the domain $\Re$. The general form of (1) includes, as specializations, the following cases:

1) Laplace's equation, with $\lambda = 0$ and $F = 0$
2) Poisson's equation, with $\lambda = 0$ and $F \neq 0$.
3) Helmholtz's equation, with $\lambda \neq 0$ and $F \neq 0$.

So only one general formulation addresses the solution to all of the three cases above. In addition we illustrate how to use the frequency independent solution of the Laplace's equation to solve the general Helmholtz equation. On the contour C the boundary condition can be of Dirichlet, Neumann, or mixed type, as given by the general form

$$\alpha\Psi + \beta\frac{\partial\Psi}{\partial n} = \gamma \tag{2}$$

where α, β, γ, are known spatial functions and $\partial\Psi/\partial n$ represents the normal derivative. It is implied that a consistent set of boundary conditions has been chosen for the problem.

The proposed scheme to solve the given boundary value problem starts by assuming the term $\lambda\Psi$ to be a known function, and including it with the given excitation function F, and thereby reducing (1) to the familiar Poisson's equation

$$\nabla^2\Psi(x, y) = -\Theta(x, y) \tag{3}$$

with

$$\Theta(x, y) = \lambda(x, y)\Psi(x, y) - F(x, y). \tag{4}$$

The solution to Poisson's equation in (3) can be expressed as

$$\Psi = \phi_h + \phi_p \tag{5}$$

where ϕ_h is the solution to the homogeneous Poisson's equation (Laplace's equation)

$$\nabla^2\phi_h = 0 \tag{6}$$

and ϕ_p is the particular integral, i.e.,

$$\nabla^2\phi_p = -\Theta(x, y) \tag{7}$$

Here we use the particular solution of the Poison's equation given by [12]

$$\phi_p(x, y) = \frac{1}{2\pi}\iint_{\Re}\Theta(x', y')\ell n\left(\frac{K}{\sqrt{(x-x')^2 + (y-y')^2}}\right)dx'dy' \tag{8}$$

where the spatial sets (x, y) and (x', y') denote the spatial coordinates of the field and source coordinates, respectively, and K is an arbitrary constant. Here, $\ell n(K)$ represents the value of the scalar potential ϕ at infinity for the two dimensional case. For the 3D case, this term does not exist, as the potential at infinity is zero. Hence the Green's function is simply 1/R instead of the natural log function. The value of the parameter K is chosen to be 100 for the 2-D problem as the reference potential at infinity is not zero but finite.

An expression similar to (8) can be derived to approximate the Laplacian potential ϕ_h. The potential ϕ_h can be assumed to be produced by some equivalent sources consisting of electrical charges, σ located on the contour C [12]. Then the potential ϕ_h at any point (x, y) can be obtained from $\sigma(x, y)$ using the following integral [9]

$$\phi_h(x, y) = \frac{1}{2\pi}\int_C \sigma(x', y')\ell n\left(\frac{K}{\sqrt{(x-x')^2+(y-y')^2}}\right)dl' \tag{9}$$

where l' is the arc length on the contour C.

The boundary condition of the homogeneous potential ϕ_h is obtained from (2) and (5) as

$$\alpha\phi_h + \beta\frac{\partial\phi_h}{\partial n} = \gamma - \left(\alpha\phi_p + \beta\frac{\partial\phi_p}{\partial n}\right). \tag{10}$$

It can be seen that (6) along with the boundary condition of (10), constitute a similar boundary-value problem. A similar problem was addressed in [9] almost thirty years ago.

This completes the formulation of the problem. The characteristic features of this formulation are:

a. The frequency term appears in an explicit form.
b. The Green's function and the unknowns are independent of frequency. The Green's function is in fact the static Green's function.

Next we illustrate how to solve these coupled equations both for the homogeneous part and the particular integral.

III. NUMERICAL SOLUTION USING THE METHOD OF MOMENTS (MOM)

In order to solve the above equations given by (8)-(10) we employ the Method of Moments.

To evaluate the above integral in (8) we divide the domain $\Re$ into N sub-regions. The midpoint coordinates of each of the sub-regions $\Delta\Re_i$ are denoted by (x_{2i}, y_{2i}). Then the potential ϕ_p at the field point (x, y) is approximated by

$$\phi_p(x,y) \cong \sum_{i=1}^{N} \Theta(x_{2i}, y_{2i}) a_i(x,y) \tag{11}$$

where

$$a_i(x,y) = \frac{1}{2\pi} \iint_{\Delta\Re_i} \ell n \left(\frac{K}{\sqrt{(x-x')^2 + (y-y')^2}} \right) dx'dy' \tag{12}$$

Hence it is assumed that $\Theta(x, y)$ is constant within each sub-region $\Delta\Re_i$ and is equal to the value $\Theta(x_{2i}, y_{2i})$.

Next we show how to numerically evaluate (9). Here, we take recourse to MOM. We expand the surface unknown σ using a pulse expansion. For purposes of illustration and simplicity let us choose point matching. Through the use of a pulse-expansion and point-matching techniques we will solve the present problem given by (9). Furthermore, if the contour C is segmented by M straight lines of length ΔC_i between points i and $i + 1$, then σ can be represented by the step approximation

$$\sigma = \sum_{i=1}^{M} \sigma_i P_i(l) \tag{13}$$

where $P_i(l)$ is a pulse function equal to 1 on ΔC_i and zero elsewhere and σ_i is its unknown amplitude. Substituting (13) into (9), we obtain an approximation for ϕ_h

$$\phi_h(x,y) \cong \sum_{i=1}^{M} \sigma_i c_i(x,y) \tag{14}$$

where

$$c_i(x,y) = \int_{\Delta C_i} \ell n \left(\frac{K}{\sqrt{(x-x')^2 + (y-y')^2}} \right) dl' \tag{15}$$

Using (4), (11) and (14), the Helmholtz potential Ψ at an arbitrary field point (x, y) can now be expressed as

$$\Psi(x,y) = \sum_{i=1}^{M} \sigma_i c_i(x,y) + \sum_{i=1}^{N} (\lambda_i \Psi_i - F_i) a_i(x, y) \tag{16}$$

where for simplicity we have used the following abbreviations in (4):

$$\lambda_i = \lambda(x_{2i}, y_{2i})$$
$$F_i = F(x_{2i}, y_{2i})$$
$$\Psi_i = \Psi(x_{2i}\, y_{2i})$$

The unknown function $\Psi(x, y)$ in (16) of Helmholtz equation can now be evaluated once the unknown terms, σ_i and Ψ_i, are determined. Next a system of two matrix equations is derived and solved for the unknowns σ_i and Ψ_i. The first matrix equation of this system is readily obtained by satisfying (16) at the midpoints (x_{2j}, y_{2j}) of each of the N sub-region $\Delta\Re_i$. Using matrix notation, we obtain

$$[\Psi_i] = [p_{ji}][\sigma_i] + [q_{ji}][\lambda_i \Psi_i - F_i] \tag{17}$$

where $p_{ji} = c_i(x_{2j}, y_{2j})$, and $q_{ji} = a_i(x_{2j}, y_{2j})$.

The second matrix equation is now obtained by enforcing the boundary condition of (10) as follows. We define $\hat{r}_j = (x_j, y_j)$, $j = 1, 2, \ldots, M$, to be the midpoints of ΔC_j. The boundary conditions are enforced at each $\hat{r}_j$. Substitution of (11) and (14) into (10) gives the following set of equations

$$\sum_{i=1}^{M} \sigma_i w_{ji} = \lambda_i - \sum_{i=1}^{N} (\lambda_i \Psi_i - F_i) b_{ji} \qquad j = 1, 2, \ldots, M \tag{18}$$

where $\gamma_j = \gamma(\hat{r}_j)$ and

$$w_{ji} = \left(\alpha c_i + \beta \frac{\partial c_i}{\partial n} \right)_{(x,y)=\hat{r}_j} \tag{19}$$

$$b_{ji} = \left(\alpha a_i + \beta \frac{\partial a_i}{\partial n} \right)_{(x,y)=\hat{r}_j} \tag{20}$$

Equation (18) can now be written in matrix notations as

$$[w_{ji}][\sigma_i] = [\gamma_j] - [b_{ji}][\lambda_i \Psi_i - F_i] \tag{21}$$

Observe that (17) and (21) form a system of two equations in two unknowns σ_i and Ψ_i, from which they can be solved. We use (21) to obtain an expression for σ and then substitute it into (17), and after simple matrix manipulations we obtain the following equation for Ψ_i

$$[A][\Psi_i] = [B] \tag{22}$$

where

$$[A] = [I] + \left([p_{ji}][w_{ji}]^{-1}[b_{ji}] - [q_{ji}] \right)[\lambda_i] \tag{23}$$

$$[B] = \left([p_{ji}][w_{ji}]^{-1}[\gamma_j] + [p_{ji}] - [w_{ji}]^{-1}[b_{ji}] - [q_{ji}] \right)[F_i] \tag{24}$$

and $[I]$ denotes the $N \times N$ identity matrix.

From the last three equations some general comments can be made:

1) Analytic expressions can easily be derived for the evaluation of all the terms of the matrices $[A]$ and $[B]$ that include the integrals (12) and (15). This is true at least for the 2-D case.
2) The matrix elements $[w_{ji}]$, which are a part of the system matrix of the moment method, are similar to the matrix elements obtained in [9]. For different Helmholtz problems with different boundary conditions, $[w_{ji}]$ remains unchanged. This observation is important in an iteration scheme where the boundary conditions are kept the same.
3) Problems with multiple right-hand sides are solvable with minimum additional computation time since the function F in (17) appears only as a term of matrix $[B]$ in (24).
4) The domain and the contour discretization schemes are totally independent. This feature can offer the flexibility to handle boundary discontinuities without the need for excessive domain grid generations. This will be illustrated through numerical examples in the next section.
5) Once Ψ_i is determined at the grid points, using Gaussian elimination for instance the potential at any other point is obtained using ordinary matrix multiplications as shown by (17). No interpolations are needed.

Next, we illustrate these points through some numerical examples.

III. STATIC APPLICATIONS

Example 1—*Water Wave Propagation:* As a first example, we consider the problem of water wave propagation in a rectangular basin 100m × 100m [3]. Denoting by Ψ the water evaluation, then the wave propagation is governed by (1) with $F = 0$, and $\lambda = k^2$ where k is the wave number. The boundary conditions used are displayed in Figure 1. The solution by MOM is compared to the solutions obtained by finite difference method (FDM) and finite element method (FEM) for various mesh sizes inside the domain. The minimum number of nodes required for each method to converge to the exact solution at any arbitrary point is optimized. Figure 2 compares the solutions computed along the line $x = 90$ by the Method of Moments utilizing (1×1), (2×2) and (4×4) grids. Figure 3 shows the solutions obtained by the finite element method utilizing (5×5), (10×10), and (20×20) grids. Figure 4 shows the results obtained by the finite difference method utilizing (5×5), (15×15), and (35×35) grids. In all these figures, the solid line represents the exact solution. Referring to these figures, one can easily observe that a considerably smaller number of nodes is employed with the present method than with the conventional methods. The minimum number of the domain nodes required to obtain a satisfactory accuracy using MOM for the present method is 16 (4×4), compared to 400 (20×20) for FEM or up to 1000 nodes for FDM.

Example 2—MOST Modeling: The nonlinear Poisson's equation plays a key role in numerical modeling of semi-conductor devices. Many important characteristics of VLSI devices can be extracted from the solution of Poisson's equation. The most common approach to the numerical solution of the nonlinear Poisson's equation is based on the application of Newton's method to simultaneous discretized equations [15]. This approach often requires large storage especially for fine meshes, as is the case for two-dimensional modeling of the MOST [14].

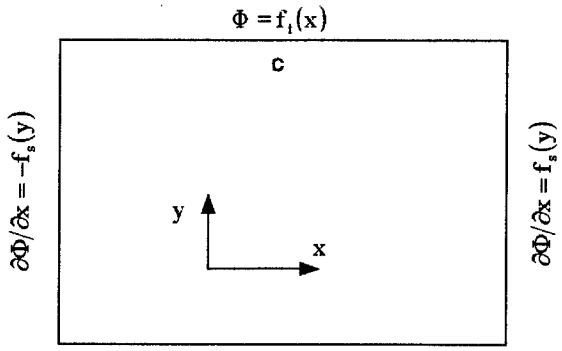

$$\text{where } f_1(x) = \begin{cases} \cos(\alpha x) & \text{if } 20 \le x \le 80 \\ -2 & \text{if } x < 80 \\ 1 & \text{if } x > 80 \end{cases}$$

$f_s(x) = \sin(\alpha y)$, $f_b(x) = \cos(\alpha x)$, and $\alpha = 2\pi$

Figure 1. Physical structure and the associated boundary conditions associated with Example 1.

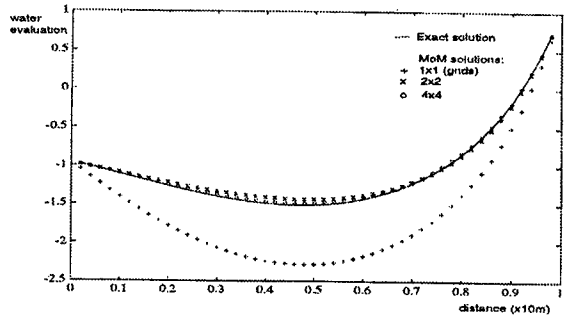

Figure 2. Solution obtained by the present method.

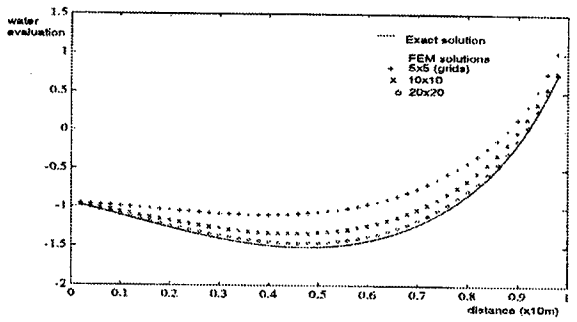

Figure 3. The FEM solution for Example 1.

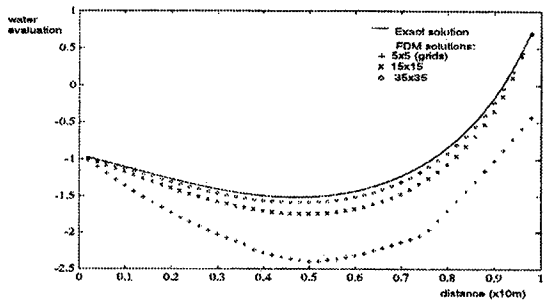

Figure 4. The FDM solution for Example 1.

In this section the MOM is applied to solve the nonlinear Poisson's equation that arises in the MOST modeling. We consider the MOST structure of Figure 5 made on a *p*-type substrate with doping N_A. Under the low current approximation the potential Φ is governed by the Poisson's equation [16]

$$\frac{\partial^2 \Psi}{\partial x^2} + \frac{\partial^2 \Psi}{\partial y^2} = \frac{n_i}{L_D^2}\left(e^{-\Psi} - e^{\Psi} - \frac{N_A}{n_i}\right) \tag{25}$$

where $\Psi = \Phi / V_T$ is the normalized potential, V_T is the thermal potential, n_i is the intrinsic carrier concentration, and L_D is the Debye length.

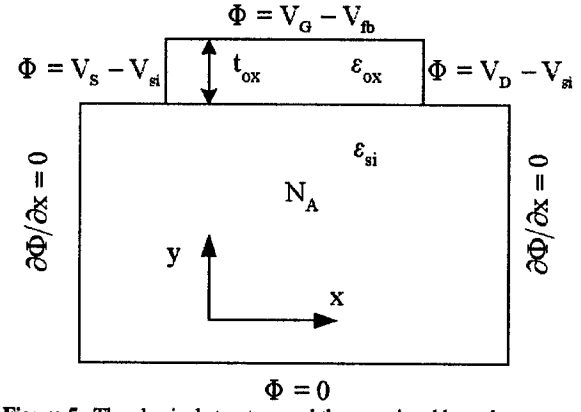

Figure 5. The physical structure and the associated boundary condition for MOST modeling.

The boundary conditions adopted along the edges of the device are the same as those used by [16], [12], and are displayed in Figure 5. On the oxide-semiconductor interface the following boundary condition is assumed

$$\varepsilon_{ox} \frac{V_G - \Phi - V_{FB}}{t_{ox}} = \varepsilon_s \frac{\partial \Phi}{\partial y} \tag{26}$$

where ε_{ox}, and ε_s are, respectively, the oxide and silicon permittivities, V_{FB} is the flat band voltage, and t_{ox} is the oxide thickness.

To solve the above elliptic problem we proceed first by dividing the boundary into M segments. Finer segments are used on the top edge of the device to handle its boundary discontinuities. Using the boundary conditions, and the technique described in [9], matrix $[w_{ji}]$ is computed, then inverted and stored. Independently, the base region is also divided into N finite elements or cells. We seek to determine the electric potential at each midpoint of the cells using (25) which is nonlinear. To solve it we set up an iterative procedure, based on Newton's linearization [15]. At the k-th iteration we replace the right-hand side of (25) by its Fourier expansion about Ψ^k. Then the following Helmholtz's equation is obtained

$$\frac{\partial^2\Psi^{(k+1)}}{\partial x^2}+\frac{\partial^2\Psi^{(k+1)}}{\partial y^2}-G\left(\Psi^{(k)}\right)\Psi^{(k+1)}=F\left(\Psi^{(k)}\right) \tag{27}$$

where F and G are given by

$$F\left(\Psi^{(k)}\right)=\frac{n_i}{L_D^2}\left(\left(\Psi^{(k)}+1\right)e^{-\Psi^{(k)}}+\left(\Psi^{(k)}-1\right)e^{\Psi^{(k)}}-\frac{N_A}{n_i}\right) \tag{28}$$

$$G\left(\Psi^{(k)}\right)=\frac{n_i}{L_D^2}\left(e^{-\Psi^{(k)}}+e^{\Psi^{(k)}}\right) \tag{29}$$

The iteration scheme starts by taking some initial guess value for $\Psi^{(0)}$ so that (27) can be solved for the first approximation $\Psi^{(1)}$. Then $\Psi^{(1)}$ is used to find the second approximation $\Psi^{(2)}$. The procedure is repeated until the norm $\left\| \Psi^{(k+1)} - \Psi^{(k)} \right\|$ is less than a desired tolerance. However, this iteration scheme often diverges [13], [15], and some damping factor was found necessary to improve the convergence of the iterative solution. At the beginning of the k-th iteration step, the following formula was used for all inner nodes

$$\Psi^{(k+1)}=(1-R)\Psi^{(k-1)}+R\Psi^{(k)} \tag{30}$$

where R (< 1) is the relaxation factor.

The accuracy of the solution obtained by the present technique is demonstrated by comparing it with the FDM (5-point) solution. For both methods, MOM and FDM, we let the values of the electric potential to be updated at each mesh point by means of an explicit formula, that is, without the solution of simultaneous algebraic equations [15]. We assign Ψ = 0, as an initial guess for all the inner nodes. Once the convergence is attained for the domain nodes, then the electric potential at any other point in the device is determined by a matrix multiplication as shown in (17), and without the need of any interpolation. For numerical computations, the following data were used: The thickness of the oxide layer was t_{ox} = 0.5 μm, the flat band voltage is $V_{FB} = -1$ V and the doping profile is assumed to be uniform with $N_A = 10^{18}$ cm^{-3}, $n_i = 1.5\times10^{10}$ cm^{-3}, thermal potential, V_T = 0.0258 V, and R = 0.1. The results of the computations are shown in Figure 6, where the distribution of the electric potential at the thermal equilibrium is plotted along different lines parallel to the x-axis. The solid lines represent the solution obtained using the FDM and (o) symbol is reserved for the solutions obtained by the present method. Close agreements can be observed between the two methods. However, for FDM 721 nonuniform mesh points are employed to reduce the total number of nodes {for uniform meshes over 4900 (70×70) nodes ought to be used}. Finer meshes were chosen in the depletion region and near the junctions to reproduce accurately the fast variation of the electric potential [16] and the surface discontinuities of the potential; whereas for MOM, the number of the uniform meshes was 529 (23×23) or 400 for nonuniform cells. The number of iterations required for the convergence was 51 with the present technique as compared to 108 iterations with FDM to reach the point at which the absolute maximum between two subsequent iterations was less than 0.05 (tolerance).

Next we apply this method to the solution of the cutoff-frequencies of various waveguides.

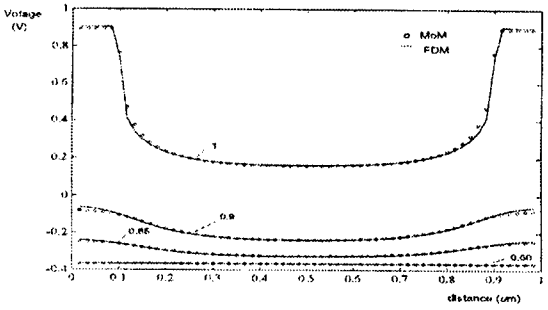

Figure 6: The distribution of the electric potentials along the lines parallel to the x-axis.

IV. SOLUTION OF THE GENERAL HELMHOLTZ EQUATION FOR HOMOGENEOUSLY FILLED WAVEGUIDES

In waveguides, solution of the Helmholtz equation determines the electromagnetic field configuration within the guides. It is convenient to divide the possible field configurations within the waveguides into two sets, namely TM waves and TE waves, each of which is governed by similar Helmholtz equations.

If we consider a waveguide in which the direction of propagation of the wave is along the z-direction, then the Helmholtz equations are as follows.

TM_z *Case* ($H_z \equiv 0$):

$$\nabla^2 E_z(x,y) + (\omega^2 \mu\varepsilon - K_z^2) E_z(x,y) = 0 \quad (31)$$

with the appropriate boundary conditions $E_z = 0$, on the conductor walls and for the

TE_z *Case* ($E_z \equiv 0$):

$$\nabla^2 H_z(x,y) + (\omega^2 \mu\varepsilon - K_z^2) H_z(x,y) = 0 \quad (32)$$

with appropriate boundary conditions $\partial H_z/\partial n = 0$,on the conductor walls where $\partial H_z/\partial n$ represents the normal derivative. Here,

- E_z z-component of the electric field;
- H_z z-component of the magnetic field;
- ω angular frequency = $2\pi f$;
- f frequency of interest;
- μ permeability of the homogeneous medium;
- ε permittivity of the homogeneous medium;
- K_z propagation constant in the z-direction.

Comparing (31) and (32) with (1), and also the boundary conditions of the TM_z and TE_z cases with those of the general equations, we can draw the following analogies as outlined in Table I.

By examining (32) that

$$[B] = [p_{ji}][w_{ji}]^{-1}[\gamma_j] + \left([p_{ji}][w_{ji}]^{-1}[b_{ji}] - [q_{ji}]\right)[F_i]$$

it can be inferred that $[B] = 0$, since $F = 0$ and $\gamma = 0$ for TM_z and TE_z cases.

In the case of TM_z, (22) reduces to the form

$$[A] \cdot [E_{zi}] = 0 \quad (33)$$

In the case of TE_z, (22) reduces to the form

$$[A] \cdot [H_{zi}] = 0 \quad (34)$$

Here again, E_{zi} and H_{zi} refer to the values of E_z and H_z at the midpoints of the subregions of the discretized waveguide cross section.

For (33) and (34), nontrivial solutions exist for $[E_{zi}]$ and $[H_{zi}]$ only if the matrix $[A]$ is singular. The condition for nontrivial (i.e., nonzero) solutions to exist for $[E_{zi}]$ and $[H_{zi}]$ it is essential that

$$\det[A] = 0 \quad (35)$$

where det[A] stands for *determinant of* [A]. We know from (23) that

$$[A] = \left([p_{ji}][w_{ji}]^{-1}[b_{ji}] - [q_{ji}]\right)[\lambda_i] + [I]$$

and we also know that for the cases of the TM_z and TE_z waves

$$\lambda = \omega^2 \mu\varepsilon - K_z^2. \quad (36)$$

Table I
Special cases of the General Helmholtz Equation

General Equation (3)	TM_z Equation (1)	TE_z Equation (2)
$\nabla^2\Psi + \lambda\Psi = F$	$\nabla^2 E_z + (\omega^2\mu\varepsilon - K_z^2)\cdot E_z = 0$	$\nabla^2 H_z + (\omega^2\mu\varepsilon - K_z^2)\cdot H_z = 0$
Ψ	E_z	H_z
λ	$\omega^2\mu\varepsilon - K_z^2$	$\omega^2\mu\varepsilon - K_z^2$
F	0	0
$\alpha\Psi + \beta\cdot\partial\Psi/\partial n = \gamma$	$E_z = 0$	$\partial H_z/\partial n = 0$
γ	0	0

Hence, given the frequency at which the Helmholtz equation is to be solved, det [A] would be a function of K_z, the roots of which will provide the values of K_z for which det [A] = 0. Once these K_z values are known, the eigenvector of [A] corresponding to the minimum eigenvalue gives the nontrivial solutions for [E_{zi}] and [H_{zi}] in case of TM_z and TE_z cases, respectively.

Once [E_{zi}] and [H_{zi}] are determined at the grid points, using Gaussian elimination for instance, the values of E_z and H_z at any other point can be obtained using ordinary matrix multiplications, as explained in [1].

IVa. Calculation of Propagation Constants for Different Waveguide Modes

It is evident that for the existence of nontrivial (nonzero) solutions for [E_{zi}] and [H_{zi}], it is necessary that (35) be satisfied. Let us define a matrix [Z] such that

$$[Z]=\left([p_{ji}][w_{ji}]^{-1}[b_{ji}]-[q_{ji}]\right). \tag{37}$$

Hence, (35) becomes

$$\det([Z][\lambda_i]+[I])=0 \tag{38}$$

which can be rewritten as

$$\det\left([Z]-\left(\frac{-1}{\lambda_i}\right)[I]\right)=0. \tag{39}$$

Equation (39) is similar to the characteristic equation of matrix [Z], with its eigenvalues given by $-1/\lambda_i$. Knowing that λ_i above $\equiv\omega^2\mu\,\varepsilon - K_z^2$ for TM_z and TE_z cases, it can be concluded that

$$\frac{-1}{\lambda_i}=\frac{1}{(K_z^i)^2-\omega^2\mu\varepsilon}=EV_i^{[Z]}, \quad i=1,2,...,N. \tag{40}$$

where K_z^i is the propagation constant of the ith mode and $EV_i^{[Z]} \equiv$ ith eigenvalue of [Z].

Equation (40) can be rearranged as

$$(K_z^i)^2=\omega^2\mu\varepsilon+\frac{1}{EV_i^{[Z]}}. \tag{41}$$

Therefore, the propagation constants of different modes in the waveguide are given by the following:

For $(K_z^i)^2>0$,

$$K_z^i=\sqrt{\omega^2\mu\,\varepsilon+\frac{1}{EV_i^{[Z]}}} \quad \text{propagating modes} \tag{42}$$

For $(K_z^i)^2<0$,

$$K_z^i=j\sqrt{\omega^2\mu\,\varepsilon+\frac{1}{EV_i^{[Z]}}} \quad \text{nonpropagating modes} \tag{43}$$

Results of propagation constants of various modes in a rectangular waveguide computed by this method are shown next.

IV b. Calculation of Cutoff Frequencies for Different Waveguide Modes

The cutoff frequencies for the various propagating modes in the waveguide are given by

$$f_c^i=\frac{\upsilon}{2\pi}\sqrt{(\omega^2\mu\,\varepsilon-(K_z^i)^2)} \tag{44}$$

where $f_c^i \equiv$ cutoff frequency of the ith mode. Here, $\upsilon \equiv$ velocity of light in the homogeneous medium $\equiv 1/\sqrt{\mu\,\varepsilon}$ and it can be deduced from (41) that

$$\omega^2\mu\varepsilon-\left(K_z^i\right)^2=\frac{-1}{EV_i^{[Z]}}, \quad i=1,2,...,N \tag{45}$$

Using (45) in (44), we find the cutoff frequencies for the first N propagating modes as

$$f^i=\frac{\upsilon}{2\pi}\sqrt{\frac{-1}{EV_i^{[Z]}}}, \quad i=1,2,...,N. \tag{46}$$

The cutoff wave number k_c^i of the ith mode can be calculated from the cutoff frequency using the relation

$$k_c^i=\frac{2\pi f_c^i}{\upsilon}, \quad i=1,2,...,N$$

This method thereby provides a straightforward approach to find the cutoff frequencies (and, hence, cutoff wavenumbers) of any waveguide structure

without resorting to scanning over a wide range of frequencies, as is done in the Ritz-Galerkin and surface integral-equation methods.

V a. Results: Rectangular Waveguide

Consider a rectangular waveguide. For the waveguide in Figure 7, the region was divided into 100 subregions and the boundary was discretized into 96 subcontours. The maximum matrix size involved in the computations was 100×100. Results have been displayed in Table II for the cutoff wave numbers of the first eight TM_z/TE_z modes. The computational time involved in finding the cutoff wavenumbers of the first 100 modes on a Sun SPARC 10 workstation was 16 s.

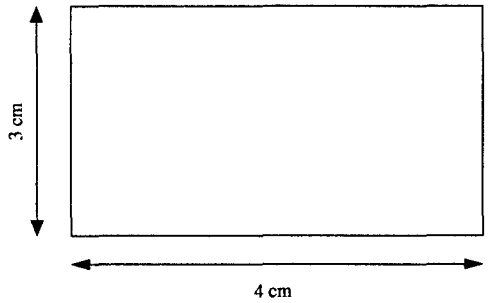

Figure 7. A rectangular waveguide.

Table II
Cutoff wavenumbers for air-filled rectangular waveguide

Mode No.	Mode	k_e actual (rad/cm)	k_c computed (rad/cm)	Diff. %
1-0	TE_z	0.7857	0.7921	0.81
0-1	TE_z	1.0476	1.0536	0.57
1-1	TE_z, TM_z	1.3095	1.3239	1.00
2-0	TE_z	1.5714	1.5827	0.72
2-1	TE_z, TM_z	1.8886	1.9108	1.10
0-2	TE_z	2.0952	2.1095	0.68
1-2	TM_z, TM_z	2.2377	2.2610	1.00
3-0	TE_z	2.3571	2.3896	1.30

Vb. Single-Ridge Waveguide

A single ridge waveguide is a popular means of getting higher bandwidth. The first four TMz and TEz mode cutoff wavenumbers were computed for the single-ridge hollow waveguide shown in Figure 8. Results have been displayed in Table III and compared with published data. For the waveguide, the region was divided into 96 subregions and the boundary was discretized into 112 subcountours. The maximum matrix size involved in computations was 96×96. The computational time involved in finding the cutoff wavenumbers of the first 96 modes in each case on a Sun SPARC 10 workstations was 18 s.

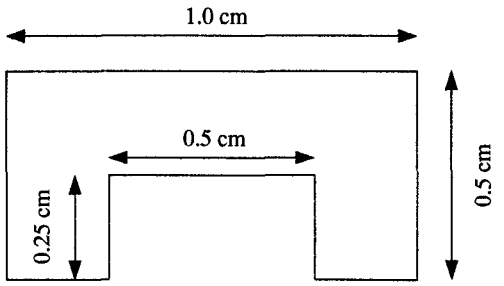

Figure 8. A single-ridge waveguide.

Table III
Cutoff wavenumbers for air-filled single-ridge waveguide

Mode No.	Mode	k_c published (rad/cm)	k_c computed (rad/cm)	Diff. %
1.	TM_z	12.1640[5]	12.2338	0.57
2.	TM_z	12.2938[17]	12.4106	0.95
3.	TM_z	13.9964[17]	14.2152	1.56
4.	TM_z	15.5871[17]	15.8221	1.50
5.	TE_z	2.2566[5]	2.2688	0.54
6.	TE_z	4.9436[17]	5.0149	1.44
7.	TE_z	6.5189[17]	6.6289	1.68
8.	TE_z	7.5642[17]	7.7097	1.92

VI. CONCLUSION

An efficient technique based on MoM formulation for solving a general Helmholtz equation starting from Laplace's equation is presented. The main feature of this new formulation is that the boundary conditions are satisfied independent of the discretizations of the regions and the nodes. This feature was found especially useful when the boundary conditions have discontinuities. Considerable reduction in the domain grids is realized with the present method as compared to the conventional methods such as finite difference method or the finite element methods. In addition, one need not use a frequency dependent Green's function which can reduce the computational cost significantly.

VII. REFERENCES

[1] L. G. Copley, "Fundamental results concerning integral representation in acoustic radiation," *J. Acoust. Soc. Am.*, Vol. 44, pp. 28–32, 1963.

[2] R. A. Altenkirch, M Rezayat, R. Eichhorn, and F. J. Rizzo, "A study of heat conduction forward of flame in solids, by the boundary integral equation method," *Trans. ASME Ser. C. J. Heat Transfer*, Vol. 104, pp. 734–740, 1982.

[3] M. Kawahara and K. Kashiyama, "Boundary type finite element method for surface wave motion based on the trigonometric function interpolation," *Int. J. Numer. Meth. Eng.*, Vol. 21, pp. 1833–1852, 1985.

[4] J. R. Rice and R. F. Boisvert, *Solving Elliptic Problems Using ELLPACK*. New York: Springer-Verlag, 1985.

[5] P. L. Arlett, A. K. Bahrani, and O. C. Zienkiewicz, "Application of finite elements to the solution of Helmholtz's equation," *Proc. IEE*, Vol. 115, No. 12, pp. 1762–1766, 1968.

[6] M. Rezayat, F. J. Rizzo, and D. J. Shippy, "A unified boundary integral equation method for class of second order elliptic boundary value problems," *J. Austral. Math. Soc. Ser.*, Vol. B–25, pp. 501–517, 1984.

[7] K. Nagaya, and T. Yamaguchi, "Method for solving eigenvalue problems of the Helmholtz equation with an arbitrary shaped outer boundary and a number of eccentric inner boundaries of arbitrary shape," *J. Acoust. Soc. Am.*, Vol. 90, pp. 2146–2153, 1991.

[8] P. J. Harris, A boundary element method for Helmholtz equation using finite part integration," *Comp. Meth. Appl. Mech. Eng.*, Vol. 95, pp. 331–342, 1992.

[9] R. F. Harrington, K. Pontoppidan, P. Abrahamsen, and N. C. Abertsen, "Computation of Laplacian potentials by an equivalent source method," *Proc. IEE*, Vol. 116, No. 10, pp. 1715–1920, 1969.

[10] C. A. Brebbia, *The Boundary Element Method for Engineers*. New York: Wiley, 1978.

[11] R. F. Harrington, *Field Computation by Moment Methods*. New York: Macmillian, 1968.

[12] E. Arvas, R. I. Turkman, and P. S. Neelakantaswamy, "MOSFET analysis through numerical solution of Poisson's equation by the method of moments," *Solid-State Elect.*, Vol. 30, No. 12, pp. 1355–1361, 1987.

[13] G. De Mey, "The boundary element method for modeling semiconductor components under low current approximation," in *Proc. Int. Conf. Simulation of Semiconductor Devices and Processes*, Pineridge Press, 1984, pp. 261–266.

[14] W. Fichtner, D. J. Rose, and R. E. Bank, "Semiconductor device simulation," *IEEE Tran. Electron. Devices*, Vol. ED-30, No. 9, pp. 1018–1030, 1983.

[15] W. F. Ames, *Nonlinear Partial Differential Equations in Engineering*. New York: Academic, 1965.

[16] J. D. Kendall and A. R. Boothroyd, "A two-dimensional analytical threshold voltage model for MOSFET's with arbitrarily doped substrates," *IEEE Electron Device Lett.*, Vol. EDL–7, pp. 401–403, 1986.

Tapan Kumar Sarkar (http://web.syr.edu/~tksarkar) received the B. Tech. degree from the Indian Institute of Technology, Kharagpur, India, in 1969, the M.Sc.E. degree from the University of New Brunswick, Fredericton, Canada, in 1971, and the M.S. and Ph.D. degrees from Syracuse University; Syracuse, New York in 1975.

From 1975 to 1976 he was with the TACO Division of the General Instruments Corporation. He was with the Rochester Institute of Technology, Rochester, NY, from 1976 to 1985. He was a Research Fellow at the Gordon McKay Laboratory, Harvard University, Cambridge, MA, from 1977 to 1978. He is now a Professor in the Department of Electrical and Computer Engineering, Syracuse University; Syracuse, NY. His current research interests deal with numerical solutions of operator equations arising in electromagnetics and signal processing with application to system design. He obtained one of the "best solution" awards in May 1977 at the Rome Air Development Center (RADC) Spectral Estimation Workshop. He has authored or coauthored ten books including the latest ones "Iterative and Self Adaptive Finite-Elements in Electromagnetic Modeling" and "Wavelt Applications in Engineering Electromagnetics" which were published in 1998 and 2002, respectively by Artech House, more than 210 journal articles and numerous conference papers and has written chapters in 28 books. The book on "Smart Antennas" will be published by John Wiley in March 2003.

Dr. Sarkar is a registered professional engineer in the State of New York. He received the Best Paper Award of the IEEE Transactions on Electromagnetic Compatibility in 1979 and in the 1997 National Radar Conference. He received the College of Engineering Research Award in 1996 and the chancellor's citation for excellence in research in 1998 at Syracuse University. He was elected Fellow of the IEEE in 1991. He was an Associate Editor for feature articles of the IEEE Antennas and Propagation Society Newsletter, and he was the Technical Program Chairman for the 1988 IEEE Antennas and Propagation Society International Symposium and URSI Radio Science Meeting.

Currently he is a distinguished lecturer for the IEEE Antennas and Propagation society. He is on the editorial board of Journal of Electromagnetic Waves and Applications and Microwave and Optical Technology Letters. He has been appointed U.S. Research Council Representative to many URSI General Assemblies. He was the Chairman of the Intercommission Working Group of International URSI on Time Domain Metrology (1990-1996). Dr. Sarkar is a member of Sigma Xi and International Union of Radio Science Commissions A and B. He received the title Docteur Honoris Causa from Universite Blaise Pascal, Clermont Ferrand, France in 1998 and the *Friends of Clermont Ferrand* award in 2000.

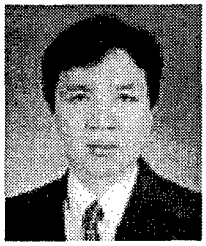

Young-Seek Chung received the B.S., M.S. and Ph.D. degrees in Electrical Engineering from Seoul National University, Seoul, Korea, in 1989, 1991, and 2000, respectively.
From 1991 to 1996, he was with the Living System Laboratory, LG Electronics. From 1998 to 2000, he was a Teaching Assistant in Electrical Engineering at the Seoul National University. Since 2001, he has been working at the Syracuse University with Dr. Tapan K. Sarkar. His current interests are the numerical analysis and the inverse scattering using the time domain techniques.

Magdalena Salazar-Palma was born in Granada, Spain. She received the degree of *Ingeniero de Telecomunicación* and the Ph.D. degree from the *Universidad Politécnica de Madrid* (Madrid, Spain), where she is a *Profesor Titular de Universidad* of the *Departamento de Señales, Sistemas y Radiocomunicaciones* (Signals, Systems and Radiocommunications Department) at the *Escuela Técnica Superior de Ingenieros de Telecomunicación* of the same university. She has taught courses on electromagnetic field theory, microwave and antenna theory, circuit networks and filter theory, analog and digital communication systems theory, numerical methods for electromagnetic field problems, as well as related laboratories.

She has developed her research within the *Grupo de Microondas y Radar* (Microwave and Radar Group) in the areas of electromagnetic field theory, computational and numerical methods for microwave structures, passive components, and antenna analysis; design, simulation, optimization, implementation, and measurements of hybrid and monolithic microwave integrated circuits; and network and filter theory and design. For a number of times she has been a visiting professor at the Department of Electrical Engineering and Computer Science, Syracuse University (Syracuse, New York, USA).

She has authored three scientific books and a total of 15 contributions for chapters and articles in books published by international editorial companies, 25 papers in international journals, and 125 papers in international conferences, symposiums, and workshops, plus a number of national publications and reports. She has delivered a number of invited presentations, lectures, and seminars. She has lectured in several short courses, some of them in the frame of European Community Programs. She has participated in 45 projects and contracts, financed by international, European, and national institutions and companies. She has been a member of the Technical Program Committee of several international symposiums and has acted as reviewer for different international scientific journals, symposiums, and editorial companies. She has assisted the *Comisión Interministerial de Ciencia y Tecnología* (National Board of Research) in the evaluation of projects. She has also served in several evaluation panels of the Commission of the European Communities. In the past she has acted several times as topical editor for the disk of references of the triennial Review of Radio Science. She is a member of the editorial board of three scientific journals. She is a registered engineer in Spain. She is a senior member of the Institute of Electrical and Electronics Engineers (IEEE). She has served as vicechairman and chairman of IEEE Spain Section MTT-S/AP-S (Microwave Theory and Techniques Society / Antennas and Propagation Society) Joint Chapter and chairman of IEEE Spain Section. She is a member of IEEE Region 8 Nominations and Appointments Committee, IEEE Ethics and Member Conduct Committee, and IEEE Women in Engineering Committee (WIEC). She is acting as liaison between IEEE Regional Activities Board and IEEE WIEC. She has received two individual research awards from national institutions.

Splitting of Material Cells and Averaging Properties to Improve Accuracy of the FDTD Method at Interfaces

R. S. Schechter, M. Kragalott, M .S. Kluskens, and W. P. Pala

Authors are in Code 5310 of the Radar Division at the Naval Research Laboratory, Washington DC 20375
(schechter@cem.nrl.navy.mil)

Abstract - In this paper we present a simple modification to the traditional Finite Difference Time Domain (FDTD) method for treating material cells. The Yee cell is split into 8 smaller material subcells so that each E and H field point is considered to be located at the crosspoint of 8 cells with differing material properties. Thus there is no longer an overlap of the material cells associated with the components of the E and H fields. The 8 material properties are averaged at each crosspoint. Since the averaging is done outside the time marching loop there is little increase in the total computational time. Numerical results are shown for a sinusoidal plane wave scattering from a dielectric sphere. These results are compared with the exact Mie solution and the traditional material cell method along different cuts through the sphere. The splitting and averaging is shown to give improved amplitude accuracy in the vicinity of the sphere. Improvement is also observed at planar interfaces angled with respect to the grid. An additional benefit of this subcell formulation is that objects may be modeled with twice the geometrical resolution without increasing the size of the staggered grid.

Index Terms- FDTD, Subcell, Split cell, Effective Dielectric Constant

I. INTRODUCTION

The finite-difference time domain (FDTD) technique is a widely used method for computing electromagnetic scattering. The formulation is based on the ideas put forth in [1] and involve computing the electric and magnetic (E and H) fields on a staggered grid. There are some shortcomings with the Yee method when applied to interfaces between materials. First, the material cells associated with the field components (staggered in space) are centered around each field point and thus overlap in space. Second, the discontinuity in permittivity at interfaces between different media causes accuracy problems. Third, is the error caused by approximating a curved boundary by a staircased one.

Various methods have been proposed to improve the accuracy of the basic FDTD method at interfaces, mainly by reducing the staircasing errors caused by angled or curved boundaries. For example, one method uses a volume weighted average of ε on each side of a material interface [2]. An effective dielectric constant is computed as follows:

$$\varepsilon_{eff} = (V_1\varepsilon_1 + V_2\varepsilon_2)/V_{cell}, \qquad (1)$$

where V_1 is the volume on one side of the interface and V_2 is the volume on the other side of the interface. This method requires a special treatment of each material interface. Specifically the method requires identifying which cells are intersected by the boundary and where the boundary intersects these cells. Dey and Mittra reported that the results using this approach are significantly more accurate than using a staircase to approximate the surface of a dielectric structure. Another approach uses effective dielectric constants together with the contour-path integral FDTD (CFDTD) method [3]. Recently a new technique was developed that utilizes the electric field components along the edges of the cell [4]. Rather than using the volume of the dielectric occupying a cell it instead uses the length of the dielectric intersecting the cell edges.

Still another method uses dielectric subgrid resolution (DSR) [5]. This can be described as partitioning a standard cell into 8 subcells, each homogeneously filled. The 8 cells can have different material properties. Generalized constitutive parameters are obtained by treating each cell as an equivalent lumped circuit. It is shown by numerical example that on coarser grids the simpler averaging method gives more accuracy than the lumped circuit approach across interfaces. The DSR method also requires greater memory since there are effective dielectric constants for 3 directions.

The practical advantage to the approach presented in this paper is that no special preprocessing operations are required to compute the intersections of cells with interface boundaries. The comparisons in this paper are on the basis of field amplitudes as opposed to resonance frequencies used in the cited articles.

II. SIMPLE SUBCELL MODEL

The method presented here uses the standard staggered grid scheme but now sub-divides or splits the existing cell into 8 smaller cells as shown in Fig. 1. Each field point may now be viewed as a crosspoint surrounded by 8 subcells with differing parameters as

opposed to being at the center of a material cell. The material cells no longer overlap in space for the staggered field points. A sphere, for example, cutting through the standard Yee cell still is approximated with a staircase but with twice the number of cells. Unlike some previous approaches there are no special calculations related to the specific geometry modeled.

Applying Ampere's Law around a contour C_1 one obtains:

$$\frac{\partial}{\partial t}\int_{S_1}\vec{D}\cdot d\hat{S}_1 = \oint_{C_1}\vec{H}\cdot d\hat{l}_1 . \qquad (2)$$

From Fig. 1, assuming that D_z is constant over a surface patch S_1 (center x-y plane in Fig. 1) and is equal to the value at the center of the patch, the surface integral becomes:

$$\int_{S_1} D_z dS = \varepsilon(i,j,k)E_z\Big|_{i,j,k}\Delta x\Delta y . \qquad (3)$$

Assume also that the value of the H field along each contour leg is constant and equal to the value at the midpoint of the leg. Since the material cell is now split, further assume that at the cell center (i,j,k) or crosspoint of the 8 material cells, that the effective dielectric constant is the average of the 8 surrounding material cells or :

$$\varepsilon(i,j,k) = \bar{\varepsilon}(i,j,k) = 1/8\sum_{n=1}^{8}\varepsilon_n . \qquad (4)$$

Using central-difference approximations for the time derivatives (interleaved in time) the following step-ahead equation results - valid for non-cubical cells.

$$E_z^{n+1}\Big|_{i,j,k} = E_z^n\Big|_{i,j,k} + \frac{\Delta t}{\bar{\varepsilon}(i,j,k)}\left[\frac{1}{\Delta y}H_x^{n+1/2}\Big|_{i,j-1/2,k} + \frac{1}{\Delta x}H_y^{n+1/2}\Big|_{i+1/2,j,k} - \frac{1}{\Delta y}H_x^{n+1/2}\Big|_{i,j+1/2,k} - \frac{1}{\Delta x}H_y^{n+1/2}\Big|_{i-1/2,j,k}\right] \qquad (5)$$

Analogous equations can be developed for E_y and E_x.

III. BENCHMARK PROBLEM - DIELECTRIC SPHERE

The problem considered is a plane wave scattering from a dielectric sphere. The incident wave has the electric field polarized in the z direction and travels in the +y direction as shown in Fig. 2. The dielectric sphere has a radius of 4.5 cm. In this work we consider scattering at two frequencies and two dielectric constants. Case I is at a frequency of 2.5 GHz with $\varepsilon = 4\varepsilon_0$ in the sphere and Case II is at 1.768 GHz with $\varepsilon = 8\varepsilon_0$ in the sphere. In each case the wavelength in the sphere is the same. The Mie series solution for the fields inside and outside the sphere is compared to numerical FDTD results.

A. Computational Modeling

Numerical results are generated using a 3D FDTD computational code that implements the standard Yee method with and without the subcell averaging. The computational grid is 512 x 256 x 512. At the extremities of the grid Liao second order absorbing boundary conditions (ABC'S) are employed. A sine wave source is fed in at y=5. The incident wave is planar over 1/2 of the grid's width or from x= 128 to x=384, with a Gaussian taper toward the absorbing boundaries This finite-width waveform approximates plane wave conditions in the vicinity of the sphere. The spatial discretization Δx is set to $\lambda/20$ (in the dielectric media) for both Cases I and II. The sphere has a radius of $15\,\Delta x$;however, with the split cell model, the sphere has a radius of 30 subcells. The FDTD simulation is run in continuous wave (cw) mode, long enough to achieve steady-state conditions over the extent of the grid. The amplitudes of the vector components of the E field are saved along chosen line cuts (along y) though the sphere. The program, which updates large 3D grids, is written with OpenMP directives to run efficiently on an SGI Origin parallel computer.

B. Analytical Solution

The Mie solution for a plane harmonic wave scattering from a dielectric sphere is well known and may be found in several references [6,7]. This exact solution is a series for the scattered field exterior to the sphere and the transmitted or total field interior to the sphere. The incident field is added to the scattered field to obtain the total field outside the sphere. The resulting vector components, in spherical polar coordinates, are transformed into Cartesian vector components along various cuts though the sphere. This permits a direct comparison with the FDTD solution. Care must be taken to insure that the FDTD cuts correspond exactly in space with the analytical ones.

C. Results and Comparison

Fig. 3 shows comparisons for Case I between the Mie solution (exact), the 8 subcell or split cell model, and standard cell model for the magnitude of E_z along a

straight line through the sphere. For cuts parallel to the y-axis, $E_z(0,y,0)$ in Fig. 3(a) and $E_z(8,y,0)$ in Fig. 3(b), the standard cell, the split cell and exact results are close and difficult to distinguish. However, the standard cell model exhibits a local amplitude overshoot at the back of the sphere. The subcell model produces more accurate field values at the back of the sphere.

Fig. 4 shows the comparison between the Mie solution, the subcell model, and the standard model for the magnitude of E_y. Along the cut $E_y(0,y,1)$ shown in Fig.4(a), the standard cell model gives a large undershoot and spatial phase error near the back of the sphere, where there is a discontinuity in E_y. The subcell model does not exhibit this large undershoot or spatial error. The standard cell model also overshoots the exact solution near the front of the sphere. Fig. 4(b) shows the cut $E_y(0,y,8)$. The standard cell and split cell are closer in amplitude away from the center (z=0) plane.

Figs. 5 and 6 show the analogous comparisons for Case II. A rather large overshoot is apparent in Fig. 5(b) near the back of the sphere in the z=8 plane for the standard cell case. Fig. 6(a) best illustrates the standard cell errors and shows large undershoots at both the front and back of the sphere, where there are jump discontinuities in E_y. An overshoot at the back of the sphere for the standard cell method is also apparent in Fig. 6(b). The split cell model agrees better with the exact at both the front and back of the sphere.

To compare the split cell and averaging method with the similar dielectric subgrid resolution (DSR) method [5]. Case II was computed using a grid spacing of 1/10 of a wavelength in the sphere. This coarse grid accentuates any differences between the methods. The E_y component across the interface best illustrates these differences. Fig. 7(a) shows that the DSR method tends to underestimate the jump discontinuities as compared to the simpler averaging method. However, at 1/20 of a wavelength in the sphere, the DSR and simple averaging curves are both converging to the Mie result, as shown in Fig.7(b).

IV. PLANAR INTERFACES

The performance of the split cell FDTD method is further demonstrated by computing the reflection and transmission of a plane wave Gaussian pulse polarized in the z direction from a planar interface. The grids are chosen to be 128×64×128. An interface tilted at 14° is simply a wedge angled from (0,64,z) to (128,128,z). The grid spacing is based on the 2/3 down power point for the pulse. At this frequency the grid spacing is chosen to be 1/10 of a wavelength in the dielectric. At smaller grid spacings the differences between the split cell and standard cell become minimal for a single pulse. For 1/10 of a wavelength grid spacing in the dielectric a second-order accurate FDTD formulation is used. The same cases are repeated with a coarser grid spacing of 1/7.5 of a wavelength but using a fourth-order (second-order in time and fourth-order in space or 2,4 scheme) FDTD formulation.

The peak amplitudes of the transmitted pulse and reflected pulse are compared with the exact amplitudes. In order to capture the reflected amplitude the incident pulse is subtracted out on the reflecting side of the interface. The results are summarized in Tables I-IV. The percent errors are shown in parentheses. The data show that the split cell formulation is consistently more accurate for interfaces angled at 14°. The cell splitting and averaging is particularly useful on coarse grids where staircasing errors may be more of a concern. The split cell and standard cell give the same transmitted and reflected amplitudes for 0° (normal incidence) thus illustrating that the averaging only has an effect for interfaces at angles.

V. CONCLUSIONS

The split cell and averaging method is shown to give improved accuracy across angled interfaces and along curved interfaces, such as a sphere. The method is especially useful where coarser grids are required. The technique is very simple, only requiring that the material cells have twice the resolution of the field cells. Since the averaging of the dielectric constants is done prior to the time stepping of the fields there is little added computational cost.

ACKNOWLEDGEMENTS

The authors wish to thank the Department of Defense High Performance Computing Program for providing the computing resources. This work was funded by the 6.1 basic research program at the Naval Research Laboratory.

REFERENCES

[1] K. S. Yee, "Numerical solution of initial boundary value problems involving Maxwell's equations in isotropic media," *IEEE Trans. Antennas and Propagation*, Vol. 14, pp. 302-307, May 1966.

[2] S. Dey and R. Mittra, "A conformal finite-difference time-domain technique for modeling cylindrical dielectric resonators," *IEEE Trans. Microwave Theory and Techniques*, Vol. 47, pp. 1737-1739, Sept. 1999.

[3] N. Kaneda, B. Houshmand, and T. Itoh, "FDTD Analysis of Dielectric Resonators with Curved Surfaces," *IEEE Trans. Microwave Theory and Techniques*, Vol. 45, pp.1645-1649, Sept. 1997.

[4] W. Yu and R. Mittra, "A Conformal Finite Difference Time Domain Technique for Modeling Curved Dielectric Surfaces," *IEEE Microwave and Wireless Components Letters*, Vol. 11, pp.25-27, Jan. 2001.

[5] G. Marrocco, M. Sabbadini, and F. Bardati, "FDTD Improvement by Dielectric Subgrid Resolution, "*IEEE Trans. Microwave Theory and Techniques*, Vol. 46, pp. 2166-2169, Dec. 1998.
[6] J. A. Stratton, *Electromagnetic Theory*, New York and London: McGraw-Hill, 1941.
[7] M. N. O. Sadiku, *Numerical Techniques in Electromagnetics*, Boca Raton, London, New York, Washington D.C.:CRC Press 2001.

Richard Schechter is a physicist in the Radar Division at Naval Research Laboratory in Washington DC. His current interests are the finite-difference time domain (FDTD) method, parallel computing, and computational electromagnetics. He also has conducted reasearch and published articles on simulating ultrasonic wave propagation on parallel computers. He obtained his B.S. in Physics from the University of Maryland in 1974 and took further graduate studies in physics and applied mathematics 1974-1980 at American University and Catholic University, both in Washington DC.

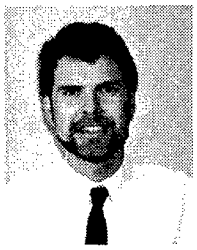

Mark Kragalott received the B.A. degree in physics and economics at Kenyon College in 1983, and M.S. and Ph.D. degrees in electrical engineering from The Ohio State University, in 1988 and 1993, respectively. As a Graduate Research Associate at the ElectroScience Laboratory at The Ohio State University, he conducted research on method of moments and extremely low frequency shielding. Since 1994 he has been with the Electromagnetics Section in the Analysis Branch of the Radar Division at the Naval Research Laboratory, Washington, D.C, where he has conducted research in topics ranging from computational electromagnetics to ultrawideband radiation and scattering.

Michael S. Kluskens received B.S. and M.S. degrees in electrical engineering from Michigan Technological University, Houghton, MI, in 1984 and 1985, respectively, and the Ph.D degree from The Ohio State University, Columbus, OH, in 1991. From 1986 to 1991, he was a Graduate Research Associate at the Electroscience Laboratory, Department of Electrical Engineering, the Ohio State University, where he conducted research on the method of moments and chiral media. He has been with the Radar Division of the Naval Research Laboratory, Washington D.C. since 1991 and is currently with the Electromagnetics Section of the Analysis Branch of the Radar Division. His primary research is in computational elecltromagnetics with emphasis on the method of moments, finite-difference time domain, and scattering from large complex structures.

William P. Pala received the B.S., M.S. and Ph.D degrees in physics from The American University, Washington, DC, in 1969, 1971, and 1976, respectively. He was a Graduate Research Associate from 1974 to 1977 at the Naval Research Laboratory. He joined the staff of the Naval Research Laboratory, Washington , DC, in 1978 where he is currently the Branch Chief of the Radar Analysis Branch. He has conducted systems research on orbital and naval radar designs. He has been conducting basic and applied research in radar cross-section determination for targets of naval interest for almost two decades. His current research interests are in computational electromagnetics, antennas, ocean scattering, automatic target recognition, and radar signature measurements. Dr. Pala is a member of the IEEE Antennas and Propagation Society and Sigma Phi Sigma physics honor society.

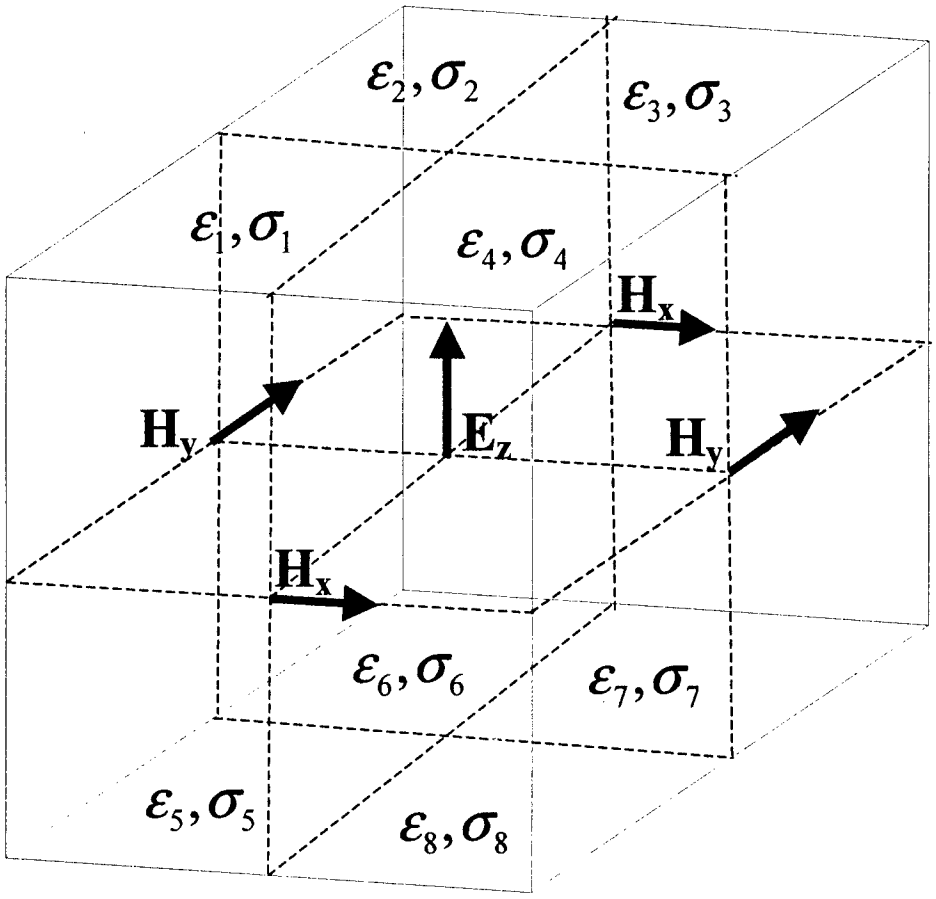

Fig. 1 Diagram of Yee cell with 8 subcells along with the position of the **E** and **H** vector components.

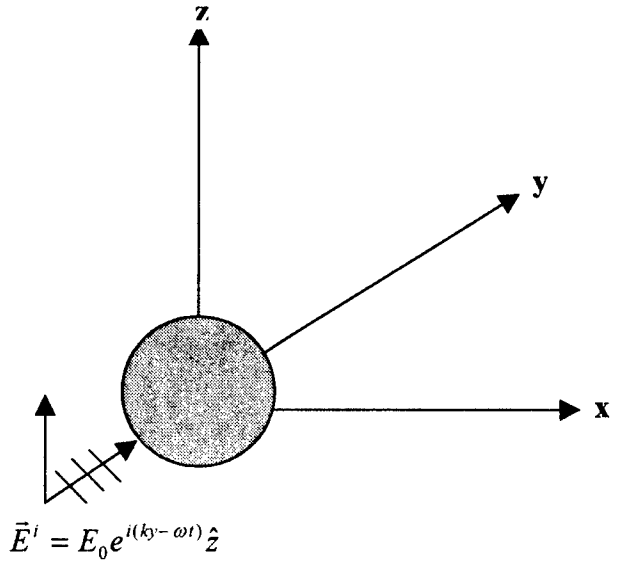

Fig. 2 Diagram of incident wave, dielectric sphere, and coordinate system.

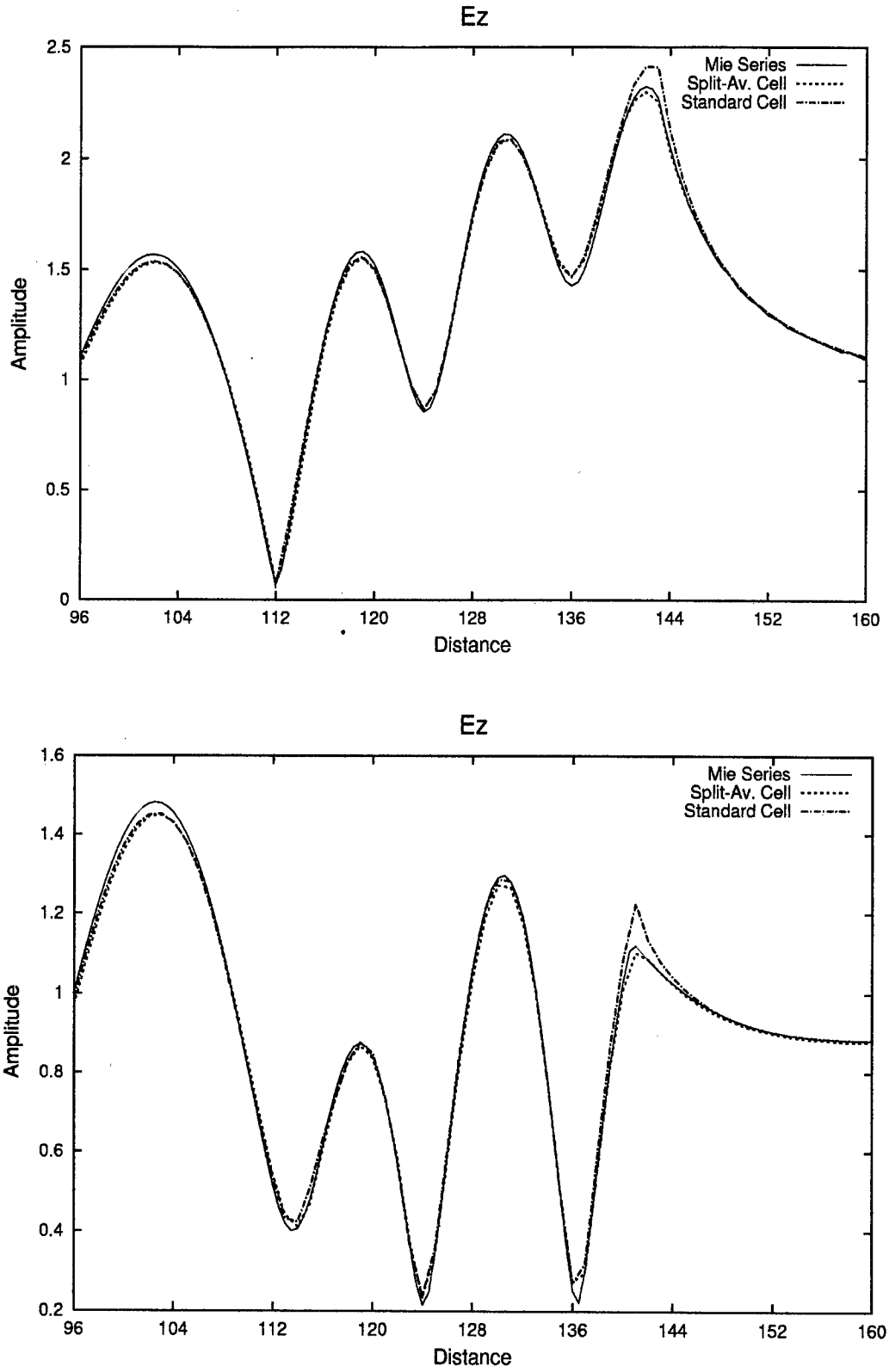

Figure 3a and 3b - Magnitude of E_z parallel to y-axis through (x=0, z=0) and (x=8,z=0). Solid line is exact Mie solution, long dash is standard cell and short dash is split-cell. The sphere is located between y=113 and y=143. Case I, f=2.5 GHz and ε=4.

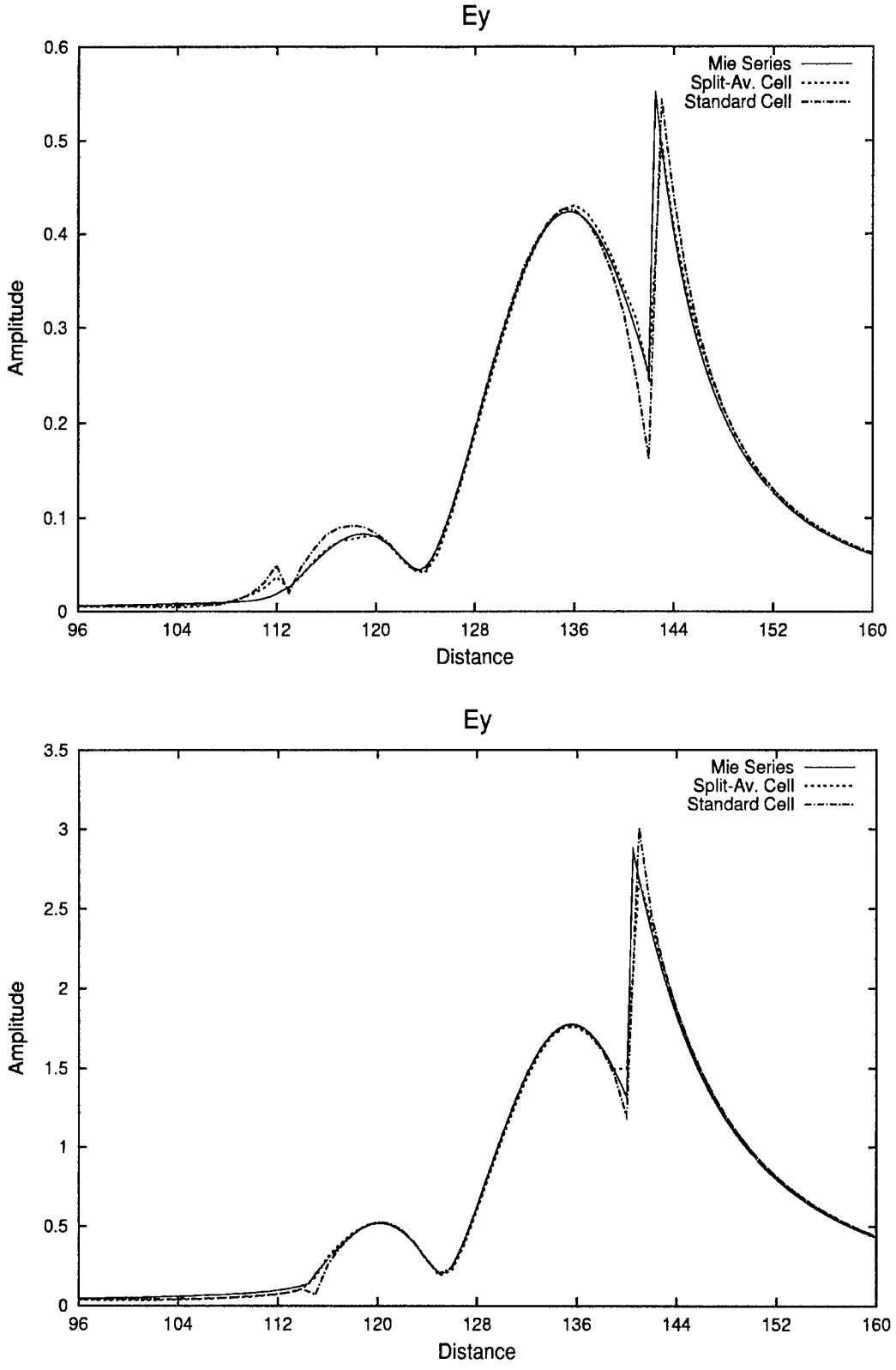

Figure 4a and 4b - Magnitude of E_y parallel to y-axis through (x=0,z=1) and (x=0,z=8). Case I, f=2.5GHz and ε=4.

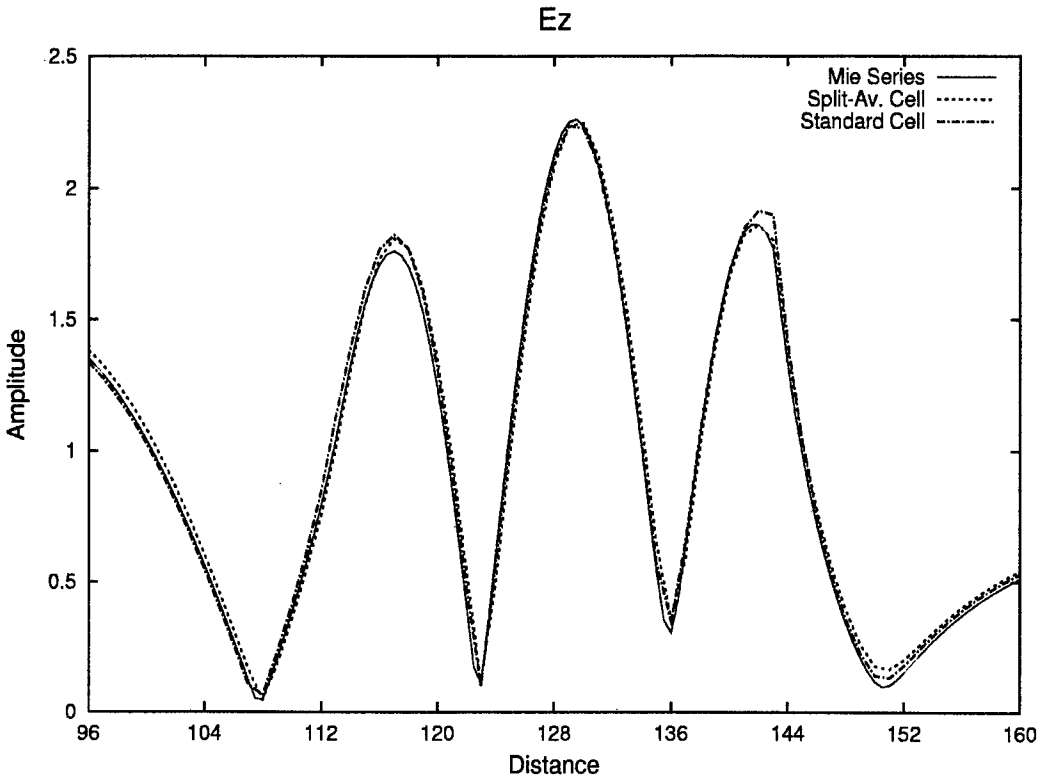

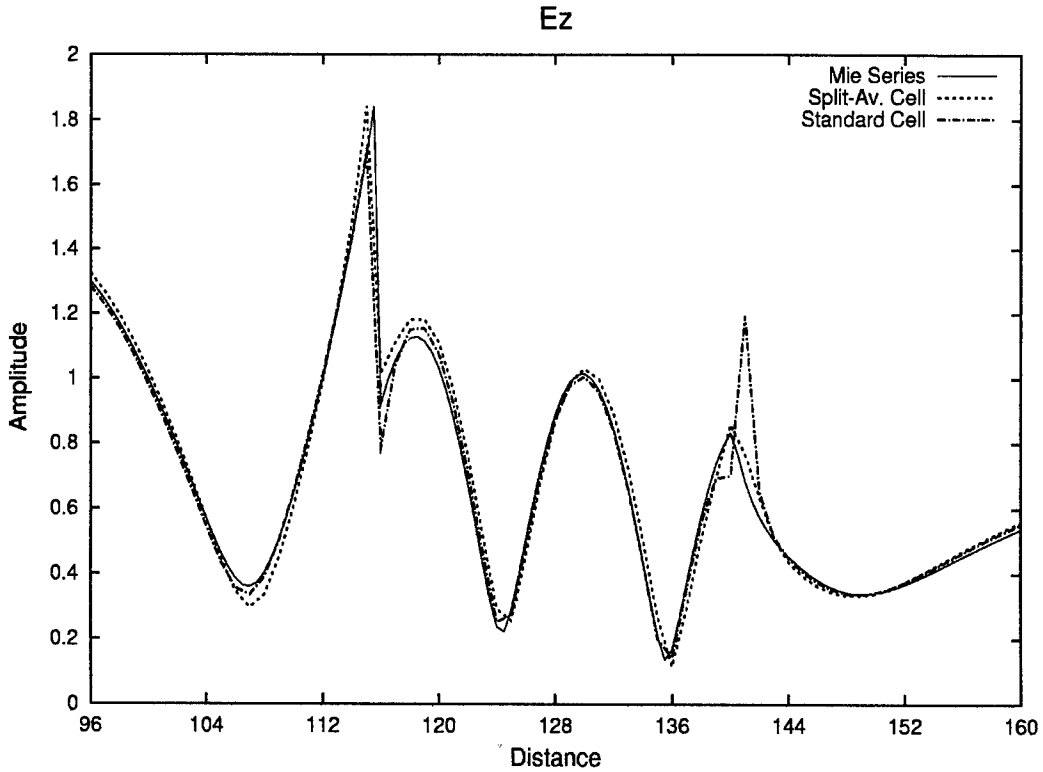

Figures 5a and 5b - Magnitude of E_z parallel to y-axis and through (x=0,z=0) and (x=0, z=8). Sphere is located between y=113 and y=143. Case II, f=1.767 GHz and ε=8.

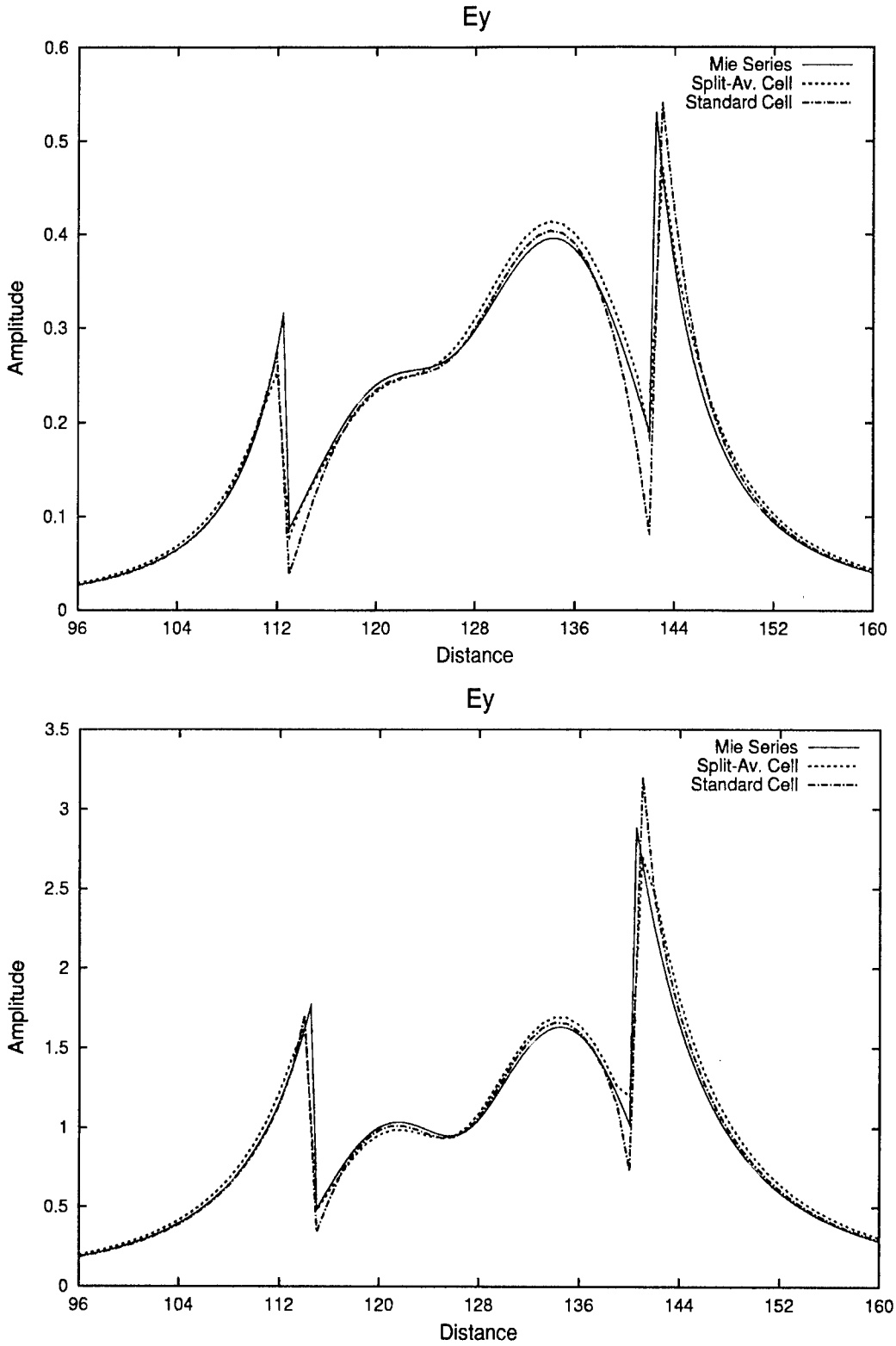

Figures 6a and 6b - Magnitude of E_y parallel to y-axis through (x=0,z=0) and (x=0,z=8). Sphere is located between y=113 and y=143. Case II, f=1.767 GHz and ε=8.

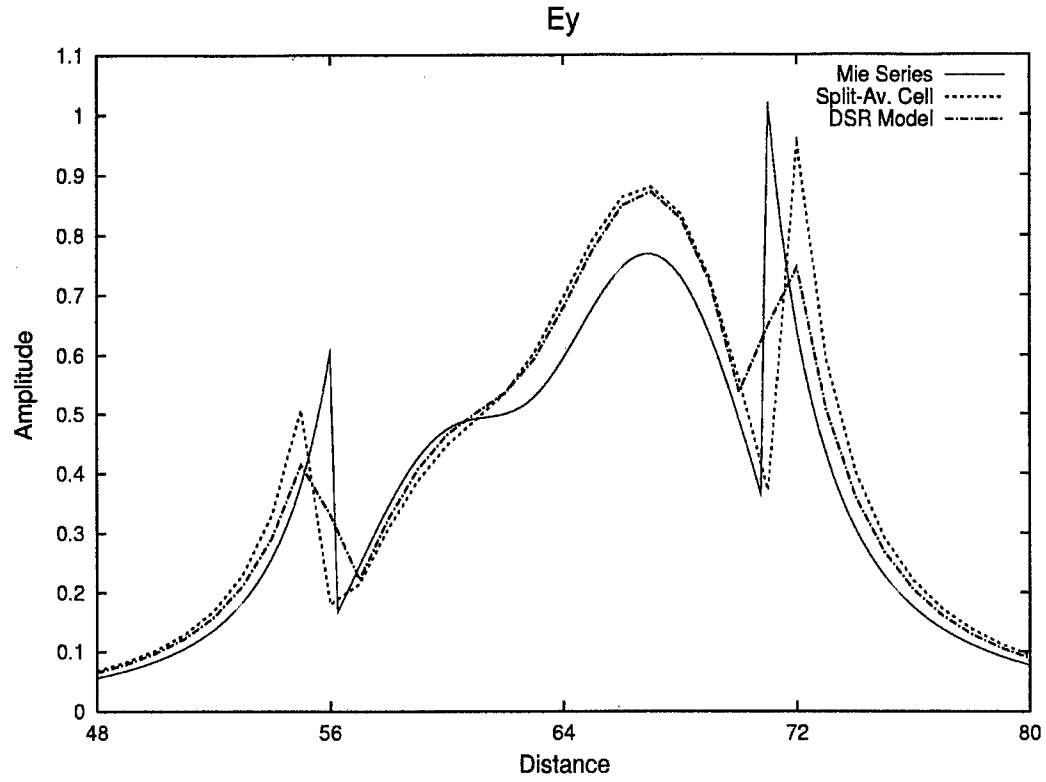

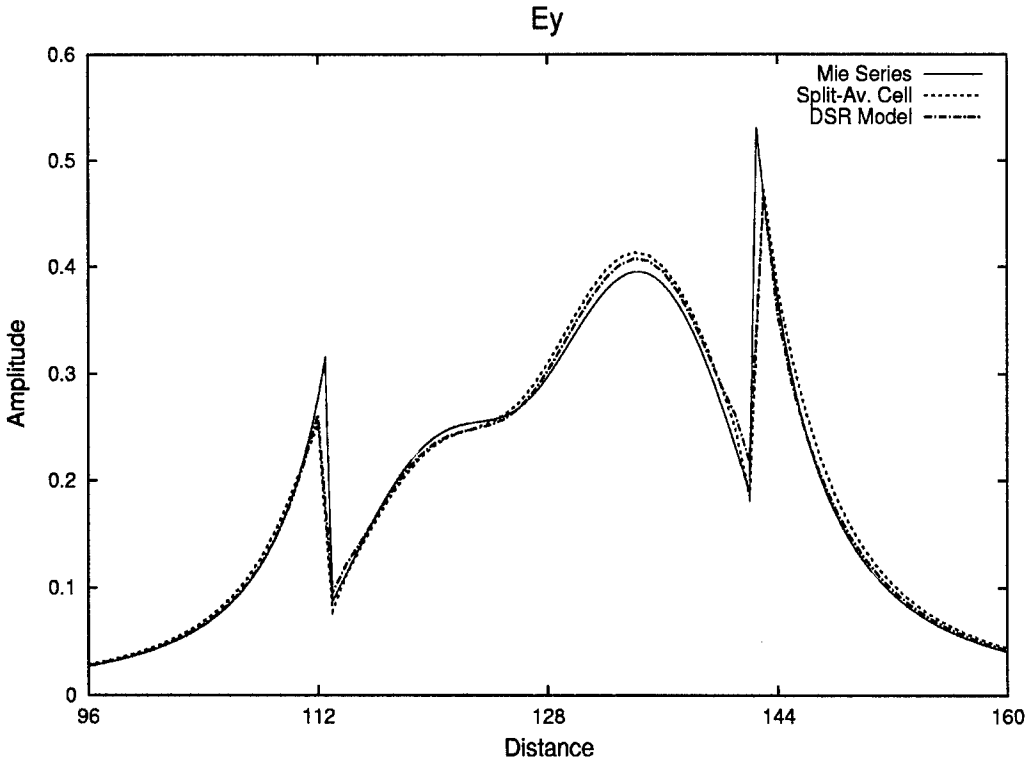

Figure 7a - Magnitude of E_y parallel to y-axis through (x=0,z=1). Compared are DSR and simple averaging. Case II, f=1.767 GHz, and ε=8, 10 points/wavelength. Figure 8b is same as 8a but with 20 points/wavelength.

Table I
Amplitudes of Transmitted and Reflected Waves
Second-Order, ε=4.0, 14°, λ/10

	Split Cell	Standard Cell	Exact
Transmitted Amplitude	.660 (.3%)	.655 (1.06%)	.662
Reflected Amplitude	-.335 (3.7%)	-.344 (6.5%)	-.323

Table II
Amplitudes of Transmitted and Reflected Waves
Second-Order, ε=8.0, 14°, λ/10

	Split Cell	Standard Cell	Exact
Transmitted Amplitude	.519 (0.0%)	.513 (1.16%)	.519
Reflected Amplitude	-.477 (1.9%)	-.484 (3.4%)	-.468

Table III
Amplitudes of Transmitted and Reflected Waves
Fourth-Order, ε=4.0, 14°, λ/7.5

	Split Cell	Standard Cell	Exact
Transmitted Amplitude	.660 (0.3%)	.643 (2.8%)	.662
Reflected Amplitude	-.325 (.6%)	-.351 (8.7%)	-.323

Table IV
Amplitudes of Transmitted and Reflected Waves
Fourth-Order, ε=8.0, 14°, λ/7.5

	Split Cell	Standard Cell	Exact
Transmitted Amplitude	.518 (0.3%)	.502 (3.3%)	.519
Reflected Amplitude	-.468 (0.0%)	-.494 (5.6%)	-.468

Mathieu Functions of Complex Argument and Their Applications to the Scattering by Lossy Elliptic Cylinders

A-K. Hamid
Department of Electrical /Electronics Engineering
University of Sharjah
P.O. Box 27272, Sharjah, United Arab Emirates
email: akhamid@sharjah.ac.ae

M. I. Hussein
Department of Electrical Engineering
United Arab Emirates University
P.O. Box 17555, Al-Ain, United Arab Emirates
email: MIHussein@uaeu.ac.ae

H. A. Ragheb
Department of Electrical Engineering
King Fahd University of Petroleum and Minerals
Dhahran, Saudi Arabia

M. Hamid
Department of Electrical and Computer Engineering
University of South Alabama
Mobile, Alabama 36688, U.S.A.
email: mhamid@usouthal.edu

Abstract

The aim of this paper is to outline the theory for calculating the angular and radial Mathieu functions of complex arguments. These functions are required for the computation of analytic solutions of electromagnetic scattering by lossy dielectric elliptic cylinders and waveguides. The backscattered echo width of a lossy dielectric elliptic cylinder is compared with the special case of lossy circular and weakly lossy elliptic cylinders and excellent agreement is obtained in all cases. Tabulated and plotted numerical results of typical Mathieu functions are presented.

1. Introduction

Many engineering and physics applications involve the solution of structures with elliptical geometries. Analytic solutions to such structures require the computation of angular and radial Mathieu functions in the elliptical coordinate system. Examples of such applications are the solution of elliptical waveguide problems [1-5], optical fibers [6], and elliptical loaded horn and corrugated elliptical horn antennas [2], field prediction inside lossy elliptic cylinders for biological body modeling [7], and scattering by mutilayered dielectric elliptic cylinders [8-12]. Furthermore, analytical solutions are generally needed to check the accuracy of numerical or approximate solutions.
Over the years many algorithms and programs have been developed to address the problem of computing Mathieu functions of integer and real arguments [4], [13-22]. However, none of these publications have addressed the more general problem of computing the angular and radial Mathieu functions of complex arguments. Caorsi et. al. have computed the solution of electromagnetic scattering by weakly lossy multilayer elliptic cylinders using first-order truncation of the Taylor expansion of each Mathieu function [23-24]. The same authors have presented the solution of the scattering of an electromagnetic wave by a lossy dielectric elliptic cylinder based on the exact Fourier series solution in terms of the Mathieu functions with complex argument [24]. Recently, Amendola outlined the theory for the computation of Mathieu functions of complex order by applying the Floquent theory [27]. Unfortunately, there are no numerical results for these functions given in the literature.
In this paper, the solution presented in [15] is extended to account for the characteristic values (eigenvalues) of Mathieu functions of complex argument. Once the characteristic values are computed, the complex Fourier coefficients of the Mathieu functions can be obtained. These coefficients are needed to compute the angular and radial Mathieu functions of complex arguments and their derivatives as will be shown.

2. Theoretical Background

The homogeneous wave equation (Helmholtz) in elliptical coordinates u, v, and z is given by

$$\frac{1}{F^2(\cosh^2 u-\cosh^2 v)}\left[\frac{\partial^2\psi}{\partial u^2}+\frac{\partial^2\psi}{\partial v^2}\right]+\left[\frac{\partial^2}{\partial z^2}+k^2\right]\psi=0 \quad (1)$$

The elliptical coordinate system (u,v,z) is defined in terms of the Cartesian coordinate system (x,y,z) by $x=F\cosh(u)\cos(v)$ and $y=F\sinh(u)\sin(v)$, where F is the semifocal length of the elliptical cross section. Assuming no variation of the function ψ along the *z-axis*, the z-derivative in (1) will drop out. The resulting differential equation can be separated into the following differential equations in terms of U(u) and V(v). The circumferential (ordinary) Mathieu's differential equation is

$$d^2V/dv^2+(a-2q\cos 2v)V=0 \quad (2)$$

and the radial (modified) Mathieu's differential equation is

$$d^2U/du^2-(a-2q\cosh 2u)U=0 \quad (3)$$

where $q=(kF)^2=q_R+jq_I$, $k=\omega\sqrt{\mu_1\varepsilon_1}$ and $\varepsilon_1=\varepsilon_1'-j\varepsilon_1''$.
It can be shown that there is a countable set of characteristic values of a, for which the solutions are π or 2π periodic.

One can easily distinguish between four kinds of characteristic values (eigenvalues) [15]:

$a = a_{2r}(q)$, even solution, period π

$a = a_{2r+1}(q)$, even solution, period 2π

$a = b_{2r+2}(q)$, odd solution, period π

$a = b_{2r+1}(q)$, odd solution, period 2π

$r = 0,1,2,...$

For every characteristic value, the solution of (2) can be given as a Fourier series:

$$Se_{2r}(v,q) = \sum_{m=0}^{\infty} A_{2m}^{2r} \cos 2mv \tag{4a}$$

$$Se_{2r+1}(v,q) = \sum_{m=0}^{\infty} A_{2m+1}^{2r+1} \cos(2m+1)v \tag{4b}$$

$$So_{2r+2}(v,q) = \sum_{m=0}^{\infty} B_{2m+2}^{2r+2} \sin(2m+2)v \tag{4c}$$

$$So_{2r+1}(v,q) = \sum_{m=0}^{\infty} B_{2m+1}^{2r+1} \sin(2m+1)v \tag{4d}$$

Where the A's and B's are complex Fourier coefficients. For computing the Fourier coefficients, one has to obtain first the characteristic values.

Substitution of the series (4a), (4b), (4c), and (4d) in the differential equation (2), yields four sets of equations for computing the Fourier coefficients:

$$\begin{bmatrix} a_{2r} & -q & 0 & & & \\ -2q & a_{2r}-4 & -q & & & \\ 0 & \ddots & \ddots & \ddots & 0 & \\ & & \ddots & \ddots & -q & \\ & & 0 & -q & a_{2r}-(2m)^2 & \end{bmatrix} \begin{bmatrix} A_0^{2r} \\ A_2^{2r} \\ \vdots \\ \vdots \\ A_{2m}^{2r} \end{bmatrix} = 0 \tag{5a}$$

$$\begin{bmatrix} a_{2r+1}-1-q & -q & 0 & & & \\ -q & a_{2r+1}-9 & -q & & & \\ 0 & \ddots & \ddots & \ddots & 0 & \\ & & \ddots & \ddots & -q & \\ & & 0 & -q & a_{2r+1}-(2m+1)^2 & \end{bmatrix} \begin{bmatrix} A_1^{2r+1} \\ A_3^{2r+1} \\ \vdots \\ \vdots \\ A_{2m+1}^{2r+1} \end{bmatrix} = 0 \tag{5b}$$

$$\begin{bmatrix} b_{2r+2}-4 & -q & 0 & & & \\ -q & b_{2r+2}-16 & -q & & & \\ 0 & \ddots & \ddots & \ddots & 0 & \\ & & \ddots & \ddots & -q & \\ & & 0 & -q & b_{2r+2}-(2m+2)^2 & \end{bmatrix} \begin{bmatrix} B_2^{2r+2} \\ B_4^{2r+2} \\ \vdots \\ \vdots \\ B_{2m+2}^{2r+2} \end{bmatrix} = 0 \tag{5c}$$

$$\begin{bmatrix} b_{2r+1}-1-q & -q & 0 & & & \\ -q & b_{2r+1}-9 & -q & & & \\ 0 & \ddots & \ddots & \ddots & 0 & \\ & & \ddots & \ddots & -q & \\ & & 0 & -q & b_{2r+1}-(2m+2)^2 & \end{bmatrix} \begin{bmatrix} B_1^{2r+1} \\ B_3^{2r+1} \\ \vdots \\ \vdots \\ B_{2m+1}^{2r+1} \end{bmatrix} = 0 \tag{5d}$$

We shall now show the computation of a_{2r+1} in (5b). All other characteristic values can be calculated in exactly the same way. It is clear from (5b) that a_{2r+1} can be seen as the eigenvalues of the infinite tridiagonal matrix,

$$\begin{bmatrix} 1+q & q & 0 & & & \\ q & 9 & q & & & \\ 0 & \ddots & \ddots & \ddots & 0 & \\ & & \ddots & \ddots & q & \\ & & 0 & q & (2m+1)^2 & \end{bmatrix} \tag{6}$$

In calculating the eigenvalues and Fourier coefficients, it is necessary to truncate the matrix after a finite number of columns and rows to obtain the required accuracy.

Once the coefficients A_{2m}^{2r}, A_{2m+1}^{2r+1}, B_{2m+2}^{2r+2}, B_{2m+1}^{2r+1} are determined using the routine DEVCCG from Microsoft IMSL Math Libraries, the angular Mathieu functions in equations (4) as well as their respective derivatives can be calculated. Next, we compute the radial Bessel functions of the first and second types using equation (3) along with the previously computed Fourier coefficients. The equations used for the computation of the even and odd functions of the first type are

$$J_{e2r}(u,q) = (-1)^r \sqrt{\pi/2} \sum_{m=0}^{M} (-1)^m A_{2m}^{2r} J_m(x_1) J_m(x_2) / A_0^{2r} \tag{7}$$

$$J_{e2r+1}(u,q) = (-1)^r \sqrt{\pi/2} \sum_{m=0}^{M} (-1)^m A_{2m+1}^{2r+1} [J_{m+1}(x_1) J_m(x_2) + J_m(x_1) J_{m+1}(x_2)] / A_1^{2r+1} \tag{8}$$

$$J_{o2r}(u,q) = (-1)^r \sqrt{\pi/2} \sum_{m=1}^{M} (-1)^m B_{2m}^{2r} [J_{m+1}(x_1) J_{m-1}(x_2) - J_{m+1}(x_1) J_{m-1}(x_2)] / B_2^{2r} \tag{9}$$

$$J_{o2r+1}(u,q) = (-1)^r \sqrt{\pi/2} \sum_{m=0}^{M} (-1)^m B_{2m+1}^{2r+1} [J_{m+1}(x_1) J_m(x_2) - J_m(x_1) J_{m+1}(x_2)] / B_1^{2r+1} \tag{10}$$

where $x_1 = \frac{\sqrt{q}}{2} e^{u}, x_2 = \frac{\sqrt{q}}{2} e^{-u}$. By replacing J_m by Y_m, we obtain the even and odd radial functions of the second type as follows

$$Y_{e2r}(u,q) = (-1)^r \sqrt{\pi/2} \sum_{m=0}^{M} (-1)^m A_{2m}^{2r} Y_m(x_1) J_m(x_2) / A_0^{2r} \tag{11}$$

$$Y_{e2r+1}(u,q) = (-1)^r \sqrt{\pi/2} \sum_{m=0}^{M} (-1)^m A_{2m+1}^{2r+1} [Y_{m+1}(x_1) J_m(x_2) + Y_m(x_1) J_{m+1}(x_2)] / A_1^{2r+1} \tag{12}$$

$$Y_{o2r}(u,q) = (-1)^r \sqrt{\pi/2} \sum_{m=1}^{M} (-1)^m B_{2m}^{2r} [Y_{m+1}(x_1) J_{m-1}(x_2) - J_{m+1}(x_1) Y_{m-1}(x_2)] / B_2^{2r} \tag{13}$$

$$Y_{o2r+1}(u,q) = (-1)^r \sqrt{\pi/2} \sum_{m=0}^{M} (-1)^m B_{2m+1}^{2r+1} [Y_{m+1}(x_1) J_m(x_2) - J_m(x_1) J_{m+1}(x_2)] / B_1^{2r+1} \tag{14}$$

Numerical results for the derivatives, with respect to q, of the even and odd angular and radial Mathieu functions are obtained using the equations given in [14-17].

3. Electromagnetic Scattering by a Lossy Dielectric Elliptic Cylinder

Consider the case of a linearly polarized electromagnetic plane wave incident on a lossy dielectric elliptic cylinder (of permeability μ, permitivity ε and conductivity σ) at an angle ϕ_i measured with respect to the x axis as shown in [25]. The electric field component of the TM polarized plane wave of amplitude E_0 is given by

$$E_z^i = E_0 e^{jk_o\rho\cos(\phi-\phi_i)} \tag{15}$$

where k_0 is the wave number in free space. The incident electric field may be expressed in terms of Mathieu functions as follows

$$E_z^i = \sum_{m=0}^{\infty} A_{em} R_{em}^{(1)}(c_0,\xi) S_{em}(c_0,\eta) + \sum_{m=1}^{\infty} A_{om} R_{om}^{(1)}(c_0,\xi) S_{om}(c_0,\eta) \tag{16}$$

$$A_{\substack{em\\om}} = E_0 j^m \frac{\sqrt{8\pi}}{N_{\substack{em\\om}}(c_0)} S_{\substack{em\\om}}(c_0,\cos\phi_i) \tag{17}$$

$$N_{\substack{em\\om}}(c) = \int_0^{2\pi} [S_{\substack{em\\om}}(c,\eta)]^2 dv \tag{18}$$

where $\xi = \cosh u$ and $\eta = \cos v$, $c_0 = k_0 F$, F is the semifocal length of the elliptical cross section, S_{em}, while S_{om} are the even and odd angular Mathieu functions of order m, respectively, $R_{em}^{(1)}$ and $R_{om}^{(1)}$ are the even and odd radial Mathieu functions of the first kind, and N_{em} and N_{om} are the even and odd normalized functions.

Electric field expansion inside and outside the lossy dielectric cylinder can be obtained by solving the Helmholtz equation in the elliptical coordinate system using the separation of variables technique. The scattered electric field outside the elliptic cylinder for $(\xi > \xi_1)$ can be expressed in terms of a sum series of Mathieu and modified Mathieu functions as follows

$$E_z^s = \sum_{m=0}^{\infty} B_{em} R_{em}^{(4)}(c_0,\xi) S_{em}(c_0,\eta) + \sum_{m=1}^{\infty} B_{om} R_{om}^{(4)}(c_0,\xi) S_{om}(c_0,\eta) \tag{19}$$

where B_{em} and B_{om} are the unknown scattered field expansion coefficients, $R_{em}^{(4)}$ and $R_{om}^{(4)}$ are the even and odd modified Mathieu functions of the fourth kind. Similarly, the transmitted electric field inside the cylinder for $\xi < \xi_1$ can be written as

$$E_z^t = \sum_{m=0}^{\infty} C_{em} R_{em}^{(1)}(c_1,\xi) S_{em}(c_1,\eta) + \sum_{m=1}^{\infty} C_{om} R_{om}^{(1)}(c_1,\xi) S_{om}(c_1,\eta) \tag{20}$$

where $c_1 = k_1 F$ is complex, and $k_1 = \omega\sqrt{\mu_1\varepsilon_1}$. $\varepsilon_1 = \varepsilon_1' - j\varepsilon_1''$, C_{em} and C_{om} are the unknown transmitted field expansion coefficients. The magnetic field component inside and outside the cylinder can be obtained using Maxwell's equations, i.e.

$$H_u = \frac{-j}{\omega\mu_1 h}\frac{\partial E_z}{\partial v} \tag{21}$$

$$H_v = \frac{-j}{\omega\mu_1 h}\frac{\partial E_z}{\partial u} \tag{22}$$

$$h = F\sqrt{\cosh^2 u - \cos^2 v} \tag{23}$$

The unknown expansion coefficients can be obtained by imposing the continuity of the tangential field components at surface of the cylinder $\xi = \xi_1$, i.e.

$$\sum_{m=0}^{\infty} M_{enm}(c_1,c_0) B_{em}\left[\mu_r R_{em}^{(4)'}(c_0,\xi_1) - R_{em}^{(4)}(c_0,\xi_1)\frac{R_{en}^{(1)'}(c_1,\xi_1)}{R_{en}^{(1)}(c_1,\xi_1)}\right] = \sum_{m=0}^{\infty} M_{enm}(c_1,c_0) A_{em}\left[R_{em}^{(1)}(c_0,\xi_1)\frac{R_{en}^{(1)'}(c_1,\xi_1)}{R_{en}^{(1)}(c_1,\xi_1)} - \mu_r R_{em}^{(1)'}(c_0,\xi_1)\right] \tag{24}$$

$$\sum_{m=1}^{\infty} M_{onm}(c_1,c_0) B_{om}\left[\mu_r R_{om}^{(4)'}(c_0,\xi_1) - R_{om}^{(4)}(c_0,\xi_1)\frac{R_{on}^{(1)'}(c_1,\xi_1)}{R_{on}^{(1)}(c_1,\xi_1)}\right] = \sum_{m=0}^{\infty} M_{onm}(c_1,c_0) A_{om}\left[R_{om}^{(1)}(c_0,\xi_1)\frac{R_{on}^{(1)'}(c_1,\xi_1)}{R_{on}^{(1)}(c_1,\xi_1)} - \mu_r R_{om}^{(1)'}(c_0,\xi_1)\right] \tag{25}$$

$$M_{\substack{enm\\onm}}(c_0,c_1) = \int_0^{2\pi} S_{\substack{em\\om}}(c_1,\eta) S_{\substack{en\\on}}(c_0,\eta) dv \tag{26}$$

where μ_r is the relative permeability of the dielectric region. The TE scattering by a lossy elliptic cylinder is also presented. In this case a derivation dual to that of the TM case leads to the following solution [25]

$$\sum_{m=0}^{\infty} M_{enm}(c_1,c_0) B_{em}^{TE}\left[\varepsilon_r R_{em}^{(4)'}(c_0,\xi_1) - R_{em}^{(4)}(c_0,\xi_1)\frac{R_{en}^{(1)'}(c_1,\xi_1)}{R_{en}^{(1)}(c_1,\xi_1)}\right] = \sum_{m=0}^{\infty} M_{enm}(c_1,c_0) A_{em}\left[R_{em}^{(1)}(c_0,\xi_1)\frac{R_{en}^{(1)'}(c_1,\xi_1)}{R_{en}^{(1)}(c_1,\xi_1)} - \varepsilon_r R_{em}^{(1)'}(c_0,\xi_1)\right] \tag{27}$$

$$\sum_{m=1}^{\infty} M_{onm}(c_1,c_0) B_{om}^{TE}\left[\varepsilon_r R_{om}^{(4)'}(c_0,\xi_1) - R_{om}^{(4)}(c_0,\xi_1)\frac{R_{on}^{(1)'}(c_1,\xi_1)}{R_{on}^{(1)}(c_1,\xi_1)}\right] = \sum_{m=0}^{\infty} M_{onm}(c_1,c_0) A_{om}\left[R_{om}^{(1)}(c_0,\xi_1)\frac{R_{on}^{(1)'}(c_1,\xi_1)}{R_{on}^{(1)}(c_1,\xi_1)} - \varepsilon_r R_{om}^{(1)'}(c_0,\xi_1)\right] \tag{28}$$

The scattered near and far fields for the TM and TE cases can be calculated once the scattered fields expansion coefficients are known. The far scattered field expressions can be obtained as follows

$$E_z^s = \sqrt{\frac{j}{k_0\rho}} e^{-jk_0\rho} \sum_m j^m \left[B_{em}^{TM} S_{em}(c_0,\eta) + B_{om}^{TM} S_{om}(c_0,\eta)\right] \quad (29)$$

$$H_z^s = \sqrt{\frac{j}{k_0\rho}} e^{-jk_0\rho} \sum_m j^m \left[B_{em}^{TE} S_{em}(c_0,\eta) + B_{om}^{TE} S_{om}(c_0,\eta)\right] \quad (30)$$

Far Field data are usually expressed in terms of the scattering cross section per unit length, *i.e.*, the echo width. For the TM polarization case it is defined as

$$\sigma_{TM} = 2\pi\rho \lim_{\rho\to\infty} \frac{\left|E_z^s\right|^2}{\left|E_z^i\right|^2} \quad (31)$$

Eq. (30) can be put in simpler form for the purpose of computation as follows

$$\sqrt{\frac{\sigma_{TM}}{\lambda}} = \sum_m j^m \left[B_{em} S_{em}(c_0,\eta) + B_{om} S_{om}(c_0,\eta)\right] \quad (32)$$

4. Numerical Results

To determine the accuracy of the computer program, the Fourier expansion coefficients of Mathieu functions are computed. These results are in excellent agreement with those given in [16] for the case of real positive argument q, and the maximum difference was found to be 10^{-5}. Also, to verify the accuracy of the computer program for the case of complex argument q, we solved the problem of electromagnetic scattering by a lossy dielectric elliptic cylinder since no results are available in the literature. The computed numerical results were compared with the special case of scattering by a lossy circular dielectric cylinder, and with electromagnetic scattering by weakly lossy multilayer elliptic cylinder [23,26]. Fig. 1 shows the numerical results of the scattered normalized echo width σ of a lossy dielectric circular cylinder having a relative permittivity of $\varepsilon_r = 1 - j11.3$ and electrical radius $k_0 a = 3.33$ for TM and TE polarizations. These results compare very well with those presented in [26]. In this case the circular cylinder was approximated using an axial ratio close to 1, and was excited by an incident plane wave with $\phi_i = 180^o$.

Fig. 2 compares the back scattering normalized echo width $k_0\sigma(0)/4$ for a homogeneous elliptical cylinder with axial ratio $a/b = 2$ and $\varepsilon' = 4.0$. Two cases are studied; these are the lossless cylinder case with $\varepsilon'' = 0.0$ and a weak loss cylinder case where $\varepsilon'' = 0.6$. The calculated results are in very good agreement with those published in [23]. One can easily recognize the reduction in the back scattering normalized echo width due to the presence of a small loss. This can be attributed to the fact that the weak loss material absorbed part of the incident wave energy. Another clear observation is the shift in of resonance location. For a free loss material, resonance is observed around $k_0 a$ =3.6, while in the weak loss case the resonance has shifted to around $k_0 a$ =2.1. Fig. 3 illustrates the results obtained in [16] for the radial Mathieu function of the first kind and zero order with respect to u for different values of q, and presented here to validate the accuracy of the computer code. Finally, Figs. 4-13 present a collection of data for Mathieu functions (radial and angular) of complex arguments. The Fourier expansion coefficients of Mathieu functions for different arguments are tabulated in Tables 1-4. These results should be very helpful for researchers solving problems in the elliptic coordinate system.

5. Conclusions

The theory for calculating the angular and radial Mathieu functions of complex arguments has been outlined. The computed backscattered echo width of a lossy dielectric elliptic cylinder was compared with the special case of lossy circular and weakly lossy elliptic cylinders and the results are in complete agreement. Selected numerical results for Mathieu functions are plotted and tabulated for limited ranges due to limitation on space.

ACKNOWLEDGEMENT

The authors wish to acknowledge the support provided by the University of Sharjah, the United Arab Emirates University and the University of South Alabama. Also the first and third authors wish to acknowledge King Fahd University of Petroleum and Minerals in Saudi Arabia where the special case of Mathieu Functions of real argument was treated in a project entitled "Propagation and Radiation from Elliptical Waveguide Partly Filled with Nonconfocal Dielectric," by H. Ragheb and A-K. Hamid, 2000.

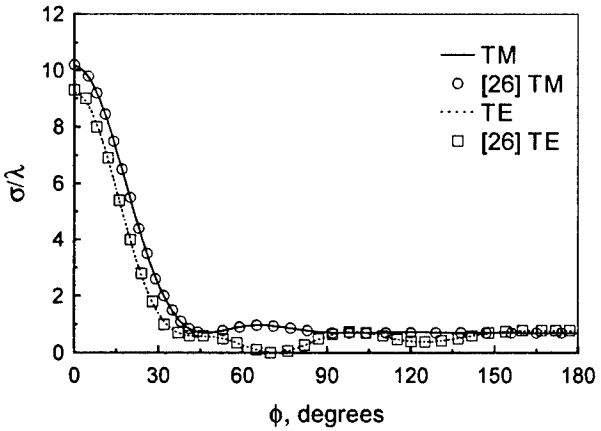

Figure 1: TM and TE Normalized backscattered echo width versus ϕ of a lossy circular cylinder with $k_0 a = 3.33$ and $\varepsilon_r = 1 - j11.3$.

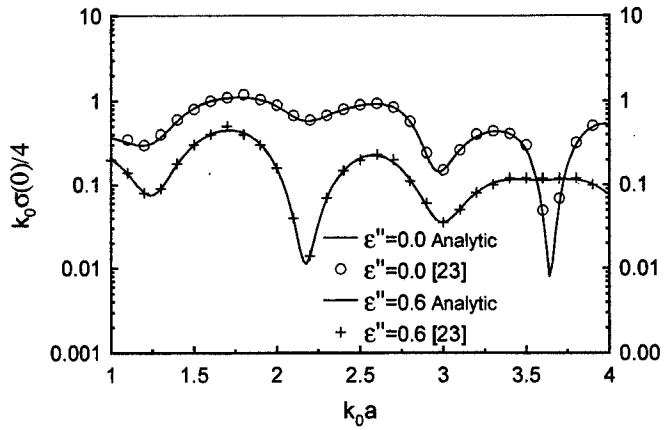

Figure 2: TM Normalized backscattered echo width versus ϕ of a lossy dieletric elliptic cylinder with $\varepsilon_r' = 4$, a/b=2 and $\phi_i = 0^o$

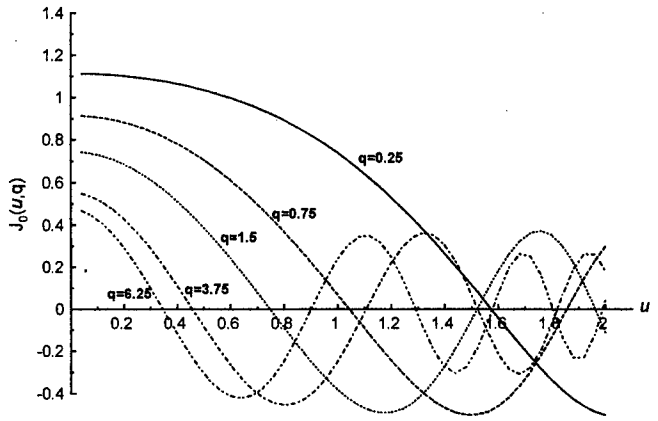

Figure 3: Radial Mathieu function of the first kind and zero order vs u for different values of q.

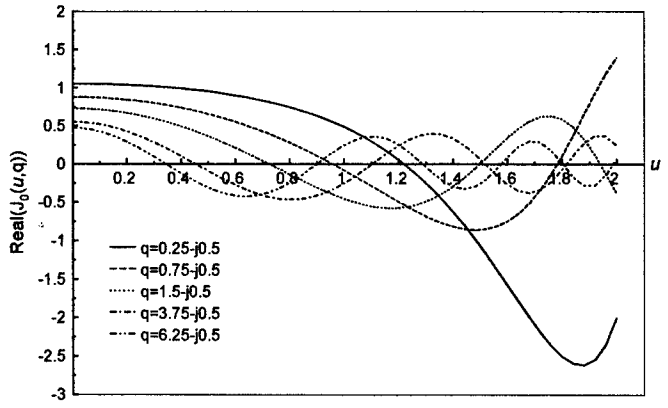

Figure 4: Real part of the radial Mathieu function of the first kind and zero order vs u for different values of complex q.

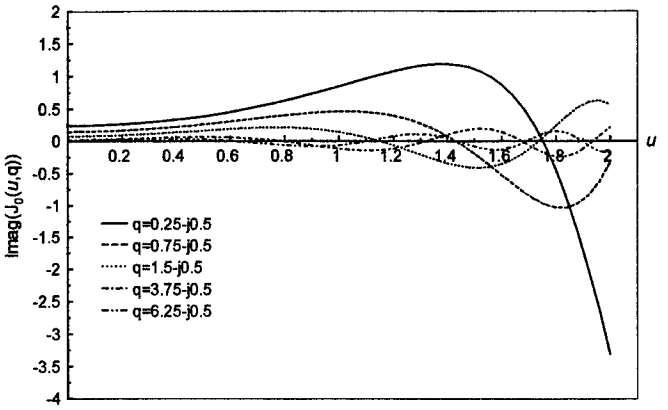

Figure 5: Imaginary part of radial Mathieu function of the first kind and zero order vs u for different values of q.

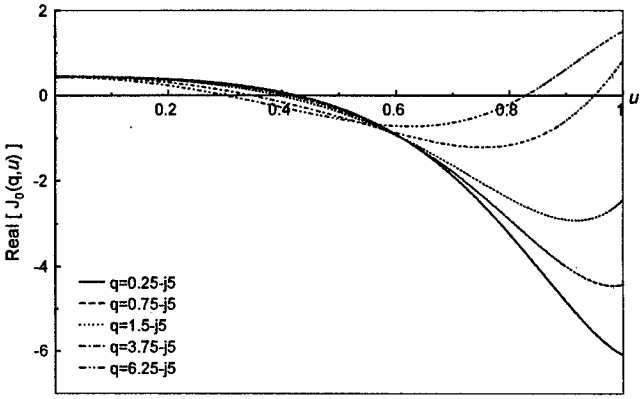

Figure 6: Real part of the radial Mathieu function of the first kind and zero order vs u for different values of q.

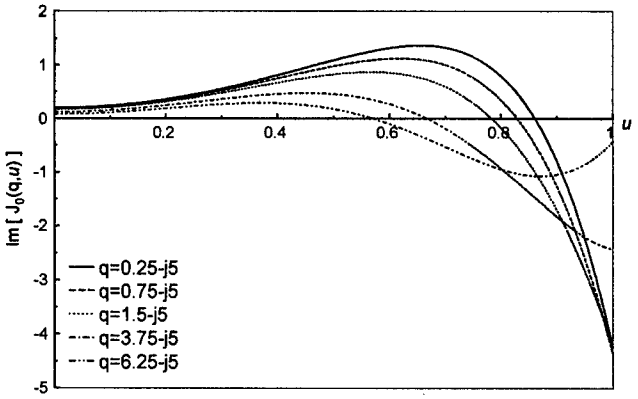

Figure 7: Imaginary part of the radial Mathieu function of the first kind and zero order vs u for different values of complex q.

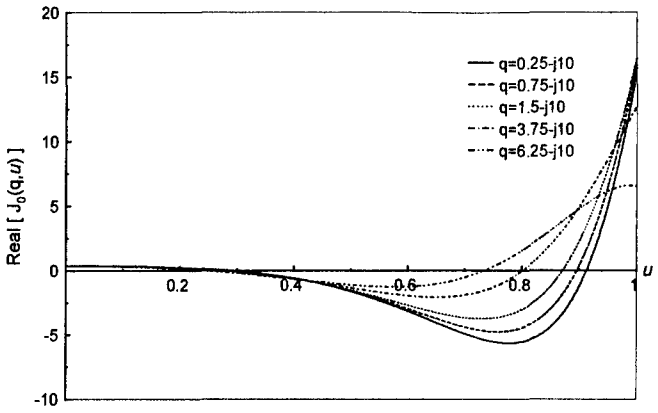

Figure 8: Real part of the radial Mathieu function of the first kind and zero order vs u for different values of q.

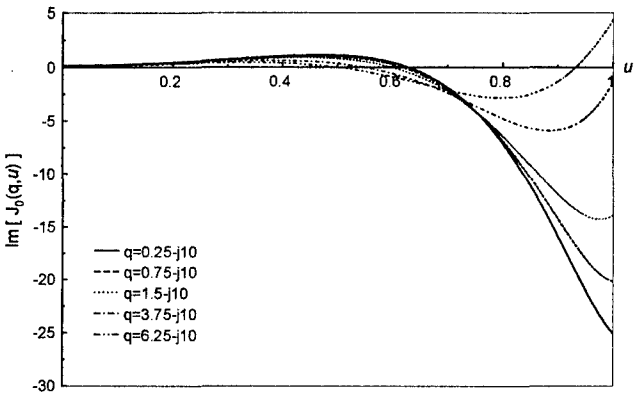

Figure 9: Imaginary part of the radial Mathieu function of the first kind and zero order vs u for different values of q.

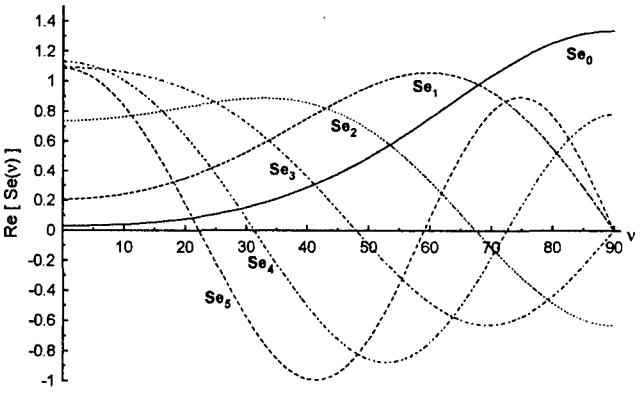

Figure 10: Real part of even periodic Mathieu function with orders 0-5 and $q = 5 - j2$ vs v.

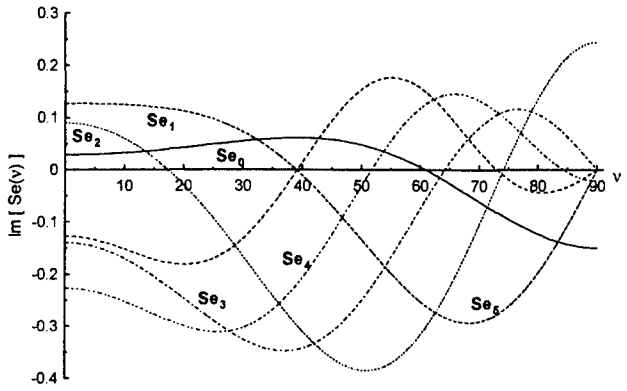

Figure 11: Imaginary part of even periodic Mathieu function with orders 0-5 and $q = 5 - j2$ vs v.

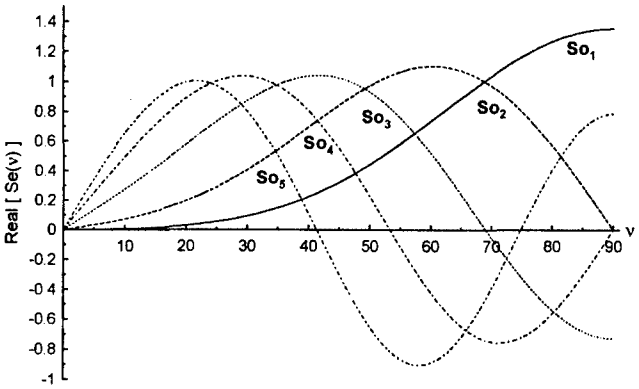

Figure 12: Real part of odd periodic Mathieu function with orders 1-5 and $q = 5 - j5$ vs v.

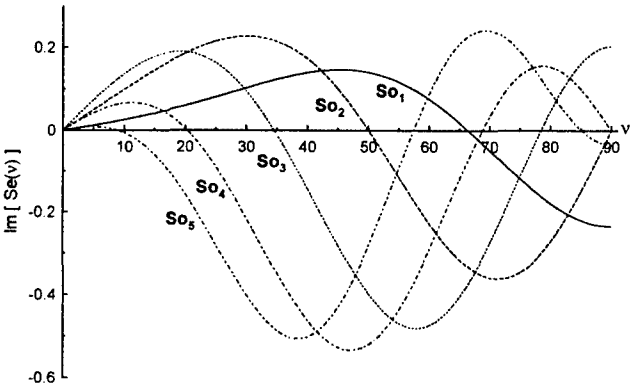

Figure 13: Imaginary part of odd periodic Mathieu function with orders 1-5 and $q = 5 - j5$ vs v.

Table 1: Complex Fourier expansion coefficients of even-even Mathieu function (A_{2m}^{2r})

A_{2m}^{2r}

	$m \setminus r$	0		2	
$q=5+j0$		*Real*	*Imag.*	*Real*	*Imag.*
	0	0.540612446	0	0.438737166	0
	2	-0.627115413	0	0.65364026	0
	4	0.14792709	0	-0.426578935	0
	6	-0.017848061	0	0.075885673	0
$q=5+j5$					
	0	0.49810151	0	0.314442843	0.171487341
	2	-0.662750285	-0.130176082	0.604942355	0
	4	0.168770876	0.133382581	0.026159729	-0.59020582
	6	-0.010394981	-0.034782531	-0.140969223	0.089859201
$q=10+j10$					
	0	-0.44951258	0.056260383	-0.294924019	0.029961136
	2	0.694591697	0	-0.059497099	0.255064311
	4	-0.296630326	-0.105862211	0.746844887	0
	6	0.058531831	0.064924524	-0.323904602	-0.281747705

Table 2: Complex Fourier expansion coefficients of even-odd Mathieu function (A_{2m+1}^{2r+1})

A_{2m+1}^{2r+1}

	$m \setminus r$	1		3	
$q=5+j0$		*Real*	*Imag.*	*Real*	*Imag.*
	1	0.762463687	0	0.077685798	0
	3	-0.63159632	0	0.30375103	0
	5	0.139684806	0	0.927728396	0
	7	-0.014915596	0	-0.201706148	0
$q=5+j5$					
	1	-0.517275706	0.286011205	-0.041658559	0.131675807
	3	0.765785524	0	0.239854654	0.290697818
	5	-0.197812838	-0.153451695	0.878673205	0
	7	0.007517743	0.03807304	-0.166961766	-0.194677341
$q=10+j10$					
	1	-0.433393417	0.130050198	0.666818493	0
	3	0.775016392	0	0.494260893	-0.299695541
	5	-0.373034841	-0.201569455	-0.01872188	-0.426395143
	7	0.054220182	0.106990887	-0.184358865	0.054869005

Table 3: Complex Fourier expansion coefficients of odd-even Mathieu function (B_{2m}^{2r})

B_{2m}^{2r}

	$m \setminus r$	2		10	
$q=5+j0$		*Real*	*Imag.*	*Real*	*Imag.*
	2	0.933429442	0	0.000033444	0
	4	-0.354803915	0	0.000642976	0
	6	0.052963729	0	0.010784806	0
	8	-0.004295885	0	0.13767512	0
$q=5+j5$					
	2	0.870294564	0	-0.000130329	-0.000002685
	4	-0.396630117	-0.272694975	-0.001280155	0.001222013
	6	0.028211436	0.099835145	-0.000421242	0.021019319
	8	0.0053059	-0.01083967	0.132565552	0.136516812
$q=10+j10$					
	2	0.734255554	0	-0.001900098	-0.000156527
	4	-0.580164625	-0.25100546	-0.009959144	0.008264692
	6	0.137051442	0.19916337	-0.006136282	0.076604876
	8	0.002015162	-0.052591626	0.231256474	0.260037365

Table 4: Complex Fourier expansion coefficients of odd-odd Mathieu function (B_{2m+1}^{2r+1})

B_{2m+1}^{2r+1}

	$m \setminus r$	1		3	
$q=5+j0$		*Real*	*Imag.*	*Real*	*Imag.*
	1	0.940019022	0	0.050382462	0
	3	-0.336541963	0	0.297365513	0
	5	0.055477529	0	0.931566996	0
	7	-0.005089553	0	-0.202193639	0
$q=5+j5$					
	1	0.904373155	0	0.016113831	0.092448918
	3	-0.389707951	-0.145292103	0.268912553	0.288134908
	5	0.057923929	0.074976514	0.87655541	0
	7	-0.000091975	-0.012224892	-0.16648902	-0.196783024
$q=10+j10$					
	1	0.852110863	0	-0.043283898	0.203330605
	3	-0.460992769	-0.18202088	0.234907973	0.510680316
	5	0.083408677	0.142179121	0.741126923	0
	7	0.009774806	-0.031241645	-0.081180316	-0.285889059

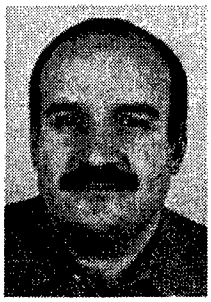

A.-K. Hamid was born in Tulkarm, WestBank, on Sept. 9, 1963. He received the B.Sc. degree in Electrical Engineering from West Virginia Tech, West Virginia, U.S.A. in 1985. He received the M.Sc. and Ph.D. degrees from the university of Manitoba, Winnipeg, Manitoba, Canada in 1988 and 1991, respectively, both in Electrical Engineering. From 1991-1993, he was with Quantic Laboratories Inc., Winnipeg, Manitoba, Canada, developing two and three dimensional electromagnetic field solvers using boundary integral method. From 1994-2000 he was with the faculty of electrical engineering at King Fahd University of Petroleum and Minerals, Dhahran, Saudi Arabia. Since Sept. 2001 he is an associate Prof. in the electrical\electronics and computer engineering at the University of Sharjah, Sharjah, United Arab Emirates. His research interest includes EM wave scattering from two and three dimensional bodies, propagation along waveguides with discontinuities, FDTD simulation of cellular phones, and inverse scattering using neural networks.

Mousa I. Hussein received the B.Sc. degree in electrical engineering from West Virginia Tech, USA, 1985, M.Sc. and Ph.D. degrees from University of Manitoba, Winnipeg, MB, Canada, in 1992 and 1995, respectively, both in electrical engineering. From 1995 to 1997, he was with research and development group at Integrated Engineering Software Inc., Winnipeg, Canada, working on developing EM specialized software based on the Boundary Element method. In 1997 he joined faculty of engineering at Amman University, Amman, Jordan, as an Assistant Professor. He is currently with the Electrical Engineering Dept. at the United Arab Emirates University. Dr. Hussein current research interests includes, computational electromagnetics, electromagnetic scattering, antenna analysis and design, EMI and signal integrity.

Hassan Ragheb was born in Port-Said, Egypt, in 1953. He received the B. Sc. Degree in Electrical Engineering from Cairo University, Egypt, in 1977 and the M. Sc. and Ph. D. degrees in Electrical Engineering from the University of Manitoba, Winnipeg, Canada, in 1984 and 1987, respectively. From 1987 to 1989, he was a research assistant in the Department of Electrical Engineering, University of Manitoba. In 1989, he joined the Department of Electrical Engineering at the King Fahd University of Petroleum and Minerals, where he is now an Associate Professor of Electrical Engineering. His research interests include electromagnetic scattering by multiple and coated objects, microstrip antennas, phased arrays, slot and open ended waveguide antennas.

Michael Hamid Graduated from McGill University in Montreal with a B.Eng. degree in 1960, a M.Eng. degree in 1962 and from the University of Toronto with a Ph.D. degree in 1966, all in Electrical Engineering. He joined the University of Manitoba in 1965 where he became a Professor of Electrical Engineering and head of the Antenna Laboratory. He was a Visiting Professor at the Universities of California Davis and Central Florida and is presently a Professor of Electrical Engineering at the University of South Alabama. He is a past president of the International Microwave Power Institute, a Fellow of IEE and IEEE and published 307 referred articles and 25 patents.

References

1. Kretzchmar, J. G., "Wave propagation in conducting elliptical waveguides," IEEE Trans. Microwave Theory Tech., vol. MTT-18, pp. 547-554, 1970.
2. Clarricoats, P. J. B., and Olver, A. D., "Corrugated Horns for Microwave Antennas," Stevenage, U.K., Peregrinus, 1984.
3. Matras, P., Bunger, R., and Arndt, F., "Analysis of the step discontinuity in elliptical waveguides," IEEE Microwave Guided Wave Lett., vol. 6, pp. 143-145, Mar., 1996.
4. Schneider, M., Marquardt, J., "Fast Computation of Modified Mathieu Functions Applied to Elliptical Waveguide Problems," IEEE Trans. Microwave Theory Tech., vol. 47, pp. 513-515, 1999.
5. James. L. G., "Propagation and Radiation from partly filled elliptical waveguide," Proc. IEE, vol. 136, pt. H, pp. 195-201, June 1989.
6. Dyott, R. B., "Elliptical Fiber waveguides," Norwood, MA, Artech House, 1995.
7. Caorsi, S, Pastorino, M., and Raffetto, M, "EM Field Prediction Inside Lossy Multilayer Elliptic Cylinders for Biological-Body Modeling and Numerical-Procedure Testing," IEEE Trans. Biomedical Eng., Vol. 11, pp. 1304-1309, 1999.
8. Sebak, A-R., "Scattering from dielectric coated impedance elliptic cylinder," IEEE Trans. On Antenna and Prog., vol. 48, pp. 1574-1580, 2000.
9. R. Holand and V.P. Cable, "Mathieu functions and their applications to scattering by a coated strip," IEEE Trans. On Elect. Compt., vol. 34, no. 1, pp. 9-16, 1992.
10. Caorsi, S, Pastorino, M., and Raffetto, M., "Electromagnetic scattering by a multilayer elliptic cylinder under transverse-magnetic illumination: series

solution in terms of Mathieu function," IEEE Trans. On Antenna and Prog., vol. 45, no. 6, pp. 926-935, 1997.
11. Sebak, A., Shafai, L., and Ragheb, H., "Electromagnetic scattering by a two layered piecewise homogeneous confocal elliptic cylinder," Radio Science, vol. 26, pp. 111-119, 1991.
12. Kim, S.K., and Yeh, C., "Scattering of an obliquely incident wave by a multilayered elliptical lossy dielectric cylinder," Radio Science, vol. 26, pp. 1165-1176, 1991.
13. Rengarajan, S.R., and Lewis, J.E., "Mathieu functions of integral order and real arguments," IEEE Trans. Microwave Theory Tech., vol. MTT-28, pp. 276-277, 1980.
14. Toyama, N., and Shogen, K., "Computation of the value of the even and odd Mathieu functions of order N for a given parameter S and argument X," IEEE Trans. On Antennas and Propag., vol. AP-32, pp. 537-539, 1984.
15. "The "Numerical analysis" Group" at Delft University of Technology, "On the computation of Mathieu functions," Journal of Engineering Mathematics, vol. 7, pp. 39-61, 1973.
16. Abramowitz, M., and Stegun, I., Handbook of Mathematical Functions N.B.S, Applied Mathematical series 55, U.S. Government Printing Office, Washington D.C., 1964.
17. National Bureau of Standards, "Tables relating to Mathieu functions, characteristic values, coefficients, and joining factors," Columbia University Press 13, August 1967.
18. Leeb, Algorithm 537: Characteristic values of Mathieu's differential equation ACM Trans. Mah. Softw. , 5, pp 112-117, 1979
19. Alhargan, F. A., "A complete method for the computation of Mathieu characteristic numbers of integer order," SIAM Rev. 38, 2, 239-255, 1996".
20. Shirts, R.B. Algorithm 721: "MTIEU1 and MTIEU2 two subroutines to compute eigenvalues and solutions to Mathieu's differential equation for noninteger and integer order", ACM Trans. Math. Softw. , 19, 3, 276-277 1993
21. Zhang, S. and Jin, J., Computation of special functions (John Wiley & Sons, New York, USA, 1996)
22. Alhargan, F. A.," Algorithms of all Mathieu Functions of integer order", ACM Trans. Mah. Softw. , 26, pp. 390-407, 2000.
23. Caorsi, S, Pastorino, M., and Raffetto, M., "Electromagnetic scattering by weakly lossy multilayer elliptic cylinders," IEEE Trans. On Antennas and Prog., vol. 46, no. 11, pp. 1750-1751, 1998.
24. S. Caorsi, M. Pastorino, and M. Raffetto, "Radar cross section per unit length of a lossy multilayer elliptic cylinder," Microwave and Optical Technology Letters, vol. 21, pp. 380-384, 1999.
25. Hussein, M.I., and Hamid A.-K., "Electromagnetic Scattering by a Lossy Dielectric Cylinder", J. of Electromagn. Waves and Appl., vol. 15, No.11, 1469-1482, 2001.
26. Ouda, M., Sebak, A., "Scattering from lossy dielectric cylinders using a multifilament current model with impedance boundary conditions," IEE Proceedings, Microwaves, Antennas and Propagation, vol. 139, no. 5 , pp. 429 –434, Oct. 1992.
27. Amendola, G., "Application of Mathieu functions to the analysis of radiators conformal to elliptic cylindrical surfaces," J. of Electromagn. Waves and Appl., vol. 13 No.11, 1403-1120, 1999.

Reducing Electromagnetic Coupling in Shielded Enclosures using a Genetic Algorithm – Finite-Difference Time-Domain Solver

Russell Iain Macpherson[1] and Nick J Ryan[2]
Department of Engineering
King's College
University of Aberdeen
Aberdeen AB24 3UE
United Kingdom
r.macpherson@ieee.org[1], n.j.ryan@eng.abdn.ac.uk[2]

Abstract: Comprehensive shielding in modern electronic equipment may lead to resonant behaviour within the equipment enclosure. This paper presents a method for optimising the placement of sources of electromagnetic (EM) energy and susceptors to this EM energy within an enclosed resonant cavity. The source and susceptor are placed on a dielectric slab within a perfectly conducting enclosure to reduce the level of EM coupling between the two. Optimisation is facilitated using a genetic algorithm coupled with a finite-difference time-domain solver. Results are presented for single objective optimisation and multi-objective optimisation cases.

1 Introduction

The explosive increase in the use of electronic equipment in the information age has led to electromagnetic compatibility (EMC) and electromagnetic interference (EMI) issues becoming more important to designers of electronic equipment. These issues must be considered at the time of design and not once designs are at the prototype stage. Higher clock speeds and faster switching transitions lead to greater levels of electromagnetic emissions, while higher component integration and lower power demands lead to greater sensitivity. So at once systems are becoming more prone to generating and also more sensitive towards EMI.

An area of interest to the authors is electronic enclosures and the placement of devices inside these enclosures. Modern electronic items have many different sources of EMI. These sources are often placed inside a rectangular shaped metal box to limit the EM emissions from the equipment. Care is taken to ensure the shielding is as comprehensive as possible thus apertures are kept to a minimum and covered in metallic blanking plates. Such a shielded, rectangular enclosure has a good chance of forming a resonant cavity so that field strengths generated by the circuit may well be enhanced once the circuit is mounted within the casing. Normally the circuit may have a number of sources within the enclosure, all of which add to the EM fields within; changing the positions of the various sources will change the amount of resonance and constructive interference, [1]. There are also likely to be a number of susceptors at multiple locations throughout the circuit.

There is obviously an optimal size and shape of enclosure and component layout however, exhaustively placing components inside enclosures and then computing the resultant fields is a task that that would require a massive undertaking on behalf of the designer. A far better approach to component placement is to use some kind of optimisation method to place the components to achieve a desired radiation level. This paper describes the novel use of a genetic algorithm (GA) and a finite-difference time-domain (FDTD) solver to optimise source and susceptor placement inside a perfectly conducting structure, building upon initial work completed in [2].

Genetic algorithms are briefly introduced in section 2 and then the Finite-Difference Time-Domain method is introduced in section 3. Section 4 describes the setup of the computer simulation and section 5 discusses the results of these simulations. Finally, section 6 presents conclusions from the work.

2 Genetic Algorithms

GAs are a stochastic search mechanism with their operation firmly rooted in natural selection and survival of the fittest, [3] and [4]. GAs have been shown to provide robust search and optimisation in complex spaces, [3] and [5]. They use simple operations on a population of individuals, which lead to an emergent evolution of an individual or individuals. Each individual in the population represents a potential solution to the given problem scenario and as such is evaluated. After an individual has been evaluated a figure of merit (FoM) is attributed to the individual. This FoM is a measure of how well the

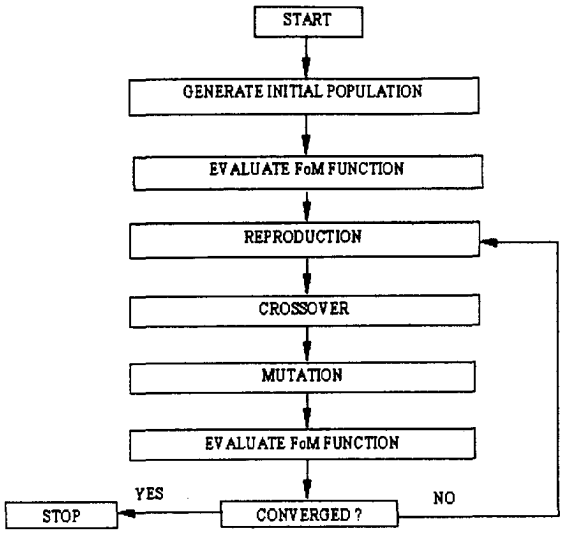

Figure 1: *GA Process Flowchart.*

individual solves the problem. GAs can lead to the optimal solution to a problem, more often however, they are used to optimise a problem towards an improved solution facilitating a trade-off between excessive computational time and meaningful results. The GA process can be summarised graphically as shown in figure 1.

The GA methodology used in this work is the micro genetic algorithm (μGA). The μGA technique has been shown to reach the optimal area of multi-modal solution spaces earlier than conventional GA methods, with minimal computing time, [6]. It has already been demonstrated that the μGA can be successfully linked with an FDTD solver, [7], for optimisation in EM problems. Initially in a GA a fixed size population is created and populated with randomly generated individuals of a fixed length, this length is determined by the encoding of the problem parameters. The population size for the μGA is generally kept small *e.g.* five. This is different from the classic GA where the population size is typically much larger, in the order of 100s. These individuals are all possible solutions to the same given problem. They are assessed and each one given a score, the FoM, which is then used to determine the likelihood of reproduction into the next generation. The FoM is analogous to fitness in the natural world where fitter individuals survive longer and hence have a better chance of continuing their genetic lineage. The particularly successful, higher scoring individuals may be reproduced more than once into the next generation. In the μGA used here tournament selection is employed. This is perhaps the most effective for many application types as it has been shown to provide better convergence towards a solution in the initial stages of optimisation, [8]. Tournament selection works by randomly choosing N members of the population, and in this instance, as in many others, $N = 2$. These individuals are then pitched against each other to determine which has the better FoM, the winner of the tournament being selected to be a member of the new population; this is repeated until the new population is filled. In conjunction with tournament selection elitist reproduction is also employed. This guarantees that the best individual from a population is present in the next population, hence preserving the best current solution to the given problem and maintaining a good genetic stock. After reproduction the individuals undergo crossover. Here two randomly picked individuals are mated together, swapping information between their chromosomes. In a classic GA mutation is also applied, however in the μGA mutation is turned off. Mutation serves to alter the genetic makeup of these new offspring with a small fixed probability. Once again mimicking nature, mutation can lead to either a detrimental or beneficial effect on performance. Mutation allows, in a classic GA, random search to take place and hopefully leads to the avoidance of local optima. Once the population has converged to a determined optimal value, further GA operating is no longer needed and the GA can be halted. Due to the small population size used in the μGA premature convergence is often seen to be happening. To prevent this a restart mechanism is used. This restart mechanism involves checking for convergence in the current generation of individuals and then restarting the next generation with only the elite individual and new randomly created individuals. The use of a restart operator ensures random search takes place and leads μGA away from local optima. Convergence is checked for in this application by measuring the changes in the chromosomes, the individuals, between generations. Once there are few changes between generations then the population can be considered to be converged; the setting of this limit is a parameter that the user has control over. An important component of any GA code is the device by which random numbers are generated, or to be more correct pseudo-random numbers. This is usually a portable pseudo-random number generator (PRNG) that produces the same sequence of *random* numbers for a given seed value. The *quality* of the PRNG is an important factor. The area of PRNG research is vast and not going to be, for brevity, discussed here. Common references on the subject are [9], [10], [11] and [12].

A clear difference can be seen here between optimisation based on calculus methods and GA based optimisation. GAs make use of interim performance in the optimisation problem; calculus based methods are only concerned with optimisation toward an overall optimal point and do not "remember" any interim performances.

3 The FDTD Method

The FDTD method, [13], [14], has become one of the most popular methods for solving Maxwell's equations. It is a volumetric domain decomposition technique that is second order accurate in space and time, easily implemented in software and accurately models the physical world. It is a widely used method for EMC/EMI work, [15], as well as radar, bioengineering and antenna analysis. The FDTD method is described widely in the literature, [16], and so only a very brief description is given here.

Maxwell's equations, in differential form, equations (1) -

(2), are simply modified to central-difference equations, discretised, and implemented in software. The equations are solved in a leap-frog manner, [14], *i.e.* the electric field is solved at a given instant in time, then the magnetic field is solved at the next instant in time, and the process is repeated over and over again. In equations (1) and (2) $\boldsymbol{H}$ and $\boldsymbol{E}$ have their usual meanings.

$$\frac{\partial \boldsymbol{H}}{\partial t} = -\left(\frac{1}{\mu}\nabla \times \boldsymbol{E} + \frac{\rho'}{\mu}\boldsymbol{H}\right), \tag{1}$$

$$\frac{\partial \boldsymbol{E}}{\partial t} = \frac{1}{\epsilon}\nabla \times \boldsymbol{H} - \frac{\sigma}{\epsilon}\boldsymbol{E}. \tag{2}$$

Using a three dimensional Cartesian co-ordinate system we can now write out the vector components of the curl operator. Given below is only one of these components, namely the x component of the $\boldsymbol{H}$ field,

$$\frac{\partial H_x}{\partial t} = \frac{1}{\mu}\left(\frac{\partial E_y}{\partial z} - \frac{\partial E_z}{\partial y} - \rho' H_x\right), \tag{3}$$

where μ is magnetic permeability and ρ' is a magnetic loss parameter. It is the complete set of coupled partial differential equations, six in total, that are the fundamental basis of the numerical FDTD algorithm. The discretised form of equation (3) is shown below:

$$\begin{aligned} m &= MEDIA_{H_x|_{i,j,k}}, \\ H_x|_{i,j,k}^{n+\frac{1}{2}} &= D_a(m)\, H_x|_{i,j,k}^{n-\frac{1}{2}} \\ &+ D_b(m)\begin{pmatrix} E_y|_{i,j,k+\frac{1}{2}}^{n} - E_y|_{i,j,k-\frac{1}{2}}^{n} \\ +E_z|_{i,j-\frac{1}{2},k}^{n} - E_z|_{i,j+\frac{1}{2},k}^{n} \end{pmatrix}, \end{aligned} \tag{4}$$

where n is the time step under consideration and i, j, k are the three orthogonal spatial co-ordinates. The integer array MEDIA defines material conditions for each field vector component. This allows the medium at each point to be mapped out. The arrays D_a, D_b are magnetic field update coefficients, there are corresponding electric field update coefficients also. A full explanation of all of these equations is presented in [13].

4 Simulation Setup

The initial results are obtained from using the GA to place a source and susceptor point relative to each other on the surface of a dielectric slab (DS) to achieve the lowest electromagnetic coupling between the two. The complete simulation is implemented in Fortran 77 compiled on a SUN ENTERPRISE server with 512MB of RAM utilising 4 of 8 processors.

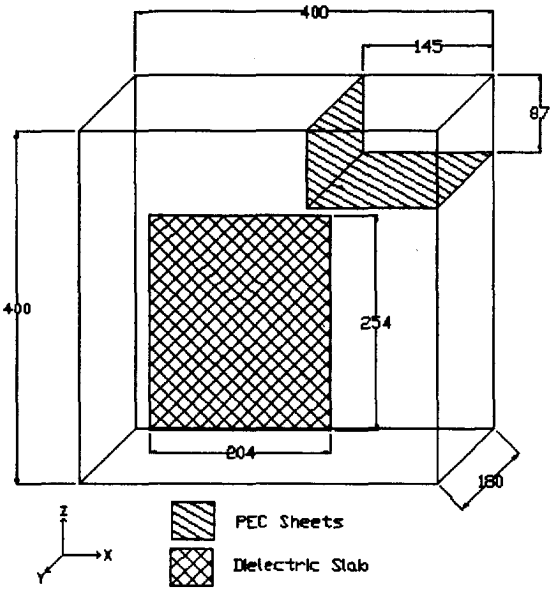

Figure 2: *Enclosure geometry showing the representations of the internal structure and dielectric slab, all sizes are in millimetres, mm.*

4.1 Physical Problem Description

The problem geometry is that of a simplified metal box, which has perfectly electrically conducting (PEC) walls, an internal structure and DS representation. The internal structure is modelled as two PEC sheets in the top corner of the geometry. The DS can be thought of as a representation of the substrate of a printed circuit board (PCB). The problem geometry is shown in figure 2. The DS has a relative permittivity, ϵ_r, of 4 and possesses unity magnetic permeability μ_r.

4.2 μGA and FDTD Setup

The μGA used is based on the implementation by Carroll, [17], modified to accommodate the given task of moving the source point and susceptor point on the DS. The two points are specified in a three dimensional Cartesian system with the y ordinate being held constant as this represents the surface of the DS. Binary encoding is used in the μGA and this leads to a chromosome string length of 24 bits, 4 bits per x, y and z co-ordinate of the source and susceptor. It should be noted that it would be possible to omit the y ordinate from the chromosome; however, the memory saving would be insignificant especially when compared to the coding effort required to convert the GA for this one specific case. Care must be taken to avoid the y ordinate being altered during reproduction and crossover, this is achieved using a uniform crossover operator. Uniform crossover, [18], has also been found to give faster convergence than single point crossover in a μGA, [6], [19]. The population size is maintained at five. These co-ordinate values are passed to the FDTD solver which computes the resulting field distribution inside the enclosure. The peak electric field at the susceptor point is returned as the FoM to the μGA, no fitness scaling is

used as tournament selection is the method of selection employed in this GA implementation, [18]. The μGA attempts to minimise this FoM, *i.e.* minimise the peak electric field at the susceptor point.

The FDTD solver is based on the equations given in [13]. The DS is one cell thick and has one cell of free space between itself and the enclosure wall. The PEC sheets are modelled as infinitely thin. A soft E_z directed sinusoidal, continuous wave, ideal Hertzian dipole of $2.05GHz$ frequency and amplitude of $10Vm^{-1}$ is used as the source in the FDTD simulation. The domain is discretised into dimensions of $7.2727mm$ in the x and z directions and $7.2mm$ in the y direction. Based on these dimensions and the material within the computational domain the time step size for the solver is set at the Courant limit, in this instance approximately $14ps$.

Initially two optimisation cases are run; a non-lossy and then a lossy dielectric slab, in the lossy case the conductivity is set to $0.04Sm^{-1}$. After this a multi-objective simulation is run where two objectives are to be optimised, these being the reduction in coupling between source and susceptor points at two specific frequencies.

5 Results

5.1 Single Objective Optimisation

The progress of the optimisation process can be seen in figure 3 where the results of both the non-lossy and lossy simulations are presented. This figure shows the evolution of the best individual in the simulation, the elite individual. While this individual remains the best the FoM remains at the same value, when a superior one is bred, a step change occurs indicating the presence of a new elite value.

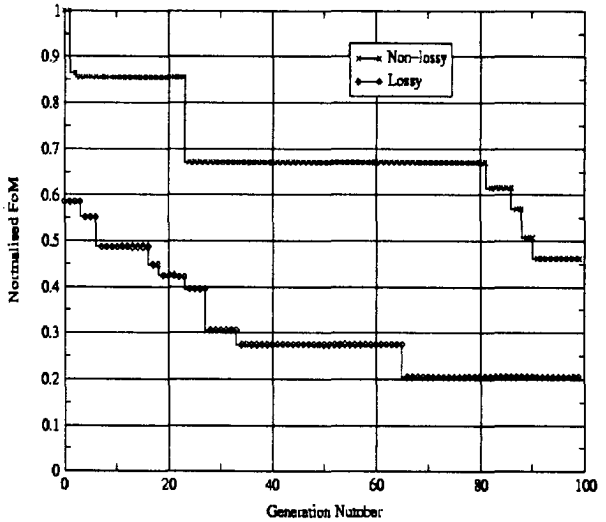

Figure 3: *Generation optimisation of both the non-lossy and lossy cases.*

The final value for the non-lossy case is $0.0541Vm^{-1}$ from an initial value of $0.1172Vm^{-1}$, and the final value for the lossy case is $0.0240Vm^{-1}$ from a value of $0.0685Vm^{-1}$. Both of the curves are normalised to the value of $0.1172Vm^{-1}$ for ease of comparison. As expected the values of field strength for the lossy case are lower than those for the non-lossy case as in the lossy case energy is dissipated in the dielectric slab. Figure 3 also shows us that the lossy case reaches its best FoM at generation 66, earlier than the non-lossy case which reaches its best FoM at generation 91. This is a random dynamic of the GA and attributable to the solution surface topology and the choice of PRNG used with the μGA. The number of generations was limited to 100 as experience with this code has shown that there is a minimal return on computing time by exceeding this point. Testimony to this is given by the fact that running the code to 200 generations gives only a final value of $0.0507Vm^{-1}$ for the non-lossy case and $0.0204Vm^{-1}$ for the lossy case, a marginal increase in performance for a doubling of computation time. This embraces one philosophy of using a GA, namely to produce an acceptable improvement toward an optimal point for a limited amount of effort.

The final field distribution on the surface of the DS can be seen in figure 4 for the non-lossy case and in figure 5 for the lossy case. These plots are generated by applying a peak hold to the E_z component at each location on the surface of the DS throughout the simulation.

The final positions of the source and susceptor points on the DS are indicated; for the non-lossy case these are at (2,16) and (3,35) respectively, and for the lossy case the co-ordinates are (2,35) and (23,11). These co-ordinate values given are of course on the x and z axes as the y ordinate is constant. These false colour plots clearly show that the μGA has indeed found good solutions but not the best solutions. The global minimum point in figure 4 is at (2,2) with a value that is $2.1dB$ down on the position found by the μGA. In figure 5 the global minimum is at (12,14) with a value that is $1.4dB$ down the μGA position. The final values found by the μGA are $57.6dB$ and $64.6dB$ down on the global maximum for the non-lossy and lossy cases respectively. It should be noted that the patterns presented in these figures are ones of over 1 million possible patterns due to source and susceptor placement. Finding the global minimum on each of them would require direct evaluation of each pattern. The μGA vastly cuts down on the number of evaluations required to arrive at an acceptable result.

5.2 Multi-objective Simulations

Multi-objective optimisation(MO) is often sought in practice as often compliance in one particular objective upsets the compliance of another objective. MO aims to achieve a solution that can not be improved upon, simultaneously, in each of the objectives. This is called a Pareto optimal solution, and the set of all these solutions is called the Pareto optimal set, [20]. For the MO simulations some changes had to be made to the GA-FDTD code. As two objectives were being optimised a method of measuring

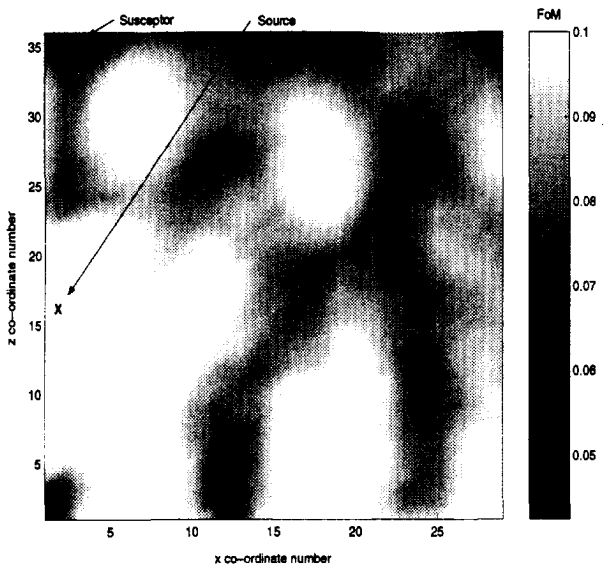

Figure 4: *False colour plot of final field distribution on surface of dielectric slab after non-lossy simulation. The x and z axes are marked in FDTD cells. Source and susceptor positions are indicated on the figure.*

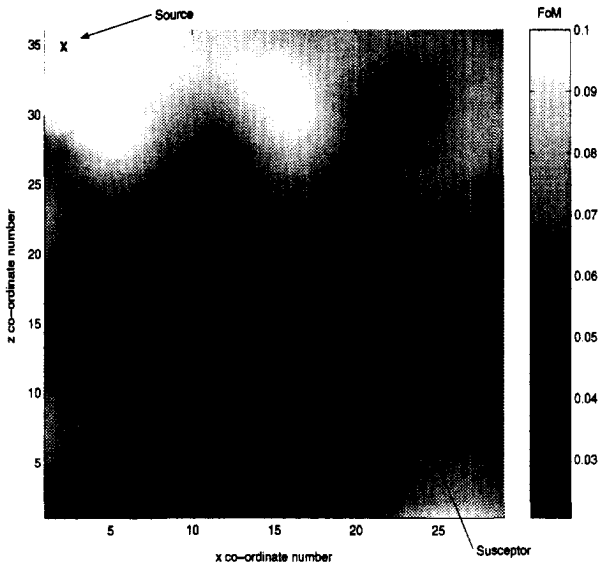

Figure 5: *False colour plot of final field distribution on surface of dielectric slab after lossy simulation. The x and z axes are marked in FDTD cells. Source and susceptor positions are indicated on the figure.*

their fitness at one and the same time is required. To accomplish this the method of objective weighting is used, [20]. This method is explained mathematically by equation (5),

$$Z = \sum_{i=1}^{N} w_i f_i(\boldsymbol{x}) \quad \text{where} \quad \boldsymbol{x} \in \boldsymbol{X}. \tag{5}$$

In equation (5) Z is a scalar valued variable that is a weighted sum of the individual objectives, where there are N objectives in total. The function f is the function that returns the FoM, in this case the FDTD solver, and $\boldsymbol{x}$ represents the parameters of the function, co-ordinate values in this case. The feasible region of solutions is denoted by $\boldsymbol{X}$. The sum of the individual weights adds to 1 and each weight lies in the range 0 to 1 *i.e.* $0 \leq w_i \leq 1$. It is the scalar value Z that is optimised by the GA. The method of objective weighting is an easily implementable scheme that produces a solution from the Pareto optimal set.

The problem setup for the MO optimisation involves the same geometry as previously with the only change being the source. A Gaussian pulse modulated onto a sine wave is now used as the source. This gives a symmetrical spectrum about the carrier frequency, no DC component, and a bandwidth controlled by the length of the pulse. Its mathematical form given in [13] is described by equation (6),

$$E_z = E_0 e^{-\left[\frac{n-n_0}{n_{decay}}\right]^2} sin(2\pi f_0(n-n_0)\Delta t). \tag{6}$$

The Gaussian pulse is centred around frequency f_0 at step n_0 with a $1/e$ characteristic decay of n_{decay} steps, and Δt is the step size. The time series and frequency response of the source is shown in figure 6. The centre frequency for the source is chosen at $1.500GHz$ and the objectives for optimisation were chosen as the minimisation of the $1.002GHz$ and $2.004GHz$ components in the frequency response which is computed on the fly as the FDTD simulation progresses as detailed in [13]. These frequencies were chosen as they tie in with equipment used in a related measurement study. Only non-lossy simulations were run in this setup.

The resulting frequency response from the E_z component at the susceptor point the simulations can be seen in figure 7. The dashed line in figure 7 shows the initial DFT before the optimisation process begins; the solid line in the figure displays the final DFT after completion of the optimisation process. A clear difference in the two curves at the respective objective frequencies can be seen. Also, it can be clearly seen that the field values at the objective frequencies, on the final DFT, are considerably lower than at other frequencies, within the same response, excepting of course at the tails of the response where there is minimal energy from the source. The values of the objectives on the final response are $54dB$ down for the $1.002GHz$ objective on the max value in the response and the value at $2.004GHz$ is $44dB$ down. Relative to the initial DFT the final response in down $27dB$ at the $1.002GHz$ objective and down $35dB$ at the $2.004GHz$ objective.

6 Conclusions

A method of using a μGA in conjunction with a FDTD solver to facilitate electromagnetic optimisation has been shown. The conjoining of the two codes allows a difficult design problem to be tackled, namely that of ra-

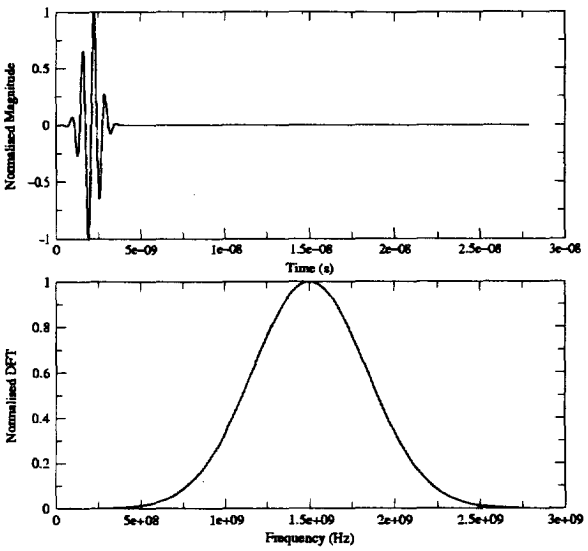

Figure 6: *Time series of the pulsed source, upper graph, and its DFT, lower graph. This is the source characteristic used in the multi-objective optimisation simulations.*

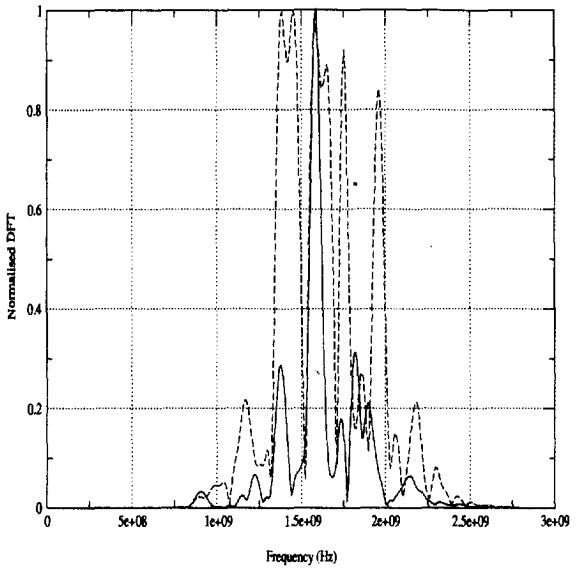

Figure 7: *DFTs of E_z at the susceptor point of the multi-objective simulation with objective of minimising the $1.002GHz$ and $2.004GHz$ frequency components of the response. Shown are the initial DFT before optimisation begins (dashed line) and the final DFT after optimisation (solid line).*

diating and susceptible component placement within an arbitrary metallic structure to minimise coupling. The μGA technique is used as this gives a significant reduction in computation time with little loss in performance of the final optimised result. Ensuring that the μGA finds the global optimum in difficult optimisation problems is an area that needs further attention, but the ability of the technique to reach a near optimal solution has been demonstrated. Both single and multiple objectives for optimisation have been presented with promising results from each. It is worth noting that if an exhaustive search were to be completed on the problems presented then over one million simulations would be required taking over one year to complete; the GA based search, however, took approximately four hours.

The design optimisation cases presented are rather simplistic but do prove the concept of the hybrid code. More challenging problem geometries can easily be accommodated in the FDTD code with little burden to computing time as once the domain has been discretised it is the number of resulting cells that chiefly determines the computation time. It is envisaged that this tool can be used to provide design rules for component placement within an enclosed resonant cavity and that it can can also be used to assess specific designs.

References

[1] J. Mix, G. Haussmann, M. Piket-May, and K. Thomas, "EMC/EMI design and analysis using FDTD," in *IEEE Int. EMC Symp.*, vol. 1, (Denver, CO), pp. 177–181, 1998.

[2] R. I. Macpherson and N. J. Ryan, "The use of a genetic algorithm and the FDTD method for limiting resonance in shielded enclosures," in *Proceedings of EMC Europe 2000, Brugge, 4^{th} European Symposium on Electromagnetic Compatibility*, vol. 2, pp. 203–208, September 2000.

[3] D. Goldberg, *Genetic Algorithms in Search, Optimization and Machine Learning.* Reading, MA: Addison-Wesley, 1989.

[4] R. L. Haupt and S. E. Haupt, *Practical Genetic Algorithms.* John Wiley & Sons, 1998.

[5] J. Holland, *Adaption in Natural and Artificial Systems.* The University of Michigan Press, 1975.

[6] K. Krishnakumar, "Micro-genetic algorithms for stationary and non-stationary function optimization," *SPIE: Intelligent Control and Adaptive Systems*, vol. 1196, pp. 289–296, 1989.

[7] J. Jiang and G. P. Nordin, "A rigorous unidirectional method for designing finite aperture diffractive optical elements," *Optics Express*, vol. 7, no. 6, pp. 237–242, 2000.

[8] G. J. E. Rawlins, ed., *Foundations of Genetic Algorithms.* Morgan Kaufmann, 1991.

[9] D. E. Knuth, *The Art of Computer Programming*, vol. 2, Semi-numerical Algorithms. Reading, Massachusetts: Addison-Wesley, 2 ed., 1981.

[10] P. Hallekalek, "Good random number generators are (not so) easy to find," *Mathematics and Computers in Simulation*, vol. 46, pp. 485–505, 1998.

[11] P. L'Ecuyer, "Uniform random number generation," *Ann. Oper. Res.*, vol. 53, pp. 77–120, 1994.

[12] P. L'Ecuyer, *Random Number Generation.* New York: In Handbook of Simulation, Jerry Banks (ed.) Wiley, 1997.

[13] A. Taflove, *Computational Electrodynamics: The Finite-Difference Time-Domain Method.* Boston, MA: Artech House, 1995.

[14] K. S. Yee, "Numerical solution of initial boundary value problems involving Maxwell's equations in isotropic media," *IEEE Transactions on Antennas and Propagation*, vol. 14, pp. 302–307, Mar. 1966.

[15] B. Archambeault, O. M. Ramahi, and C. Brench, *EMI/EMC Computational Modeling Handbook.* Kluwer Academic Publishers, 1998.

[16] J. B. Schneider and K. Shlager, "Finite-Difference Time-Domain literature database." WWW. Available at `http://www.fdtd.org` Last Accessed 20^{th} April 2002.

[17] D. L. Carroll, "Fortran Genetic Algorithm driver." WWW. Available at `http://cuaerospace.com/carroll/ga.html` Last Accessed 20^{th} April 2002.

[18] M. Mitchell, *An Introduction to Genetic Algorithms.* MIT Press, 5 ed., 1999.

[19] D. L. Carroll, *Genetic Algorithms and Optimizing Chemical Oxygen-Iodine Lasers*, vol. XVIII of *Developments in Theoretical and Applied Mechanics*, pp. 411–424, H. Wilson, R. Batra, C. Bert, A. Davis, R. Schaper, D. Stewart, and F. Swinson eds. Guntersville, AL: The University of Alabama, 1996.

[20] N. Srinivas and K. Deb, "Multiobjective optimization using nondominated sorting in genetic algorithms," *Evolutionary Computation*, vol. 2, no. 3, pp. 221–248, 1994.

Russell Macpherson graduated with a MEng (Hons) degree in electrical and electronic engineering degree from the University of Aberdeen, Scotland, U.K. in 1999. Currently he is pursuing his PhD studies at the same institution. His research interests include genetic algorithms, artificial neural networks and fuzzy logic and how these methods can be applied to electromagnetic optimisation problems.

Nick Ryan received the BEng degree in electrical and electronic engineering from the University of Bristol, U.K. in 1990 and the PhD degree from the department of electronic and electrical engineering, University of Sheffield, U.K. in 1998. He joined the department of engineering in the University of Aberdeen, U.K. in 1997 where he currently lectures safety and reliability in electronic systems. His research interests include computational electrodynamics, electromagnetic compatibility, and renewable energy systems.

COUPLING 2D FINITE ELEMENT MODELS AND CIRCUIT EQUATIONS USING A BOTTOM-UP METHODOLOGY

E. Gómez[1], J. Roger-Folch[2], A. Gabaldón[1] and A. Molina[1]

[1]Dpto. de Ingeniería Eléctrica. Universidad Politécnica de Cartagena. Campus Muralla del Mar, 30202. Cartagena, Spain
E-mail: emilio.gomez@upct.es, antonio.gabaldon@upct.es, angel.molina@upct.es

[2]Dpto. de Ingeniería Eléctrica. ETSII. Universidad Politécnica de Valencia. PO Box 22012, 46071. Valencia, Spain.
E-mail: jroger@die.upv.es

ABSTRACT. The aim of this paper is to present an approach, able to deal with all possible connections of voltage and current sources and impedances, combining conductors in which the skin effect is taken into account and conductors in which skin effect is neglected. This approach is obtained using a bottom-up methodology. In this way, the meaning of terms in the generalized approach is naturally inherited from some specific problems. This model is presented in a compact form, preserving sparse, symmetric and positive-definiteness matrices. The vectors and matrices, computed during the solution stage, are employed in engineering calculations as current and inductance computations providing compact expressions suitable for efficient algorithms. Finally, the proposed approach, implemented in a FEM software package developed by the authors, is applied to the study of a three-phase transformer, supplied with a balanced three-phase voltage (sinusoidal and nonsinusoidal) and loaded with an unbalanced three-phase RL impedance. The agreement between the computed and experimental results shows the validity of the proposed model and its implementation.

1 INTRODUCTION

The natural excitation for the Finite Element Method (FEM) in electromagnetism is current (current density). This current is supplied by an external electric circuit; and, usually, the value of this current is unknown, as the circuits consist of passive elements and voltage sources. Therefore, FEM and electrical equations are coupled by these unknown currents. There are two different approaches to couple these equations. In the first approach, called direct coupling, the equations obtained from FEM and the electrical circuits are integrated in a single system of equations having the magnetic vector potential as its solution. In the second one, called indirect coupling, two different systems of equations are obtained; one of them takes into account the FEM equations, and the other one, the circuit equations. In this paper, a method, based on the direct coupling of FEM and circuit equations is presented.

Many approaches on coupled 2D Finite Element models and circuit equations have been proposed [1]-[7]. Most of them, take into account the skin effect for all the conductors or, they neglect its influence, without evaluating its magnitude over each conductor. In this paper, a bottom-up methodology is applied, generalizing the meaning of the studied examples, instead of a theoretically obtained approach. So, some common winding connections were studied—one-phase circuit and three-phase circuits with star and delta connections—, being presented here the three-phase star connection handling unbalanced load and voltage conditions. In this paper, the model is applied to the study of a power transformer, although it has been applied to other non-static machines as induction motors, [10].

2 BASIC EQUATIONS

Assuming that the displacement currents are neglected, Maxwell's equations using a magnetic vector potential formulation can be written in 2D as:

$$\frac{\partial}{\partial x}\left(\nu(\mathbf{B})\frac{\partial A(x,y)}{\partial x}\right)+\frac{\partial}{\partial y}\left(\nu(\mathbf{B})\frac{\partial A(x,y)}{\partial y}\right)=-J(x,y) \quad (1)$$

Where $A(x,y)$ is the magnetic vector potential, $J(x,y)$ the current density (z component) and ν the reluctivity that depends on the magnetic flux density vector ($\boldsymbol{B}$). In anisotropic materials, reluctivity depends on $|\boldsymbol{B}|$ and the angle (θ) between $\boldsymbol{B}$ and the rolling direction of the material $\nu=\nu(A,\theta)$.

The expression of current density depends on how the conductors are defined. So, the conductors can be modelled as solid conductors, in which case the skin effect is taken into account, or stranded conductors, in which case the skin effect is neglected. Stranded conductors are particularly useful to model windings in which an individual mesh considering their relations would exceed in many cases the requirements of actual computers without providing a significantly greater accuracy. If all the conductors in the problem are solid conductors, the following equation is employed, [8] [9]:

$$\nabla\times\nu\nabla\times\mathbf{A}=\sigma\mathbf{E}_{ext}-\sigma\frac{\partial\mathbf{A}}{\partial t}-\sigma v_e\times\nabla\times\mathbf{A} \quad (2)$$

The first term on the right side in (2), $\boldsymbol{E}_{ext}$ being the external electric field and σ the electrical conductivity, represents the current density due to the voltage source. The second term takes into account the current density due to the temporal

variation of A. The third one represents the current density due to the movement, being v_e the velocity of the conductor with respect to **B**. By using a frame of reference, such that the relative velocity becomes zero, (2) can be written as, [8]:

$$\nabla \times \nu \nabla \times \mathbf{A} = \sigma \mathbf{E}_{ext} - \sigma \frac{d\mathbf{A}}{dt} \tag{3}$$

The total current of a conductor can be obtained by integrating the right side of (3):

$$I_c = \iint_{S_c} \left(\sigma \mathbf{E}_{ext} - \sigma \frac{d\mathbf{A}}{dt} \right) \mathrm{dS} \tag{4}$$

In 2D problems (3) becomes:

$$-\nabla(\nu \nabla A) = \sigma \frac{u_s}{l} - \sigma \frac{dA}{dt} \tag{5}$$

Where u_s is the voltage between the terminals of the conductor and l the length of the conductor (thickness of the considered domain along the z-axis). Equation (5) takes into account the skin effect.

When the conductors are considered stranded, it is supposed that the current (i_f) is the same in all the conductors connected in series (winding); then, their current density can be obtained by J=Ni$_f$/S. Where S is the entire section of all the conductors (N turns) integrating the winding, σ the electrical conductivity and R_F the DC resistance. The current can be calculated in 2D problems, by considering the voltage u_F between the terminals of the winding as the sum of the voltages of its conductors:

$$i_f = \frac{u_F}{R_F} - \frac{l N}{R_F S} \iint_S \frac{dA}{dt} dS \tag{6}$$

Using (1) and (6):

$$-\nabla(\nu \nabla A) = \frac{N u_F}{S R_F} - \frac{\sigma N}{S} \iint_S \frac{dA}{dt} dS \tag{7}$$

Summarizing (3) and (7) into a single equation for 2D problems:

$$-\nabla(\nu \nabla A) = \begin{cases} \dfrac{N u_F}{S R_f} - \dfrac{\sigma N}{S} \iint_S \dfrac{dA}{dt} dS & \textit{Stranded} \\ \sigma \dfrac{u_s}{l} - \sigma \dfrac{dA}{dt} & \textit{Solid} \end{cases} \tag{8}$$

3 EXAMPLE. THE WINDINGS ARE STAR CONNECTED

The authors have solved some complex winding connections. In this case, three windings of stranded conductors are star connected (figure 1). They are modelled with FEM, and indeed can or can not share the same 2D magnetic circuit. The total DC resistances, including the resistances corresponding to the windings and the load, are called R_R, R_S, R_T. In the same way L_R, L_S, L_T take into account the inductance corresponding to the load and the part of leakage flux not considered in the two-dimensional model.

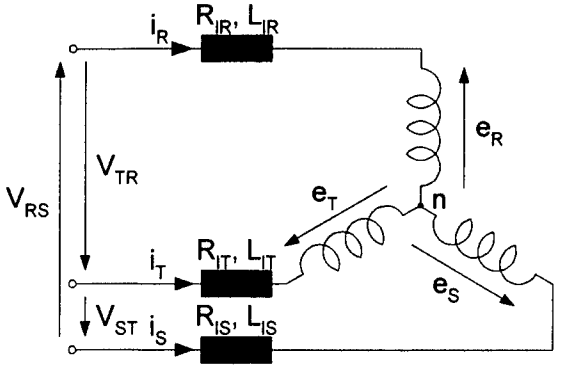

Figure 1. The windings are star connected.

From figure1 the following equations can be obtained:

$$V_{RS} = e_R - e_S + \left(R_R i_R + L_R \frac{di_R}{dt} \right) - \left(R_S i_S + L_S \frac{di_S}{dt} \right) \tag{9}$$

$$V_{ST} = e_S - e_T + \left(R_S i_S + L_S \frac{di_S}{dt} \right) - \left(R_T i_T + L_T \frac{di_T}{dt} \right) \tag{10}$$

$$V_{TR} = e_T - e_R + \left(R_T i_T + L_T \frac{di_T}{dt} \right) - \left(R_R i_R + L_R \frac{di_R}{dt} \right) \tag{11}$$

$$i_R + i_S + i_T = 0 \tag{12}$$

values of e_R, e_S and e_T can be obtained using:

$$e_j = -l \; N_j \left(\frac{dA_{m,j}}{dt} \right) \qquad j = R,S,T \tag{13}$$

where A_m is the mean magnetic vector potential on j winding, defined by:

$$A_{m,j}(t) = \frac{\iint_{S_j} \{\varphi(x,y)\}^T \{A(t)\} dS}{\iint_{S_j} dS} = \frac{\iint_{\Omega} \beta_j(x,y) \{\varphi(x,y)\}^T d\Omega}{\iint_{S_j} dS} \{A(t)\} = \{w\}^T \{A(t)\} \tag{14}$$

Being $\{w\}^T$ the phase vector, which provides information about the topology of each winding, $\varphi(x,y)$ the shape or interpolation functions, whose formulas are well-known for classical elements, and Ω the entire domain where the integral is extended by using the phase functions β_j:

$$\beta_j(x,y)=\begin{cases}1 & If\ \ (x,y)\in S_j^+\\ -1 & If\ \ (x,y)\in S_j^-\\ 0 & Otherwise\end{cases} \tag{15}$$

Using the Crank-Nicholson time stepping method, the following equations are obtained:

$$\frac{1}{2}\left(\frac{di}{dt}\right)^{t+\Delta t}+\left(1-\frac{1}{2}\right)\left(\frac{di}{dt}\right)^{t}=\frac{i^{t+\Delta t}-i^{t}}{\Delta t} \tag{16}$$

$$\frac{1}{2}\left(\frac{dA_m}{dt}\right)^{t+\Delta t}+\left(1-\frac{1}{2}\right)\left(\frac{dA_m}{dt}\right)^{t}=\frac{A_m^{t+\Delta t}-A_m^{t}}{\Delta t} \tag{17}$$

Using (9), (10), (11), (12), (13), (16) and (17):

$$\begin{Bmatrix} i_R^{t+\Delta t}\\ i_S^{t+\Delta t}\\ i_T^{t+\Delta t}\end{Bmatrix}=\frac{\Delta t}{M_E^2}\begin{bmatrix} M_T & 0 & -M_S\\ -M_T & M_R & 0\\ 0 & -M_R & M_S\end{bmatrix}\begin{Bmatrix} V_{RS}^{t+\Delta t}+V_{RS}^{t}\\ V_{ST}^{t+\Delta t}+V_{ST}^{t}\\ V_{TR}^{t+\Delta t}+V_{TR}^{t}\end{Bmatrix}-\frac{2l}{M_E^2}$$
$$\begin{bmatrix} M_S+M_T & -M_T & -M_S\\ M_T & M_T+M_R & M_R\\ M_S & M_R & M_S+M_R\end{bmatrix}\begin{bmatrix} N_R & 0 & 0\\ 0 & N_S & 0\\ 0 & 0 & N_T\end{bmatrix}\begin{Bmatrix} A_{m,R}^{t+\Delta t}-A_{m,R}^{t}\\ A_{m,S}^{t+\Delta t}-A_{m,S}^{t}\\ A_{m,T}^{t+\Delta t}-A_{m,T}^{t}\end{Bmatrix}$$
$$-\frac{l}{M_E^2}\begin{bmatrix} M'_R(M_S+M_T) & M'_SM_T & -M'_TM_S\\ M'_RM_T & M'_S(M_T+M_R) & M'_TM_R\\ M'_RM_S & M'_SM_R & M'_T(M_S+M_R)\end{bmatrix}\begin{Bmatrix} i_R^{t}\\ i_S^{t}\\ i_T^{t}\end{Bmatrix} \tag{18}$$

where:

$$\begin{aligned} M_j &= R_j\Delta t+2L_j \qquad j=R,S,T\\ M'_j &= R_j\Delta t-2L_j \qquad j=R,S,T\\ M_E^2 &= M_RM_S+M_SM_T+M_TM_R\end{aligned} \tag{19}$$

Equation (18) can be written in a packed form as:

$$\begin{aligned}\left\{i^{t+\Delta t}\right\} &= \Delta t\left[G_a\right]\left\{u_{ext}^{(t+\Delta t)+t}\right\}\\ -l\ \ &\left[G_b\right]\left[N\right]\left(\left\{A_m^{t+\Delta t}\right\}-\left\{A_m^{t}\right\}\right)-\left[G_a\right]\left[G_c\right]\left\{i^{t}\right\}\end{aligned} \tag{20}$$

The current density can be obtained using:

$$\left\{J^{t+\Delta t}\right\}=\begin{Bmatrix} J_R^{t+\Delta t}\\ J_S^{t+\Delta t}\\ J_T^{t+\Delta t}\end{Bmatrix}=\begin{bmatrix} \frac{N_R}{S_R} & 0 & 0\\ 0 & \frac{N_S}{S_S} & 0\\ 0 & 0 & \frac{N_T}{S_T}\end{bmatrix}\begin{Bmatrix} i_R^{t+\Delta t}\\ i_S^{t+\Delta t}\\ i_T^{t+\Delta t}\end{Bmatrix} \tag{21}$$

Using (20), (21) and the definition of A_m in (14) the following equation is obtained:

$$\begin{aligned}\left\{J^{t+\Delta t}\right\} &= \Delta t\left[W\right]\left[N\right]\left[G_a\right]\left\{u_{ext}^{(t+\Delta t)+t}\right\}\\ -l\left[W\right]\left[N\right]\left[G_b\right]\left[N\right]\left[W\right]^T&\left(\left\{A^{t+\Delta t}\right\}-\left\{A^{t}\right\}\right)\\ -\left[W\right]\left[N\right]\left[G_a\right]\left[G_c\right]&\left\{i^{t}\right\}\end{aligned} \tag{22}$$

Where the term $[W]$ is called the phase matrix defined as the matrix containing the phase vectors presented in the problem (three in this case).

Using (1) and (22):

$$\begin{aligned}\left(\left[S^{t+\Delta t}\right]+l\left[W\right]\left[N\right]\left[G_b\right]\left[N\right]\left[W\right]^T\right)&\left\{A^{t+\Delta t}\right\}=\\ \Delta t\left[W\right]\left[N\right]\left[G_a\right]&\left\{u_{ext}^{(t+\Delta t)+t}\right\}+l\left[W\right]\left[N\right]\left[G_b\right]\left[N\right]\left[W\right]^T\left\{A^{t}\right\}\\ -\left[W\right]\left[N\right]\left[G_a\right]&\left[G_c\right]\left\{i^{t}\right\}\end{aligned} \tag{23}$$

where $[S^{t+\Delta t}]$ is the stiffness matrix. Therefore, equation (23) models 2D magnetic circuits with a three star connected windings of stranded conductors, the magnetic vector potential in the nodes at $t+\Delta t$ being the unknown values. Besides, current in the windings at t must be computed using efficient algorithms.

4 THE GENERALIZED SYSTEM OF EQUATIONS

The example analyzed above can be generalized to different types of connections and conductors (solid and stranded) [11].

$$\begin{aligned}\left(\left[S^{t+\Delta t}\right]+\frac{2\sigma}{\Delta t}\left[T\right]+l\left[W\right]\left[N\right]\left[G_b\right]\left[N\right]\left[W\right]^T\right)&\left\{A^{t+\Delta t}\right\}=\\ \left(-\left[S^{t}\right]+\frac{2\sigma}{\Delta t}\left[T\right]+l\left[W\right]\left[N\right]\left[G_b\right]\left[N\right]\left[W\right]^T\right)&\left\{A^{t}\right\}\\ +\left[T\right]\left[\tfrac{\sigma}{l}Q\right]&\left\{u_{mas,ext}^{(t+\Delta t)+t}\right\}+\Delta t\left[W\right]\left[N\right]\left[G_a\right]\left\{u_{ext}^{(t+\Delta t)+t}\right\}\\ -\left(\left[W\right]\left[N\right]\left[G_a\right]\left[G_c\right]-\left[W\right]\left[N\right]\right)&\left\{i_{cab}^{t}\right\}\end{aligned} \tag{24}$$

So, by example, if a specific problem includes windings of stranded conductors with star connection and other windings with whatever connections, the contribution of the star connected windings to the terms of (24) is obtained from (23).

The matrices in (24) maintain the sparsity, symmetry and positive-definiteness of the traditional FEM. Obviously, sparsity depends on geometry and the number of nodes since the mean magnetic vector potential introduces connections among the nodes of the windings modelled with stranded conductors (14).

Defining n, m and p as the number of nodes, and windings made of stranded and solid conductors respectively, the

meaning and dimensions of the terms in (24) can be expressed as:

- $[S]_{nxn}$ is the stiffness matrix.
- $[T]_{nxn}$ is called the mass matrix, containing information about the current distribution.
- $[W]_{nxm}$ is the phase matrix showing information about the distribution of windings made of stranded conductors. It is composed of the phase vectors defined in (14).
- $[G_a]_{mxm}$, $[G_b]_{mxm}$ and $[G_c]_{mxm}$ take into account how the windings defined in [W] are connected. In (18) and (20) they are defined to star connections.
- $\{A^{t+\Delta t}\}_n$ is the vector of unknown nodal values representing the value of the magnetic vector potential at the current time step $t+\Delta t$
- $\{A^t\}_n$ represents the value of the magnetic vector potential at the previous time step t.
- [Q] has the same meaning in solid conductors as [W] in stranded conductors.
- $\left\{u_{mas,ext}^{(t+\Delta t)+t}\right\}_p$ represents the addition of voltages applied to the solid conductors at the current time step $t+\Delta t$ and at the previous time step t.
- $\left\{u_{ext}^{(t+\Delta t)+t}\right\}_m$ represents the addition of voltages applied to the stranded conductors at the current time step $t+\Delta t$ and at the previous time step t.
- $\left\{i_{cab}^{t}\right\}_m$ represents the value of current at the previous time step in conductors defined as stranded.

5 COMPUTATION OF ENGINEERING RESULTS

As shown in (23) and (24), currents in windings must be calculated during the solution stage. Besides, this computational cost must be kept as low as possible. Other engineering results such as inductance, magnetic flux and electromotive force can be obtained by making use of the terms defined in (24), computed at each time step avoiding time consuming calculations in the postprocessing stage.

5.1 Current Calculations

The winding currents can be calculated using:

$$i_f(t) = \int_{\Omega_f} \mathbf{J}(t)\ d\Omega \tag{25}$$

In solid conductors (25) can be expressed as:

$$I_c = \iint_{S_c} \left(\sigma \frac{u_s}{l} - \sigma \frac{\partial \mathbf{A}}{\partial t} \right) dS \tag{26}$$

Current in windings made of conductors considered as stranded ones can be calculated using (1), (5) and the definition of phase vector:

$$\left[S^{t+\Delta t}\right]\left\{A^{t+\Delta t}\right\} = \left\{I^{t+\Delta t}\right\} = \sum_{k=1}^{m} N_k \left\{\omega_k\right\}\ i_k^{t+\Delta t} \tag{27}$$

Where m is the number of windings. The current of a winding (i) can be computed multiplying both terms in (27) by the transposed i-phase vector $\{\omega_i\}^T$, taking into account that the product of $\{\omega_i\}^T$ and $\{\omega_k\}$ is null when k is not the same as i:

$$i_i^{t+\Delta t} = \frac{\left\{\omega_i\right\}^T \left[S^{t+\Delta t}\right]\left\{A^{t+\Delta t}\right\}}{N_i \left\{\omega_i\right\}^T \left\{\omega_i\right\}} \tag{28}$$

This method computes the phase current using as data, the phase vector, the number of turns, together with the stiffness matrix and the vector of the magnetic vector potential nodal values at the current time step $t+\Delta t$. Therefore, all the terms in (28) are computed during the solution stage of FEM.

5.2 Flux and Electromotive Force Calculations

These results can be easily computed using (13) and (14).

5.3 Inductance Calculations

Inductance has a geometrical meaning when all the materials exhibit a linear behaviour. In other case, several non-coincident definitions can be taken into account [12]. Using the definition based on flux linkages, self-inductance can be calculated in windings made of stranded conductors as:

$$\begin{aligned} L_i^{t+\Delta t} &= \frac{N_i \phi^{t+\Delta t}}{i_i^{t+\Delta t}} = \frac{l N_i \left\{\omega_i\right\}^T \left\{A^{t+\Delta t}\right\}}{\dfrac{\left\{\omega_i\right\}^T \left[S^{t+\Delta t}\right] \left\{A^{t+\Delta t}\right\}}{N_i \left\{\omega_i\right\}^T \left\{\omega_i\right\}}} \\ &= l N_i^2 \left\{\omega_i\right\}^T \left[S^{t+\Delta t}\right]^{-1} \left\{\omega_i\right\} \end{aligned} \tag{29}$$

In the same way mutual inductance can be computed using the flux linkage definition:

$$\begin{aligned} M_{ij}^{t+\Delta t} &= \frac{N_i \phi_i^{t+\Delta t}}{i_j^{t+\Delta t}} = \frac{l N_i \left\{\omega_i\right\}^T \left\{A^{t+\Delta t}\right\}}{\dfrac{\left\{\omega_j\right\}^T \left[S^{t+\Delta t}\right] \left\{A^{t+\Delta t}\right\}}{N_j \left\{\omega_j\right\}^T \left\{\omega_j\right\}}} \\ &= l N_i N_j \left\{\omega_i\right\}^T \left[S^{t+\Delta t}\right]^{-1} \left\{\omega_j\right\} \end{aligned} \tag{30}$$

As the current is computed in (28), self and mutual inductances are calculated using the phase vectors and the stiffness matrix, that can be dependent on time. Stiffness

matrix is affected by the B-H curve when it exhibits a nonlinear behaviour.

In [13] the inductance computation in case of solid conductors is stated.

6 EXAMPLES

A software package has been developed implementing (24). It has been tested with many examples of increasing complexity over transformers, considering several balanced and unbalanced connections in primary and secondary –one phase and three phase transformers–, steady and unsteady states, sinusoidal and nonsinusoidal voltages and current sources (balanced and unbalanced); two of these examples are presented below.

6.1 Steady-state

The model is applied to a 3 kVA three-phase ΔY transformer (figure 2). The transformer is supplied with a balanced nonsinusoidal three-phase voltage (figure 3), generated with a programmable AC power source. These waveforms are applied to the software package using files obtained from an oscilloscope. The secondary is loaded with an unbalanced three-phase RL impedance. Figure 4 shows the simulated currents in steady state, and figure 5 shows the computed and measured currents.

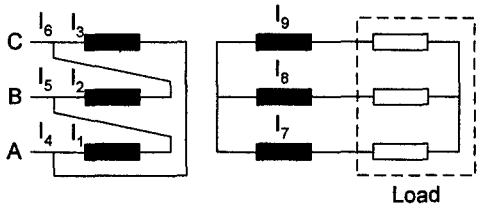

Figure 2. The transformer is delta-star connected.

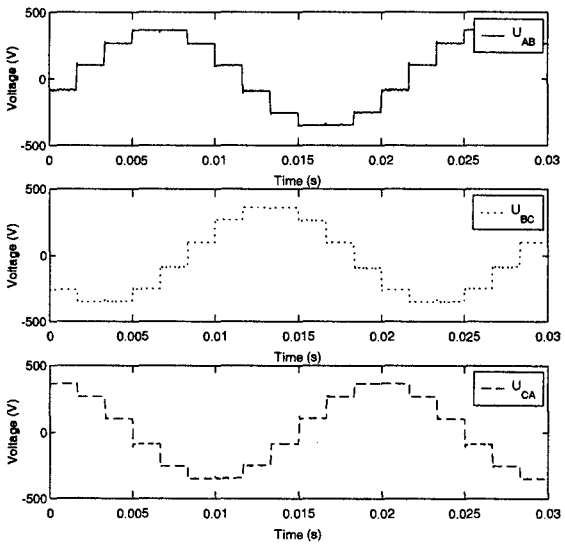

Figure 3. Line-to-line supplied voltages.

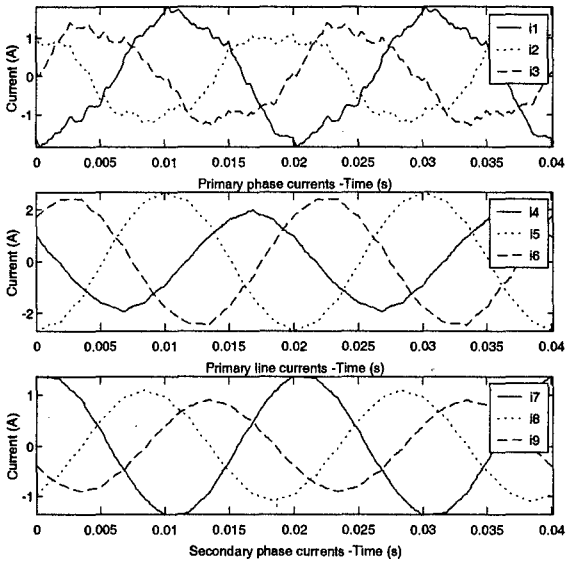

Figure 4. Primary and secondary computed currents.

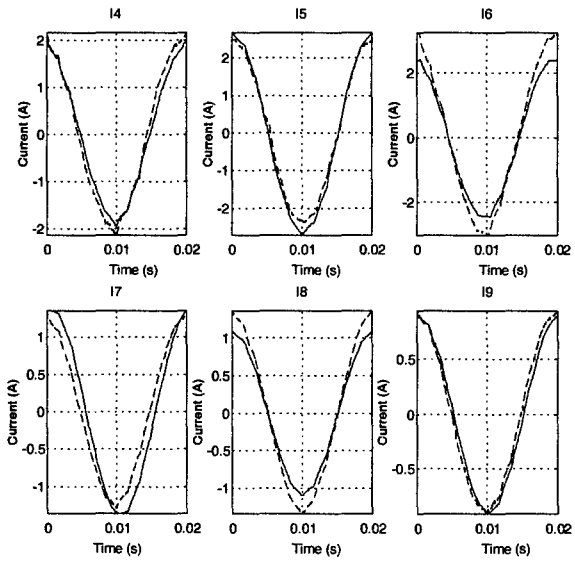

Figure 5. Computed (solid) and measured (dashed) currents.

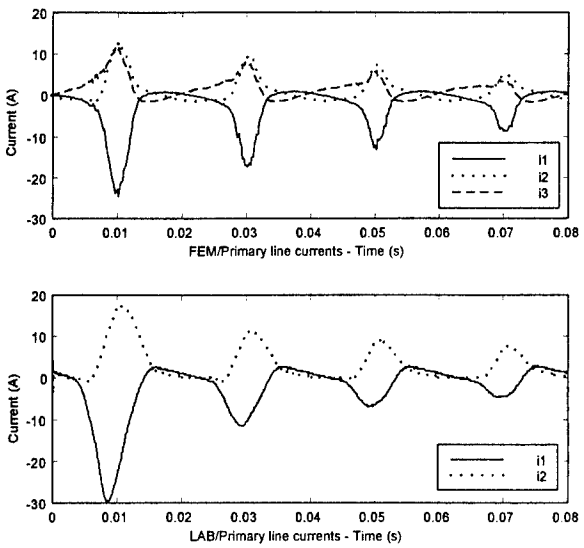

Figure 6. Computed (FEM) and measured (LAB) currents.

6.2 Non steady-state

The transformer is now YY connected, and loaded with the same unbalanced three-phase RL impedance. Figure 6 shows the computed and measured primary currents; the discrepancies between them are due to the unfavourable conditions of the high supply voltage and the instant chosen for the switching-on of the transformer.

7 CONCLUSIONS

A generalized approach for FEM and external circuits coupling has been presented considering both types of conductors simultaneously, stranded and solid respectively. This model has been established using a bottom-up methodology. The meanings of the terms of the particularized equation (23) have been generalized to obtain the terms in general equation (24). Indeed, when a problem containing a particularized example is selected, the expressions of these are included in the terms of (24).

Current, magnetic flux, electromotive force and inductance definitions have been obtained using some terms of (24), simplifying their notation and speeding-up their computation during the solution stage rather than during the postprocessing stage.

Finally, the approach, implemented in a software package developed by the authors, has been applied to several cases. The results have shown a good agreement with those measured in the lab.

8 REFERENCES

[1] A. Y. Hannalla and D. C. Macdonald, "Numerical analysis of transient field problems in electrical machines" *Proc. IEE*, vol. 123, no. 9, pp. 893-898, 1976.

[2] H. De Gersem, R. Mertens, U. Pahner, K. Hameyer and R. Belmans, "Coupled field-circuit problem: a generalized signal flow graph description of the circuit equations" *Eur. Phys. J. AP*, vol 1, pp. 247-251, 1998.

[3] J. Väänänen, "Circuit theoretical approach to couple two-dimensional Finite Element Models with external circuit equations" *IEEE Trans. Magn.*, vol. 32, no. 2, pp. 400-410, 1996.

[4] F. Piriou and A. Razek, "Finite Element analysis in electromagnetic systems. Accounting for electric circuits" *IEEE Trans. Magn.*, vol. 29, no. 2, pp. 1669-1675, 1993.

[5] I. A. Tsukerman, A. Konrad, G. Meunier and J. C. Sabonnadière, "Coupled field-circuit problems: Trends and accomplishments" *IEEE Trans. Magn.*, vol. 29, no. 2, pp. 1701-1704, 1993.

[6] A. Nicolet, F. Delincé, N. Bamos, A. Genon and W. Legros, "A coupling between electric circuits and 2D magnetic field modelling" *IEEE Trans. Magn.*, vol. 29, no. 2, pp. 1697-1700, 1993.

[7] J. R. Brauer, B. E. MacNeal and F. Hirtenfelder, "New constraint technique for 3D finite element analysis of multiturn windings with attached electric circuits" *IEEE Trans. Magn.*, vol. 29, no. 6, pp. 2446-2448, 1993.

[8] S. J. Salon, *Finite Element analysis of electrical machines*. Kluwer Academic Publishers, 1995.

[9] B. Thidé, *Electromagnetic field theory*, Upsilon books, http://www.plasma.uu.se/CDE/Book, 2002.

[10] J. Roger-Folch and V. J. Lázaro, "Contribution to the transient analysis of induction motors solving the electrodynamic equations by using the Finite Element Method", *COMPEL*, vol. 14, No. 4, pp. 93-96, 1995.

[11] J. Roger-Folch, E. Gómez and V. J. Lázaro, "Time-stepping Finite Element Analysis of Transformers in 2D", *International Symposium on Electromagnetic Fields in Electrical Engineering*, pp. 241-244, September, Gdansk (Poland), 1997.

[12] D. A. Lowther and P.P. Silvester, *Computer-Aided Design in Magnetics*. Springer Verlag, 1986.

[13] J. Roger Folch, V. J. Lázaro and E. Gómez, "Mutual Inductance Computation using the 2D Finite Element Method", *International Conference on Electrical Machines*, pp. 1408-1411, Istanbul (Turkey), 1998.

Emilio Gómez Lázaro was born in Albacete, Spain. He received his MSc. and Ph.D. degrees, from Universidad Politécnica de Valencia, respectively in 1995 and 2000; both in Electrical Engineering. He has held teaching and research positions at Universidad Politécnica de Valencia and Universidad Jaume I, Spain. Currently, he is an Associate Professor of Electrical Engineering at Universidad Politécnica de Cartagena in Murcia, Spain. His current research interests include numerical methods for electromagnetism, large-scale parallel computing and, more generally, scientific computing and engineering.

Antonio Gabaldón Marín was born in Murcia, Spain. He received his MSc. in Electrical Engineering from Universidad Politécnica de Valencia, Spain, in 1988, and his Ph.D. degree from the same University in 1991. Currently, he is working at Department of Electrical Engineering of Universidad Politécnica de Cartagena, Spain. His research interests include Demand-Side Management, End-Use Efficiency, Modelling and Distribution Automation, and numerical methods for electromagnetism.

José Roger-Folch obtained his MSc. in Electrical Engineering in 1970 from the Universidad Politécnica de Cataluña and his Ph.D. in 1980 from the Universidad Politécnica de Valencia, Spain. From 1971 to 1978 he worked in the Electrical Industry as Project Engineer. Since 1978, he joined the Universidad Politécnica de Valencia and he is currently Professor of Electrical Installations and Machines. His main research areas are the Numerical Methods (F.E.M. and others) applied to the Design and Maintenance of Electrical Machines and Equipments.

Angel Molina García was born in Murcia, Spain. He received his MSc. in Electrical Engineering from Universidad Politécnica de Valencia, Spain, in 1998. Currently, he is working towards his Ph.D. at Department of Electrical Engineering of Universidad Politécnica de Cartagena, Spain. His research interests include Demand-Side Management, Demand-Side Bidding, residential load modelling, large-scale parallel computing and scientific computing and engineering.

Use of the Simultaneous Diagonalization Technique in the $A\bar{x} = \lambda B\bar{x}$ Eigenproblem Applied to the Computation of the Characteristic Modes

G. ANGIULLI† AND F. VENNERI‡

†Dip. di Informatica, Matematica Elettronica e Trasporti
Università *Mediterranea*
89100 Reggio Calabria, Italy.

‡Dip. di Elettronica, Informatica e Sistemistica
Università della Calabria
87036 Rende (Cs), Italy.

Abstract- Characteristic modes developed by Garbacz, Harrington and Mautz have long been used in the analysis of radiation and scattering from conducting bodies and apertures. For their computation, it is necessary to solve an eigensystem of the form $\mathbf{A}\bar{x} = \lambda\mathbf{B}\bar{x}$. If the matrices $(\mathbf{A}, \mathbf{B})$ are Hermitian and $\mathbf{B}$ is positive definite, the generalized eigenvalue problem can be accurately solved using the simultaneous diagonalization technique (SDT). Because of numerical approximations and rounding sometimes it may happen that the matrices properties deteriorate and the SDT procedure becomes inapplicable. In this work a new technique, developed recently by Higham and Cheng is proposed as a method to solve these deteriorate cases. It is applied to the computation of the characteristic modes for some scattering problems. Results are analyzed and discussed.

1. Introduction

The generalized eigenvalue problem:

$$\mathbf{A}\bar{x} = \lambda\mathbf{B}\bar{x} \qquad (1)$$

is often encountered in computational electromagnetics [1]. The solution of (1) depends on properties of the matrices $\mathbf{A}$ and $\mathbf{B}$ resulting from the discretization of the field equations. If these matrices are not singular, then (1) can be reduced to the solution of the standard eigenproblem:

$$\mathbf{H}\bar{x} = \lambda\bar{x} \quad with \quad \mathbf{H} = \mathbf{B}^{-1}\mathbf{A} \qquad (2)$$

However, if $\mathbf{A}$ and $\mathbf{B}$ are Hermitian and $\mathbf{B}$ is positive definite, the problem (1) can be solved with a higher degree of accuracy applying the *simultaneous diagonalization technique* (SDT) to the matrices $(\mathbf{A}, \mathbf{B})$ than the direct calculation of the inverse matrix $\mathbf{B}^{-1}$ [2]. Although the underlined properties are sometimes held of the matrices issued in electromagnetic problems, unfortunately the discretization performed by numerical algorithms on the electromagnetic field equations often causes the loss of these properties. As a consequence, the SDT becomes inapplicable. Recently, Higham and Cheng have faced the above problem from a theoretical point of view and they have proposed a technique that allows to use the SDT even in presence of discretization errors. This method is based on the concept of *nearest definite pair* [3]. In this work, we have applied Higham-Cheng results to evaluation of the characteristic modes for the scattering from conducting bodies. The paper is organized as follows: section II presents the basics on the theory of characteristic modes for conduct-

ing bodies. Section III and IV illustrate the SDT procedure for the resolution of the positive definite Hermitian generalized eigenproblem and its extension. In section V we show the numerical results. Finally, in section VI, the conclusions.

2. Theory of Characteristic Modes for Conducting Bodies

The characteristic modes have been intensively used in the analysis of radiation and scattering from conducting bodies and apertures [4]-[13]. They are numerical entire basis functions that in principle can be computed for any object shape. Since these eigenfunctions include the behavior of unknown current density flowing on the metallic bodies and apertures, only a small number of them are required for a good reconstruction of it. So, if available, characteristic modes would lead to a scattering or radiation problem treatable with a classical Method of Moment even in presence of a large number of objects [10]-[13]. In the case of scattering or radiation from conducting bodies, these modes are basically solutions of a generalized eigenproblem involving the impedance operator $\mathcal{Z}$, which relates the surface current $\bar{J}$ on a conducting body to the tangential component of the incident electric field $\bar{E}_{Tan}^{Inc}$ on it, i.e. [5]:

$$\mathcal{Z}\bar{J} = \bar{E}_{Tan}^{Inc} \tag{3}$$

One method to solve a functional equation of the form (3) is to obtain a modal solution in terms of eigenfunctions of $\mathcal{Z}$. For this purpose, we consider the operational eigenproblem:

$$\mathcal{Z}\bar{J}_k = \nu_k \mathcal{M}\bar{J}_k \tag{4}$$

in which $\mathcal{M}$ is a suitable weight operator and $\nu_k = 1 + j\lambda_k$. The operator $\mathcal{Z}$ can be uniquely represented in the form:

$$\mathcal{Z} = \mathcal{R} + j\mathcal{X} \tag{5}$$

where the operators $\mathcal{R}$ and $\mathcal{X}$ are defined as:

$$\mathcal{R} = \frac{\mathcal{Z} + \mathcal{Z}^*}{2} \tag{6}$$

$$\mathcal{X} = \frac{\mathcal{Z} - \mathcal{Z}^*}{2j} \tag{7}$$

Note that $\mathcal{R}$ and $\mathcal{X}$ are real selfadjoint operators and furthermore $\mathcal{R}$ is positive definite [5]. The choice $\mathcal{M} = \mathcal{R}$ reduces the complex operatorial eigenproblem (4) to a real operatorial eigenproblem:

$$\mathcal{X}\bar{J}_k = \lambda_k \mathcal{R}\bar{J}_k \tag{8}$$

The eigenfunctions $\bar{J}_k$ have been named *characteristic modes* [5]. They can be numerically evaluated through the reduction of the operator equation (8) to a matrix equation using the Method of Moment [5],[10]. For this aim the *k-th* modal current density on the metallic body is expanded in a set of N suitable subsectional basis functions $\bar{B}_n$:

$$\bar{J}_k = \sum_{n=1}^{N} I_n \bar{B}_n \tag{9}$$

where the I_n are unknown complex constants. Substitution of (9) into (8) and application of the Galerkin method leads to a matrix equation of the form:

$$\mathbf{X}\bar{I}_k = \lambda_k \mathbf{R}\bar{I}_k \tag{10}$$

where $\bar{I}_k$ is the column vector of the unknown coefficients I_n. Equation (10) is a generalized eigensystem of the form (1) in which the eigenvalues λ_k and the eigenvectors $\bar{I}_k$ approximate the eigenvalues and the eigenfunctions of the equation (8). It follows by $\mathcal{X}$ and $\mathcal{R}$ properties that the matrices $\mathbf{X}$ and $\mathbf{R}$ are expected Hermitian and furthermore $\mathbf{R}$ is expected positive definite. Consequently, in principle it is possible to use the SDT for solving the eigensystem (1). But because of numerical approximation, the $\mathbf{R}$ matrix often becomes indefinite and the SDT algorithm becomes inapplicable. In the following, it will be shown that the use of the nearest definite pair technique permits to employ the SDT giving a significant improvement in the evaluation of the characteristic modes over the direct inversion technique.

3. Resolution of the Positive Definite Generalized Eigenproblem with the Simultaneous Diagonalization Technique

The generalized eigenproblem where the matrices $\mathbf{A}$ and $\mathbf{B}$ are Hermitian and in which one is positive definite plays an important role in matrix theory. If we assume, without loss of

generality, that $\mathbf{B}$ is positive definite, the problem (1) can be accurately solved by means of a method named *simultaneous diagonalization technique* [2] as follows: Let $\mathbf{U}_1$ be an unitary matrix whose columns are an orthonormal set of eigenvectors for $\mathbf{B}$. Premultiplying and postmultiplying (1) by $\mathbf{U}_1^*$ and $\mathbf{U}_1$, where the star denotes the complex conjugate transpose operation, and taking into account that:

$$\mathbf{U}_1^*\mathbf{U}_1 = \mathbf{U}_1\mathbf{U}_1^* = diag(1) \tag{11}$$

where $diag(1)$ is the identity matrix, we obtain:

$$\dot{\mathbf{A}}\bar{y} = \lambda\dot{\mathbf{B}}\bar{y} \tag{12}$$

in which the matrices $\dot{\mathbf{A}}$, $\dot{\mathbf{B}}$ and the vector $\bar{y}$ are of the form:

$$\begin{aligned} \dot{\mathbf{A}} &= \mathbf{U}_1^*\mathbf{A}\mathbf{U}_1 \\ \bar{y} &= \mathbf{U}_1^*\bar{x} \\ \dot{\mathbf{B}} &= \mathbf{U}_1^*\mathbf{B}\mathbf{U}_1 = diag(\mu) \end{aligned} \tag{13}$$

and in which $diag(\mu)$ is the diagonal matrix formed by eigenvalues of the $\mathbf{B}$ matrix. Next, we introduce the nonsingular transformation $\mathbf{H}$:

$$\mathbf{H} = diag(\mu^{-\frac{1}{2}}) \tag{14}$$

Using $\mathbf{H}$ in (12), we obtain:

$$\ddot{\mathbf{A}}\bar{z} = \lambda\ddot{\mathbf{B}}\bar{z} \tag{15}$$

where $\ddot{\mathbf{A}}$, $\bar{z}$ and $\ddot{\mathbf{B}}$ are:

$$\begin{aligned} \ddot{\mathbf{A}} &= \mathbf{H}^*\dot{\mathbf{A}}\mathbf{H} \\ \bar{z} &= \mathbf{H}^{-1}\bar{y} \\ \ddot{\mathbf{B}} &= \mathbf{H}^*\dot{\mathbf{B}}\mathbf{H} = diag(1) \end{aligned} \tag{16}$$

Finally, if we construct an unitary matrix $\mathbf{U}_2$ whose columns are an orthonormal set of eigenvectors for $\ddot{\mathbf{A}}$, the matrix transformation $\mathbf{T} = \mathbf{U}_1\mathbf{H}\mathbf{U}_2$ permits simultaneously to reduce the matrices $\mathbf{A}$, $\mathbf{B}$ to diagonal form:

$$\left.\begin{aligned} \mathbf{T}^*\mathbf{A}\mathbf{T} &= diag(\lambda) \\ \mathbf{T}^*\mathbf{B}\mathbf{T} &= diag(1) \end{aligned}\right\} \tag{17}$$

resolving the eigenproblem (1). An efficient implementation of the above procedure that utilizes both the Cholesky factorization and the symmetric QR algorithm is described in [14].

4. Extension of the Simultaneous Diagonalization Technique

The application of the procedure discussed in the previous section is not limited to the treatment of Hermitian pairs $(\mathbf{A}, \mathbf{B})$ with $\mathbf{B}$ positive definite, but sometimes it can be extended to the Hermitian pairs in which the $\mathbf{B}$ matrix is indefinite. For this aim, the concept of definiteness has been restated referring directly to the matrix pair $(\mathbf{A}, \mathbf{B})$ rather than to a single matrix $\mathbf{B}$. More in details, pair $(\mathbf{A}, \mathbf{B})$ having *Crawford number* γ [15], denoted as:

$$\gamma(\mathbf{A}, \mathbf{B}) = \min_{\|\bar{z}\|_2=1} \sqrt{(\bar{z}^*\mathbf{A}\bar{z})^2 + (\bar{z}^*\mathbf{B}\bar{z})^2} \tag{18}$$

strictly positive has been named as *definite* and, when $\gamma = 0$ the pair has been named as *indefinite*. Also, it is possible evaluate the definiteness of a Hermitian pair $(\mathbf{A}, \mathbf{B})$ drawing its *Field of Values* $F(\mathbf{A} + j\mathbf{B})$ in the complex plane. The field of values is defined as the set of all the values assumed by the Rayleigh quotients of the pair [3]:

$$F(\mathbf{A} + j\mathbf{B}) = \frac{z^*(\mathbf{A} + j\mathbf{B})z}{z^*z} \quad z \neq 0 \tag{19}$$

The pair will be *definite* if and only if zero does not lie in $F(\mathbf{A} + j\mathbf{B})$, otherwise it will be *indefinite*. A solution of (1) in which $\mathbf{B}$ is indefinite, but the Crawford number γ of the pair $(\mathbf{A}, \mathbf{B})$ is positive, has been given in [15] by means of the *Stewart's theorem* [16]. This theorem ensured the existence of an angle $\theta \in [0, 2\pi)$ that permits to define, starting from a given pair $(\mathbf{A}, \mathbf{B})$ with $\gamma > 0$, a new pair $(\mathbf{A}_\theta, \mathbf{B}_\theta)$ in which $\mathbf{B}_\theta$ is positive definite, as follows:

$$\left.\begin{aligned} \mathbf{A}_\theta &= \mathbf{A}\cos\theta + \mathbf{B}\sin\theta \\ \mathbf{B}_\theta &= -\mathbf{A}\sin\theta + \mathbf{B}\cos\theta \end{aligned}\right\} \tag{20}$$

For this new pair is now applicable the SDT. The eigenvalues λ of the old pair $(\mathbf{A}, \mathbf{B})$ and the eigenvalues λ_θ of the new pair $(\mathbf{A}_\theta, \mathbf{B}_\theta)$ are simply related by:

$$\lambda = \frac{\lambda_\theta\cos\theta - \sin\theta}{\lambda_\theta\sin\theta + \cos\theta} \tag{21}$$

However, it may happen that the discretization errors may affect the matrices in a way that a pair $(\mathbf{A}, \mathbf{B})$ theoretically expected to be definite becomes indefinite in practice. As a consequence the SDT cannot be applied. For this last case it can be useful evaluate the nearest definite pair $(\mathbf{A} + \Delta\mathbf{A}, \mathbf{B} + \Delta\mathbf{B})$ and attempt to resolve the problem (1) for this one. Else, assigned the indefinite Hermitian pair $(\mathbf{A}, \mathbf{B})$, we must find the nearest Hermitian definite pair

$(\mathbf{A}+\Delta\mathbf{A}, \mathbf{B}+\Delta\mathbf{B})$, having a specified Crawford number $\gamma = \delta > 0$ according to the distance [3],[17]:

$$d_\delta(\mathbf{A},\mathbf{B}) = min\{|||[\Delta\mathbf{A}\ \Delta\mathbf{B}]|||_2 : \gamma(\mathbf{A}+\Delta\mathbf{A}, \mathbf{B}+\Delta\mathbf{B}) = \delta\} \quad (22)$$

and the angle θ by means of which the nearest pair can be simultaneously diagonalized. This problem has been recently solved by Higham and Cheng by means of the following theorem [3]:

Higham-Cheng's Theorem: Let $\mathbf{A}, \mathbf{B} \in \mathcal{C}^{n\times n}$ be Hermitian and let $\mathbf{C} = \mathbf{A} + j\mathbf{B}$ and $\mathbf{A}_\phi = \mathbf{A}cos(\phi) + \mathbf{B}sin(\phi)$. Let $\min_{(0\le\phi\le 2\pi)} \lambda_{max}(\mathbf{A}_\phi)$ be attained at the angle θ and let $\mathbf{A}_\theta$ have the spectral decomposition:

$$\mathbf{A}_\theta = \mathbf{Q}diag(\mu_k)\mathbf{Q}^* \quad with \quad \mu_n \le ... \le \mu_1 \quad (23)$$

If $0 \in F(\mathbf{C})$ then:

$$d_\delta(\mathbf{A},\mathbf{B}) = \delta + \mu_1 \quad (24)$$

If $0 \notin F(\mathbf{C})$ then:

$$d_\delta(\mathbf{A},\mathbf{B}) = max(\delta + \mu_1, 0) \quad (25)$$

In both cases, two sets of optimal perturbations in (22) are:

$$\left.\begin{aligned}\Delta\mathbf{A}_1 &= \mathbf{Q}diag(min(-\delta+\mu_k, 0))\mathbf{Q}^*\cos\theta \\ \Delta\mathbf{B}_1 &= \mathbf{Q}diag(min(-\delta+\mu_k, 0))\mathbf{Q}^*\sin\theta\end{aligned}\right\} \quad (26)$$

and

$$\left.\begin{aligned}\Delta\mathbf{A}_2 &= -d_\delta(\mathbf{A},\mathbf{B})diag(1)\cos\theta \\ \Delta\mathbf{B}_2 &= -d_\delta(\mathbf{A},\mathbf{B})diag(1)\sin\theta\end{aligned}\right\} \quad (27)$$

A detailed demonstration of this theorem can be found in [3]. The most important consequence of the above results is that the SDT can be generalized to the Hermitian pairs $(\mathbf{A}, \mathbf{B})$ having $\mathbf{B}$ matrix indefinite.

5. Numerical Results

In order to check the validity and accuracy of the foregoing procedure in the computation of characteristic modes for conducting bodies, numerical results for some cases are carried out. Firstly, characteristic modes have been computed for the TM_z scattering from a perfectly conducting circular cylinder and from an elliptic one, since for these cases characteristic modes are known in analytical form [12]. In Fig.(1) are represented the geometries for both problems. In Fig.(2) is reported the plot of the smaller eigenvalues of the $\mathbf{R}$ matrix obtained discretizing the EFIE for the scattering due to a plane wave impinging on a metallic circular cylinder with radius $\frac{\lambda}{2}$. Pulse basis functions and delta function testing functions are used to create the matrix $\mathbf{R}$ [1]. Since only the properties of the matrices above are considered here for the computation of characteristic modes, it is not necessary to specify the direction of the incident field. The depicted eigenvalues are scaled to show the relative value only. This plot clearly shows that the $\mathbf{R}$ matrix is indefinite, even if it is expected definite because the properties of the operator $\mathcal{R}$. In Fig.(3) is plotted the field of values for the pair $(\mathbf{X}, \mathbf{R})$. Because the origin of the complex plane is not contained in $F(\mathbf{X} + j\mathbf{R})$ this pair is definite. In Figs.(4) and (5) are reported the plot of the smaller eigenvalues of the $\mathbf{R}$ ma-

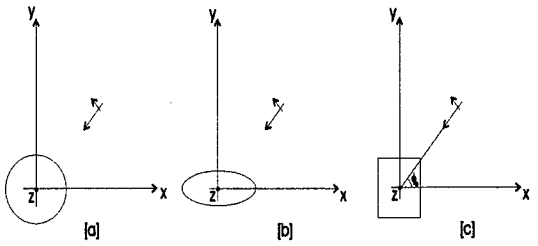

Figure 1: Geometry for scattering from circular, elliptic and square metallic cylinders.

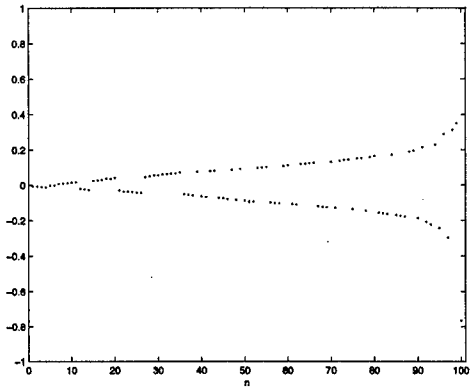

Figure 2: Plot of the smaller normalized eigenvalues for the TM_z scattering from a circular cylinder of radius $a = \frac{\lambda}{2}$ (Problem Size 128 × 128).

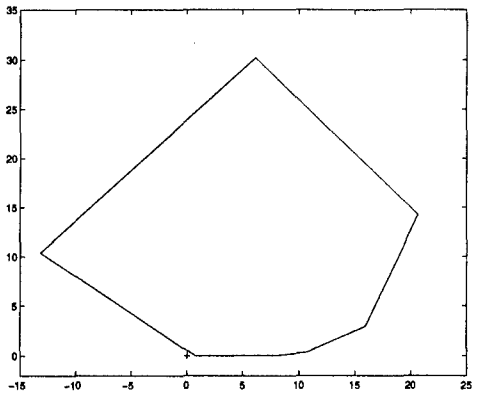

Figure 3: Field of Values for pair related to computation of characteristic modes for circular cylinder.

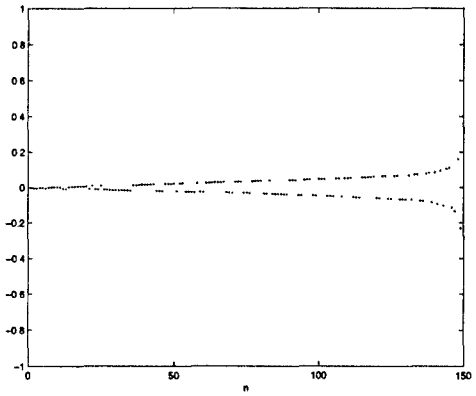

Figure 4: Plot of the smaller normalized eigenvalues for the TM_z scattering from an elliptic cylinder with semi major axis $a = \lambda$ and semi minor axis $b = \frac{\lambda}{4}$ (Problem Size 180 x 180).

trix and the field of values $F(\mathbf{X} + j\mathbf{R})$ for the pair obtained considering the scattering from a metallic elliptic cylinder with semi major axis $a = \lambda$ and semi minor axis $b = \frac{\lambda}{4}$ by an incident plane wave. For this scattering problem we have obtained both an indefinite matrix $\mathbf{B}$ and an indefinite pair $(\mathbf{X}, \mathbf{R})$ as clearly depicted in these figures. In Table (1) are shown the analytical eigenvalues versus the numerical ones for the previously analyzed scattering problems. Numerical eigenvalues have been obtained using both the Higham-Cheng procedure and the direct inversion technique. Excellent agreement is shown comparing the exact eigenvalues and the numerical ones computed by means of the former procedure while the eigenvalues obtained using the direct inversion technique are very inaccurate. As last case, consider the evaluation of the characteristic modes for the scattering from a metallic square cylinder of side $a = \lambda$. In Figs.(1) and (6) are reported the geometry for the problem and its field of values, respectively. As it is shown in Fig.(6), the matrix pair $(\mathbf{X}, \mathbf{R})$ for this case is definite because the field of values does not contain the origin of the complex plane. In Fig. (7) is shown the obtained current distribution on the cylinder by a plane wave impinging at an angle $\phi_0 = 0$. The continuous line indicates the current computed by means of the standard MoM while crosses indicate the solution obtained using characteristic modes computed using the Higham-Cheng procedure. A very good agreement is clearly observed.

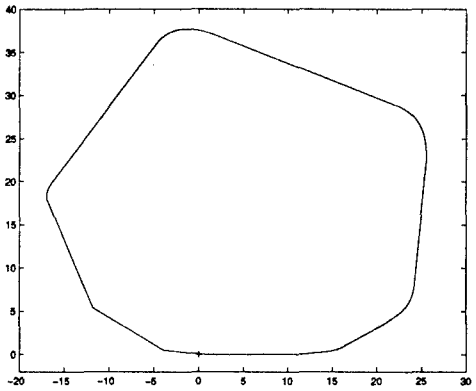

Figure 5: Field of Values for pair related to computation of characteristic modes for elliptic cylinder.

6. Conclusions

A technique developed by Higham and Cheng for the treatment of the Hermitian generalized eigenproblem based on the concept of nearest definite pair has been proposed for the computation of the characteristic modes. Numerical results for some scattering problems are presented. In all the cases, the outlined procedure, even if acting on very ill conditioned matrices, provides very accurate numerical results. Finally, we point out that the application of the method is not limited to the presented cases being fruitfully applicable to a wide number of electromagnetic problems which posses the discussed properties [18].

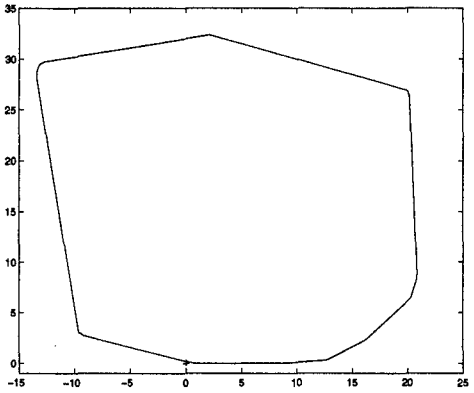

Figure 6: Field of Values for pair related to computation of characteristic modes for square cylinder (Problem Size 165 × 165).

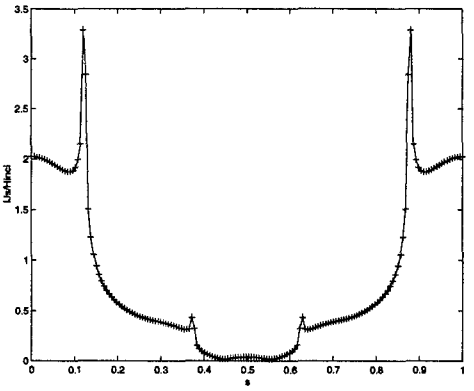

Figure 7: Plot of the current density on the metallic square cylinder. The continuous line indicate solution computed by means of the MoM. Crosses indicate solution obtained using characteristic modes.

Exact Solution *(circular cylinder)* cond(**X**)=1.29e+01 cond(**R**)=5.56e+17	**Higham-Cheng Solution**	**Direct Inversion**
-0.12609	-0.12609	-35.6120-32.1893j
-0.12609	-0.12609	-35.6120+32.1893j
1.07929	1.07921	49.1555
0.20579	0.20572	14.8938+76.7077j
0.20579	0.20572	14.8938-76.7077j
Exact Solution *(elliptic cylinder)* cond(**X**)=3.22e+01 cond(**R**)=3.54e+18	**Higham-Cheng Solution**	**Direct Inversion**
-0.958287	-0.961337	-3.34497 +1.71189j
-0.143256	-0.143658	-0.987728-1.30952j
0.139654	0.137123	1.305403
0.454565	0.451928	-0.987728+1.30952j
0.831470	0.832260	-2.58841

Table 1: Analytical vs. numerical eigenvalues.

References

[1] R. Harrington, "*Field Computation by Moment Methods*", *Macmillan*, New York, 1968.

[2] J. H. Wilkinson, "*The Algebraic Eigenvalue Problem*", *Oxford*, New York, 1965.

[3] S. H. Cheng, N. J. Higham, "*The Nearest Definite Pair for the Hermitian Generalized Eigenvalue Problem*", Linear Algebra Appl., vol. 302–303, pp.63–76, 1999.

[4] R. J. Garbacz, "*Modal Expansions for Resonance Scattering Phenomena*", Proc. of IEEE, vol.53, pp.856–864, 1965.

[5] R. F. Harrington and J. R. Mautz, "*Theory of Characteristic Modes for Conducting Bodies*", IEEE Trans. on AP, vol. 19, pp.622–628, 1971.

[6] R. F. Harrington and J. R. Mautz, "*Characteristic Modes for Aperture Problems*", IEEE Trans. on MTT, vol. 33, pp.500–505, 1985.

[7] A. El-Hajj, K.Y. Kabalan, R. F. Harrington, "*Characteristic Mode of a Slot in a Conducting Cylinder and Their Use for Penetration and Scattering, TE case*", IEEE Trans. on AP, vol. 40, pp.156–161, 1992.

[8] M. Davidoviz, "*Continuous Spectrum and Characteristic Modes of the Slot Line in Free Space*", IEEE Trans. on MTT, vol. 44, pp.340–341, 1996.

[9] A. El-Hajj, K.Y. Kabalan, A. Rayes, "*Characteristic Mode Formulation of Multiple Rectangular Apertures in a Conducting Plane with a Dielectric-Filled Cavity*", IEEE Trans. on Electromagn. Compat., vol. 40, pp.89–93, 1998.

[10] O. M. Bucci, G. Di Massa, "*Use of Characteristic Modes in Multiple-Scattering Problems*", J. Phys. D: Appl. Phys., vol. 28, pp.2235–2244, 1995.

[11] G. Amendola, G. Angiulli, G. Di Massa, "*Numerical and Analytical Characteristic Modes for Conducting Elliptic Cylinders*",

Microwave and Optical Technology Letters, vol. 16, pp.243–249, 1997.

[12] G. Angiulli, G. Amendola, G. Di Massa, *"Characteristic Modes in Multiple-Scattering by Conducting Cylinders of Arbitrary Shape"*, Electromagnetics, vol. 18, pp.593–612, 1998.

[13] G. Angiulli, G. Amendola, G. Di Massa, *"Application of Characteristic Modes to the Analysis of Scattering from Microstrip Antennas"*, Journal of Electromagnetic Waves *and* Applications, vol. 14, pp.1063–1081, 2000.

[14] G. H. Golub, C. F. Van Loan, *"Matrix Computations"*, Johns Hopkins University Press, 1996.

[15] C. R. Crawford, *"A Stable Generalized Eigenvalue Problem"*, SIAM J. Numeric. Anal., vol. 13, pp.854–860, 1976.

[16] G. W. Stewart, *"Perturbation Bounds for the Definite Generalized Eigenvalue Problem"*, Linear Algebra Appl., vol. 23, pp.69–85, 1979.

[17] N. J. Higham, *"Computing a Nearest Symmetric Positive Semidefinite Matrix"*, Linear Algebra Appl., vol. 103, pp.103–118, 1988.

[18] G. Angiulli, G. Amendola, G. Di Massa, *"Application of Higham-Cheng Algorithm to the Generalised Eigenproblem in Computational Electromagnetics"*, Electr. Lett., vol. 37, pp.282–283, 2001.

Giovanni Angiulli was born in Torino, Italy in 1966. He holds a *Laurea* degree in Informatics Engineering from University of Calabria in 1993 and a Ph.D. degree in Electronic Engineering and Computer Science from the University of Napoli *"Federico II"* in 1998.
Since 1999 he is with University *"Mediterranea"* of Reggio Calabria as an Assistant Professor. His main scientific interests are in the area of numerical methods in electromagnetics.

Francesca Venneri holds a *Laurea* degree in Information Technology Engineering from the University of Calabria, Italy, in October 1998 and a Ph.D. degree in Electronic Engineering from the University *"Mediterranea"* of Reggio Calabria in 2002.
Currently she is Research Fellow at the Dipartimento di Elettronica, Informatica e Sistemistica of the University of Calabria.

FDTD Analysis of ELF Wave Propagation in Inhomogeneous Subionospheric Waveguide Models

Hayakawa, M. and T. Otsuyama
Department of Electronic Engineering, The University of Electro-Communications, 1-5-1 Chofugaoka, Chofu, Tokyo 182-8585, Japan
Tel: +81 424 43 5159, Fax: +81 424 43 5168, E-mail hayakawa@whistler.ee.uec.ac.jp

ABSTRACT. The space formed by the ground and ionosphere is known to act as a resonator for extremely low frequency (ELF) waves. Lightning discharges trigger this global resonance, which is known as Schumann resonances at the frequencies of 8, 14, 21Hz etc. Even though the inhomogeneity (like day-night asymmetry, local perturbation etc.) is important for such subionospheric ELF propagation, the previous analyses have been always made by some approximations because the problem is too complicated to be analyzed by exact full-wave analysis. This paper presents the first application of the conventional FDTD method to such subionospheric ELF wave propagation, in which any kinds of inhomogeneities can be included in the analysis, to be compared with the observational results. We show the application of FDTD to our problem and present a few numerical computational results to be compared with those by the pre-existing analysis method.

1. Introduction

Recently there has been again a great interest in subionospheric ELF waves because of the two important findings. The first one is the suggestion by Williams [1] that the global warming which is a very important issue for human being, can be effectively monitored by the intensity of Schumann resonances. Schumann resonance is a global resonance phenomenon in the Earth-ionosphere cavity as shown in Fig. 1, which is triggered by lightning discharges in the thunder-active equatorial region. The resonance frequencies are 8, 14, 21Hz etc. in the ELF range. The second reason is closely associated with the finding of optical phenomena (red sprites etc.) in the mesosphere and the lower ionosphere, and it is found that this mesospheric optical phenomenon is a source of strong ELF signals (called ELF transients) [2]. This ELF transient signal is one of the important tools for the study of those mesospheric optical phenomena and then the electrodynamic coupling between the atmosphere and ionosphere.

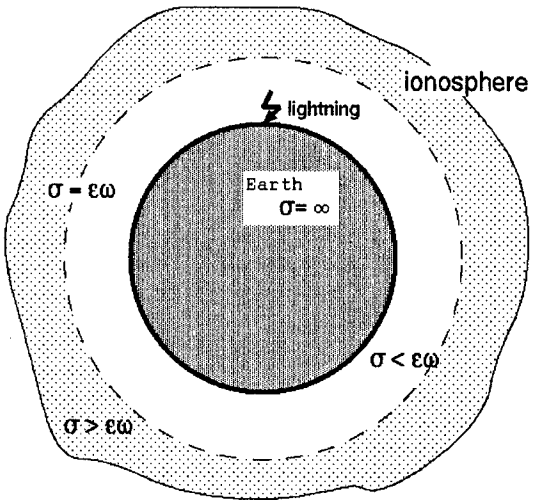

Fig. 1. Configuration of the Earth-ionosphere cavity.

There have been published a few monographs dealing with the subionospheric ELF propagation [3-5]. Schumann [6] was the first to predict the presence of resonances in the spherical earth-ionosphere cavity and suggested a mathematical formulation of the propagation problem at ELF. A great simplification is the presence of only a single globally propagating, zero-order TEM mode [7], while all the higher-order modes attenuate severely at distances of several waveguide effective heights. Despite this simplification, the complex structure of the lower ionosphere imposes an intricate three-dimensional electrodynamical problem that cannot be reduced to practical techniques without certain additional simplifying assumptions. This is the reason why several fundamental observed properties of Schumann resonances cannot be well explained [5,8], and please look at the forthcoming monograph on ELF [8] indicating a lot of unsolved problems in the ELF range. The factors of making the problem very complete are (1) radially (vertically) inhomogeneity of the ionosphere, (2) day-night asymmetry, (3) local ionospheric perturbations etc.

In this sense it is highly required that very complicated situations should be solved in an exact way even by using the numerical methods. If the exact numerical solutions are available for any complicated cavity, it would be possible for us to examine the validity of the previous approximate solutions.

2. Three-dimensional FDTD analysis

The above discussion has led to the requirement for a three-dimensional finite-difference time domain (FDTD) application to our ELF propagation problem in spherical coodinates with azimuthal dependence. Fortunately, this 3D FDTD code has been developed by Holland [9], which can be used in our application. Fig. 2 (right panel) shows the spherical coordinate system (r, θ, ϕ) and location of a unit cell. The left panel of Fig. 2 illustrates the location of field-evaluation points on a unit cell. As shown in Fig. 2, we build a cell entitled I, J and K along each of three axes (r, θ, and ϕ) . In the r direction I = 1 is the starting grid (r = a (Earth's radius) 6.4Mm) and this ground is assumed to be a perfect conductor. I = N_r is the outermost radial boundary, is taken to be r = a + 150 km and to be a perfect conductor. In the θ direction J = 1 is the North Pole (θ = 0°) and J = N_θ is the South Pole (θ = 180°) . The coordinate ϕ indicates the longitude in such a way that K = 1 and K = N_ϕ are the same point, but the latter has encircled the globe. On this condition the six electromagnetic field components are expressed by Holland [9].

The Maxwell's equations to be solved are expressed as follows [10].

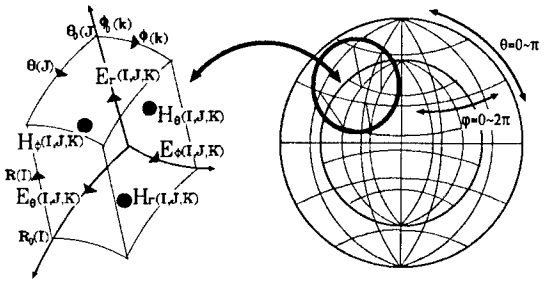

Fig. 2. The spherical coordinate system (r,θ,ϕ) and location of a unit cell (right panel). The left panel illustrates the location of field-evaluation points on the unit cell.

$$\begin{cases} \nabla\times\mathbf{E} = -\mu_0\dfrac{\partial\mathbf{H}}{\partial t} \\ \nabla\times\mathbf{H} = \varepsilon_0\dfrac{\partial\mathbf{E}}{\partial t} + \sigma\mathbf{E} + \mathbf{J}_{ext} \end{cases} \tag{1}$$

where **E** is the electric field, **H** is the magnetic field, ε_0, μ_0 are the dielectric constant and permeability of free space, σ is the conductivity which is a function of space, and $\mathbf{J}_{ext}$ is the current source of the system (here this is a lightning discharge). Here we write down the field updating equations in the spherical coordinates as follows.

In the region of I=1~N_{r-1}, J=2~$N_{\theta-1}$ and K=2~N_ϕ, the field updating equation for E_r component is given by;

$$\begin{aligned} E_r(\mathrm{I,J,K})^{n+1/2} = {} & \frac{\varepsilon_0/\Delta t-\sigma/2}{\varepsilon_0/\Delta t+\sigma/2}E_r(\mathrm{I,J,K})^{n-1/2} + (\varepsilon_0/\Delta t+\sigma/2)^2 \\ & \cdot\left(\frac{1}{R(\mathrm{I})\sin\theta_0(\mathrm{J})}\cdot\left[\frac{\sin\theta(\mathrm{J})H_\phi(\mathrm{I,J,K})^n-\sin\theta(\mathrm{J}-1)H_\phi(\mathrm{I,J-1,K})^n}{\Delta\theta}\right.\right. \\ & \left.\left.-\frac{H_\theta(\mathrm{I,J,K})^n-H_\theta(\mathrm{I,J,K-1})^n}{\Delta\phi}\right]\right) \end{aligned} \tag{2}$$

The corresponding equation for E_θ is as follows.

$$\begin{aligned} E_\theta(\mathrm{I,J,K})^{n+1/2} = {} & \frac{\varepsilon_0/\Delta t-\sigma/2}{\varepsilon_0/\Delta t+\sigma/2}E_\theta(\mathrm{I,J,K})^{n-1/2} + (\varepsilon_0/\Delta t+\sigma/2)^2 \\ & \cdot\left(\frac{1}{R_0(\mathrm{I})}\cdot\left[\frac{H_r(\mathrm{I,J,K})^n-H_r(\mathrm{I,J,K-1})^n}{\sin\theta(J)\Delta\phi}\right.\right. \\ & \left.\left.-\frac{R(\mathrm{I})H_\phi(\mathrm{I,J,K})^n-R(\mathrm{I}-1)H_\phi(\mathrm{I}-1,\mathrm{J,K})^n}{\Delta r}\right]\right) \end{aligned} \tag{3}$$

and this equation pertains to I=1~N_{r-1}, J=2~$N_{\theta-1}$ and K=2~N_ϕ. And then, the field updating equation for E_ϕ component is as follows.

$$E_\phi(\mathrm{I,J,K})^{n+1/2} = \frac{\varepsilon_0/\Delta t - \sigma/2}{\varepsilon_0/\Delta t + \sigma/2} E_\phi(\mathrm{I,J,K})^{n-1/2} + (\varepsilon_0/\Delta t + \sigma/2)^2 \cdot \left(\frac{1}{R_0(\mathrm{I})} \left[\frac{R(I) H_\theta(\mathrm{I,J,K})^n - R(\mathrm{I}-1) H_\theta(\mathrm{I}-1,\mathrm{J,K})^n}{\Delta r} - \frac{H_r(\mathrm{I,J,K})^n - H_r(\mathrm{I,J}-1,\mathrm{K})^n}{\Delta \theta} \right] \right) \quad (4)$$

for I=2~N_{r-1}, J=1~$N_{\theta-1}$ and K=2~N_ϕ. Δr, $\Delta\theta$ and $\Delta\phi$ are the grid size in the r, θ, ϕ directions, and Δt is time step.

The field updating equation for magnetic field components (H_r, H_θ, H_ϕ) are given as follows.

$$H_r(\mathrm{I,J,K})^{n+1} = H_r(\mathrm{I,J,K})^n - \frac{\Delta t}{\mu_0} \left(\frac{1}{R_0(\mathrm{I}) \sin\theta(\mathrm{J})} \left[\frac{\sin\theta_0(\mathrm{J}+1) E_\phi(\mathrm{I,J}+1,\mathrm{K})^{n+1/2} - \sin\theta_0(\mathrm{J}) E_\phi(\mathrm{I,J,K})^{n+1/2}}{\Delta\theta} - \frac{E_\theta(\mathrm{I,J,K}+1)^{n+1/2} - E_\theta(\mathrm{I,J,K})^{n+1/2}}{\Delta\phi} \right] \right) \quad (5)$$

for I=2~N_r, J=1~$N_{\theta-1}$ and K=1~$N_{\phi-1}$.

$$H_\theta(\mathrm{I,J,K})^{n+1} = H_\theta(\mathrm{I,J,K})^n - \frac{\Delta t}{\mu_0} \cdot \left(\frac{1}{R(\mathrm{I})} \left[\frac{E_r(\mathrm{I,J,K}+1)^{n+1/2} - E_r(\mathrm{I,J,K})^{n+1/2}}{\sin\theta_0(\mathrm{J})\Delta\phi} - \frac{R_0(\mathrm{I}+1) E_\phi(\mathrm{I}+1,\mathrm{J,K})^{n+1/2} - R_0(\mathrm{I}) E_\phi(\mathrm{I,J,K})^{n+1/2}}{\Delta r} \right] \right) \quad (6)$$

for I=1~N_{r-1}, J=2~$N_{\theta-1}$ and K=1~$N_{\phi-1}$.

$$H_\phi(\mathrm{I,J,K})^{n+1} = H_\phi(\mathrm{I,J,K})^n - \frac{\Delta t}{\mu_0} \cdot \left(\frac{1}{R(\mathrm{I})} \left[\frac{R(\mathrm{I}+1) E_\theta(\mathrm{I}+1,\mathrm{J,K})^{n+1/2} - R(\mathrm{I}) E_\theta(\mathrm{I,J,K})^{n+1/2}}{\Delta r} - \frac{E_r(\mathrm{I,J}+1,\mathrm{K})^{n+1/2} - E_r(\mathrm{I,J,K})^{n+1/2}}{\Delta\theta} \right] \right) \quad (7)$$

for I=1~N_{r-1}, J=1~$N_{\theta-1}$ and K=1~$N_{\phi-1}$.

The field components are on a modified Yee cell with unit vectors $\hat{r}$, $\hat{\theta}$, and $\hat{\varphi}$, and the corresponding indices I, J, K. Spatial locations are given in term of positions R_0(I), θ_0(J), ϕ_0(K). Points lying midway between these locations are given by R(I), θ(J), ϕ(K).

3. Modeling of conductivity profile and current source, and some numerical examples

In order to verify the usefulness of this 3D FDTD computation, we show some numerical results for a uniform cavity without any day-night asymmetry, because we can compare our own results with the previous analytical computations [11,12]. However, the height profile of the conductivity is definitely induced in our computations.

First we indicate the height profile of the atmospheric conductivity, which is expressed by,

$$\sigma(z) = \sigma_0 \exp(z/h) \quad (8)$$

where z is the height above the ground and h is the scale height (h = 6km). σ_0 is assumed to be

10^{-14}[S/m]. This is a typical profile [10]. Next we assume a lightning discharge current in the form of two exponentials by Bruce and Golde [13], but we adopt a model with much slower time variation than the actual lightning in order to validate the horizontal grid size of 250km.

$$I(t) = I_0\{\exp(-70t) - \exp(-100t)\} \qquad (9)$$

where t is in second. Assuming this current source, we made the FDTD computations in which the grid size in r is 2km, and the grid sizes in θ and ϕ are $\pi/72$ (about 250km).

Fig. 3 illustrates the computational results on the temporal evolution of horizontal magnetic field for four different distances (d = 5, 10, 15 and 20 Mm, indicating the distance in the θ direction) when the current source is located at the equator ($\theta=\pi/2$, $\phi = 0°$). The pulse is generated at $t = 0$ and we can understand the propagation of a pulse in the v waveguide; we notice the direct wave and its corresponding antipodal wave. As you see from this figure, with the increase in propagation distance, the higher frequency components will decay so that we have a spread in waveform for larger propagation distances. The horizontal magnetic field of the antipodal wave is opposite in sign to that of the direct wave, so that the signal for d = 20Mm is zero because of the complete cancellation of the direct and antipodal waves. An important characteristic from this figure is that we expect severe damping between d = 5Mm and 10Mm, but negligible damping between d = 10Mm and 15Mm. These numerical computations are compared with the corresponding computation for their model [11] (the result is shown in Fig. 4), in which there exist some differences in the modeling. The first one is the difference in the input signal (source) because they used a delta function. The sign of the horizontal magnetic field is taken to

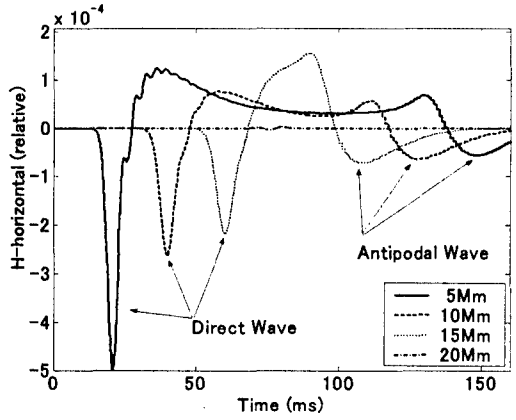

Fig. 4. Computational result of the temporal evolution of horizontal magnetic field for four different propagation distances (d=5, 10, 15 and 20 Mm).

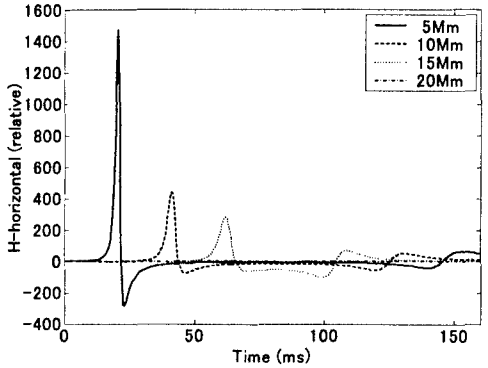

Fig. 3. Same as Fig. 3, but with the previous analytical method[11]. This figure should be compared with Fig. 3.

be oppose to that in this paper. We have found an extremely good similarity between these two figures, suggesting the usefulness of this 3D FDTD analysis in subionospheric ELF propagation. Another difference is definitely due to the difference in propagation constants. They [11] have used a heuristic propagation constant (v_1 and v_2) based on the experimental data,

$$v(f) = v_1 - iv_2 = (f-2)/6 - if/100, \qquad (10)$$

where f is frequency, and v_1, v_2 are real and imaginary part of propagation constant, respectively.

On the other hand, we have used the atmospheric conductivity profile, Eq.(8) as mentioned before. By using the approximate formulas by Greifinger and Greifinger [14], we can estimate the real and imaginary parts of the propagation constant for our ionospheric model. These results are shown in Fig. 5. Fig. 5(a) refers to the real part, while Fig. 5(b) refers to the imaginary part (or attenuation constant) of the propagation constant. The real parts are nearly identical for the two models, but we see a significant difference in the imaginary part (i.e. damping effect). Especially we notice a lot of difference in the attenuation constant at higher frequencies. In the paper [11], they used the heuristic propagation constant, Eq. (10), so that they have not indicated any explicit conductivity height profile. Of course it is theoretically possible for us to obtain the conductivity profile by some approximations from Eq. (10), but this kind of job is not so meaningful. In our next paper we will compare the attenuation from both methods under the same conductivity profile in order to prove the deviation in Fig. 5(b) is caused by different computational models instead of numerical errors.

Finally, we show the last figure for exact comparison between ours and the previous model [11] for the same propagation distance (d=10Mm) in Fig. 6.

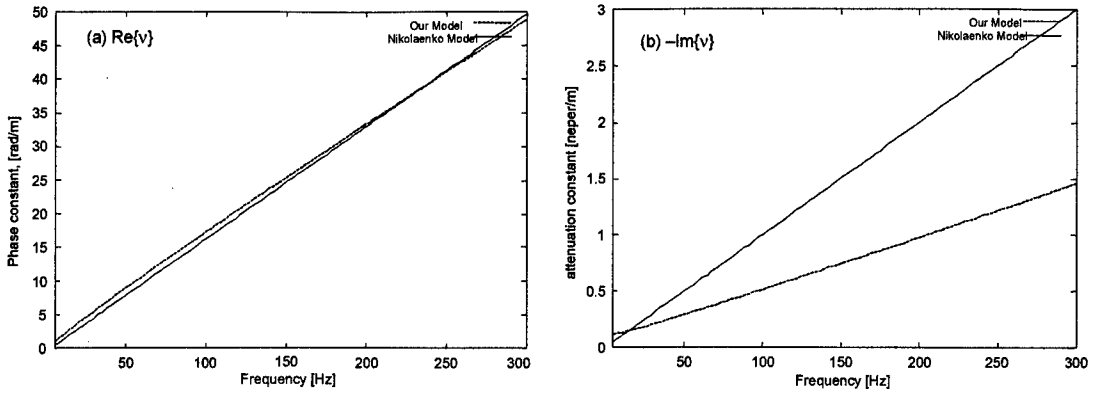

Fig. 5. Comparison of propagation constant. (a) refers to the propagation constant (real part), while (b) the imaginary part, indicating attenuation constant. Two models are compared; our model and Nickolaenko and Hayakawa [11]

4. Conclusions and future application of this FDTD analysis to much more complicated models

In the previous section we have shown only one example of our FDTD analysis for subionospheric ELF propagation and a comparison with the previous analytical solution has indicated that our FDTD application would be of great potential in our future studies. As you see from the above discussion, the field updating mechanism is exactly the same as that of the high-frequency FDTD [16], and it seems that there is no special treatment in the ELF wave analysis. We can list what we will be able to do in this ELF field by means of our FDTD analysis.

As for the ELF propagation itself (such as the propagation of ELF transients (Q bursts, slow tails)), we can study the reflection mechanism of these ELF waves in the lower ionosphere in details by comparing our FDTD results with the previously proposed approximations [14,15].

Then, as for Schumann resonance, there are

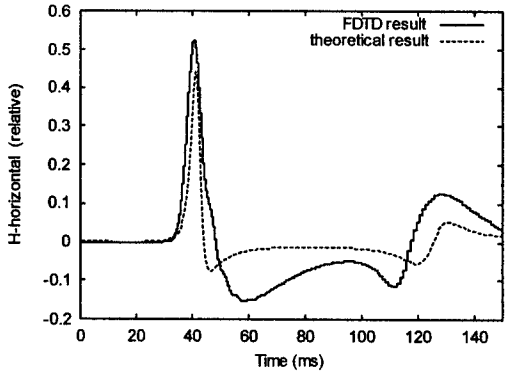

Fig. 6. Comparison of the ELF waveforms for a particular d=10Mm estimated by our method and previous method [11].

several possibilities of the application of our FDTD method. For example, (1) the full consideration of day-night asymmetry in order to well explain the diurnal variation of Schumann resonance intensity and frequencies, (2) the local perturbation (such as the perturbation at high latitudes (auroral regions)).

We will use our FDTD analysis for these above questions in order to improve the physics coming from these subionospheric ELF propagation studies.

REFERENCES

[1] E. R. Williams. The Schumann resonance: A global tropical thermometer. Science, 256, 1184-1187, 1992.

[2] D. J. Boccipio, E. R. Williams, S. J. Heckman, W. A. Lyons, I. T. Baker and R. Boldi. Sprites, ELF transients, and positive ground stroke. Science, 269, 1088-1091, 1995.

[3] J. R. Wait. *Electromagnetic Waves in Stratified Media. Perganion Press*, Oxford, 1962.

[4] J. Galejs. *Terrestrial Propagation of Long Electromagnetic Waves*. Pergamon Press, Oxford, 1972.

[5] P. V. Bliok, A. P. Nikolaenko and Yu. F. Filippov, *Schumann Resonances in the Earth-Ionosphere Cavity*, Peter Pergrinus Ltd., 1980.

[6] W. O. Schumann. On the radiation free self-oscillations of a conducting sphere, which is surrounded by an air layer and an ionospheric shell [in German]. Zeitschrift fur Naturforschung, 7, 149-154, 1952.

[7] T. Madden and W. Thompson. Low frequency electromagnetic oscillations of Earth-ionosphere cavity. Rev. Geophys., 3, 211-254, 1965.

[8] A. P. Nickolaenko and M. Hayakawa, *Resonances in the Earth-Ionosphere Cavity*, Kluwer Academic Publishers, Dordrecht, 2002.

[9] R. Holland. THREDS: A finite-difference time-domain EMP code in 3D spherical coordinates.

IEEE Trans. Nuclear Science, NS-30(6), 4592-4595, 1983.

[10] D. D. Sentman. Schumann resonances. In Handbook of Atmospheric Electrodynamics, Ed. by H. Volland, vol. 1, 267-310, CRC Press, 1995.

[11] A. P. Nickolaenko and M. Hayakawa. Natural electromagnetic pulses in the ELF range. Geophys. Res. Lett., 25(16), 3103-3106, 1998.

[12] A. P. Nickolaenko, M. Hayakawa, I. G. Kudintseva, S. V. Myand and L. M. Rabinowicz. ELF sub-ionospheric pulse in time domain, Geophys. Res. Lett., 26(7), 999-1002, 1999.

[13] C. E. R. Bruce and R. H. Golde. The lightning discharge. J. Inst. Electr. Eng., 88, 487, 1941.

[14] C. Greifinger and P. Greifinger. Approximate method for determining ELF eigenvalues in the earth-ionosphere waveguide. Radio Science, 13, 831, 1978.

[15] V. C. Mushtak and E. R. Williams. ELF propagation parameters for uniform models of the Earth-ionosphere waveguide. J. Atmos. Soler-terr. Phys., 18, 1989-2001, 2002.

[16] K.Kunz and R.J. Luebbers. *The Finite Difference Time Domain Method for Electromagnetics*, CRC Press, Boca Raton, USA, 1993.

Masashi Hayakawa obtained Bachelor degree, Master degree from Nagoya University in 1966 and 1968, respectively. Doctor of Engineering from the same university in 1974. In 1970 he joined Research Institute of Atmospherics of Nagoya University as a Research Associate, and become Assistant and Associate Professors there. Since 1991 he has been a professor of the University of Electro-Communications and has been working on space physics, atmospheric electricity, seismo-electromagnetics, EMC, inversion problem. He was URSI Commission E chair (1996-1999), and he is now co-editor of Radio Science. IEICE, AGU, URSI member.

Takuya Otsuyama obtained Bachelor degree, Master degree from University of Electro-Communications in 1996 and 1998, respectively. And he obtained Doctor of Engineering from the same university in 2002. He has been working on upper atmosphere discharge and Trimpi phenomena. He joined Sankosha Co. and is working on lightning detection and application.

CALL FOR CEM COMPUTER MODELING & SIMULATION DEMONSTRATIONS FOR THE 2003 ACES CONFERENCE, MONTEREY, CA

CHAIR

Andrew L. Drozd

andro1@aol.com

This new session is devoted to illustrating fundamental CEM modeling and simulation (M&S) concepts and methods through a series of interactive computer demonstrations of simple canonical-type problems. These include the application of the moment method (MoM), uniform theory of diffraction (UTD) and variations on the asymptotic ray tracing method, finite difference time-domain (FDTD), finite element modeling (FEM), transmission line (TL) theory, and other useful methods. The demonstrations will be conducted using general-purpose codes to illustrate the M&S concepts and approaches.† Hands-on participation during the demonstrations is encouraged. The demonstrations will cover, but not be limited to the following topics:

- Shielding Effectiveness Simulation Using the FDTD Method
- Modeling the Shielding Effectiveness Using Integral Equation Techniques
- Large Complex System Analysis Using MLFMA
- System-Level EMC Antenna Coupling Analysis for Large, Complex Structure Topologies Using Multi-Fidelity Modeling and Simulation Methods
- EMC Simulation Techniques for Printed Circuit Boards
- Power and Ground Voltage Fluctuations and Effects of Decoupling Capacitors on PCBs
- FDTD Modeling of DC Power-Busses
- FEM Analysis of Printed Circuit Board Signal Coupling
- Model Validation for Electromagnetic Codes
- Visualization of Fields
- Complex Coupling Phenomena
- Modeling Using the PEEC Method.

If you are interested in having a demonstration considered, please provide a title of the proposed demonstration, name/affiliation, and 50-word abstract by no later than 15 January 2003 to Andrew L. Drozd c/o ANDRO Computational Solutions, Beeches Technical Campus, Bldg. 3, Suite 4, 7902 Turin Road, Route 26N, Rome, NY 13440.
Tel.: (877) 334-1188, Fax: 315.334.1397, Email: andro1@aol.com.

Please note that presenters will be required to bring their own laptop computers. Arrangements can be made with the Chair for use of other A/V aids.

---

† The ACES does not specifically endorse any software code, tool, or technique used in any of the demonstrations.

2002 INSTITUTIONAL MEMBERS

ANDREW CORPORATION
10500 W. 153rd Street
Orland Park, IL 60462

AUSTRALIAN DEFENCE LIB.
Northcott Drive
Campbell, A.C.T. 2600 AUSTRALIA

BAE SOWERBY RESEARCH CTR.
FPC 267 Po Box 5
Filton, Bristol, BS134 7QW UK

BAE SYSTEMS, LIB.
W. Hanningfield
Chelmsford CM2 9HN UK

BOEING NORTH AMERICAN SVCS
1200 Wilson Blvd.
Arlington, VA 22209

CENTER HP COMPUTING
PO Box 830657
Birmingham, AL 35283-0657

CHALMERS UNIV of TECHNOLOGY
Dept of Microwave Technology
Gothenburg, S 41296 SWEDEN

CULHAM EM
Bldg F5, Culham
Abingdon, Oxford, OX14 3ED UK

DARTMOUTH COLL-FELDBERG LIB
6193 Murdough Center
Hanover, NH 03755-3560

DEFENCE RESEARCH ESTAB. LIB.
3701 Carling Avenue
Ottowa, ON, K1A 0Z4 CANADA

ERICSSON SAAB
Gelbgjutaregat
Linkoping, SE 58188 SWEDEN

ETSE TELECOMUNICACION
Biblioteca, Campus Lagoas
Vigo, 36200 SPAIN

FACOLTA INGEGNERIA
Library, Via G Duranti 89
Perugia, 06125 ITALY

FANFIELD LTD
Braxted Park
Witham, Essex, CM8 3XB UK

GEORGIA TECH LIBRARY
225 North Avenue, NW
Atlanta, GA 30332-0001

HKUST, UNIVERSITY LIBRARY
Clear Water Bay Road
Kowloon, HONG KONG

HRL LABS, RESEARCH LIBRARY
3011 Malibu Canyon
Malibu, CA 90265

IIT RESEARCH INSTITUTE
185 Admiral Cochrane Drive
Annapolis, MD 21401-7396

INFO & LIBRARY SERVICE
Private Bag 37
Clayton, Vic, 3168 AUSTRALIA

INSYS LTD.
Reddings Wood, Ampthill
Bedford, MK45 2HD UK

IPS RADIO & SPACE SVC/LIBRARY
PO Box 5606
W. Chatswood, 2057 AUSTRALIA

L-3 COMMUNICATIONS
130 Constitution
Menlo Park, CA 94025

LINDA HALL LIBRARY
5109 Cherry Street
Kansas City, MO 64110-2498

MISSISSIPPI STATE UNIV LIBRARY
PO Box 9570
Mississippi State, MS 39762

MITRE CORPORATION LIBRARY
202 Burlington Road
Bedford, MA 01730-1407

NATL GROUND INTELLIGENCE
220 7th Street N.E.
Charlottesville, VA 22902-5307

NATL RADIOLOGICAL PROT. BD.
Chilton, Didcot, OXON,
OX11 0RG UK

NAVAL RESEARCH LABORATORY
C. Office
Washington, DC 20375

PENN STATE UNIVERSITY
126 Paterno Library
University Park, PA 16802-1808

PHILIPS RESEARCH LAB LIBRARY
Cross Oak Lane, Salfords
Redhill, RH1 5HA SURREY UK

QINETIQ INFORMATION CTR.
Ively Road
Farnsborough, HANT, GU14 OLX UK

RENTON TECH LIBRARY/BOEING
PO BOX 3707
SEATTLE, WA 98124-2207

QUEENSLAND CENTER, LIBRARY
2643 Moggill Road
Brisbane, QLD, 4069 AUSTRALIA

SOUTHWEST RESEARCH INST.
6220 Culebra Road
San Antonio, TX 78238

SWETS BLACKWELL
440 Creamery Way, Suite A
Exton, PA 19341

TDK CORP.
2-15-7 Higashi-oh, Ciba
Ciba, 272 8558 JAPAN

TECHNISCHE UNIV. DELFT
Mekelweg 4, Delft, Holland, 2628 CD
NETHERLANDS

TELSTRA RES. LABS LIBRARY
770 Blackburn Road
Clayton, VIC, 3168 AUSTRALIA

TOKYO UNIV OF TECHNOLOGY
1404 ñ1 Katakura, Hachioji
Tokyo, 192-0982 JAPAN

UNIV OF CENTRAL FLORIDA LIB.
PO Box 162666
Orlando, FL 32816-2440

UNIV OF COLORADO LIBRARY
Campus Box 184
Boulder, CO 80309-0184

UNIV OF MISSOURI-ROLLA LIB.
1870 Miner Circle
Rolla, MO 65409-0001

US ARMY COLD REGION RES, LIB.
72 Lyme Road
Hanover, NH 03775-1290

ACES COPYRIGHT FORM

This form is intended for original, previously unpublished manuscripts submitted to ACES periodicals and conference publications. The signed form, appropriately completed, MUST ACCOMPANY any paper in order to be published by ACES. PLEASE READ REVERSE SIDE OF THIS FORM FOR FURTHER DETAILS.

TITLE OF PAPER:

AUTHORS(S)

PUBLICATION TITLE/DATE:

RETURN FORM TO:

Dr. Atef Z. Elsherbeni
University of Mississippi
Dept. of Electrical Engineering
Anderson Hall Box 13
University, MS 38677 USA

PART A - COPYRIGHT TRANSFER FORM

(NOTE: Company or other forms may not be substituted for this form. U.S. Government employees whose work is not subject to copyright may so certify by signing Part B below. Authors whose work is subject to Crown Copyright may sign Part C overleaf).

The undersigned, desiring to publish the above paper in a publication of ACES, hereby transfer their copyrights in the above paper to The Applied Computational Electromagnetics Society (ACES). The undersigned hereby represents and warrants that the paper is original and that he/she is the author of the paper or otherwise has the power and authority to make and execute this assignment.

Returned Rights: In return for these rights, ACES hereby grants to the above authors, and the employers for whom the work was performed, royalty-free permission to:

1. Retain all proprietary rights other than copyright, such as patent rights.
2. Reuse all or portions of the above paper in other works.
3. Reproduce, or have reproduced, the above paper for the author's personal use or for internal company use provided that (a) the source and ACES copyright are indicated, (b) the copies are not used in a way that implies ACES endorsement of a product or service of an employer, and (c) the copies per se are not offered for sale.
4. Make limited distribution of all or portions of the above paper prior to publication.
5. In the case of work performed under U.S. Government contract, ACES grants the U.S. Government royalty-free permission to reproduce all or portions of the above paper, and to authorize others to do so, for U.S. Government purposes only.

ACES Obligations: In exercising its rights under copyright, ACES will make all reasonable efforts to act in the interests of the authors and employers as well as in its own interest. In particular, ACES REQUIRES that:

1. The consent of the first-named author be sought as a condition in granting re-publication permission to others.
2. The consent of the undersigned employer be obtained as a condition in granting permission to others to reuse all or portions of the paper for promotion or marketing purposes.

In the event the above paper is not accepted and published by ACES or is withdrawn by the author(s) before acceptance by ACES, this agreement becomes null and void.

AUTHORIZED SIGNATURE — TITLE (IF NOT AUTHOR)

EMPLOYER FOR WHOM WORK WAS PERFORMED — DATE FORM SIGNED

Part B - U.S. GOVERNMENT EMPLOYEE CERTIFICATION

(NOTE: if your work was performed under Government contract but you are not a Government employee, sign transfer form above and see item 5 under Returned Rights).

This certifies that all authors of the above paper are employees of the U.S. Government and performed this work as part of their employment and that the paper is therefor not subject to U.S. copyright protection.

AUTHORIZED SIGNATURE — TITLE (IF NOT AUTHOR)

NAME OF GOVERNMENT ORGANIZATION — DATE FORM SIGNED

PART C - CROWN COPYRIGHT

(NOTE: ACES recognizes and will honor Crown Copyright as it does U.S. Copyright. It is understood that, in asserting Crown Copyright, ACES in no way diminishes its rights as publisher. Sign only if *ALL* authors are subject to Crown Copyright).

This certifies that all authors of the above Paper are subject to Crown Copyright. (Appropriate documentation and instructions regarding form of Crown Copyright notice may be attached).

AUTHORIZED SIGNATURE | TITLE OF SIGNEE

NAME OF GOVERNMENT BRANCH | DATE FORM SIGNED

Information to Authors

ACES POLICY

ACES distributes its technical publications throughout the world, and it may be necessary to translate and abstract its publications, and articles contained therein, for inclusion in various compendiums and similar publications, etc. When an article is submitted for publication by ACES, acceptance of the article implies that ACES has the rights to do all of the things it normally does with such an article.

In connection with its publishing activities, it is the policy of ACES to own the copyrights in its technical publications, and to the contributions contained therein, in order to protect the interests of ACES, its authors and their employers, and at the same time to facilitate the appropriate re-use of this material by others.

The new United States copyright law requires that the transfer of copyrights in each contribution from the author to ACES be confirmed in writing. It is therefore necessary that you execute either Part A-Copyright Transfer Form or Part B-U.S. Government Employee Certification or Part C-Crown Copyright on this sheet and return it to the Managing Editor (or person who supplied this sheet) as promptly as possible.

CLEARANCE OF PAPERS

ACES must of necessity assume that materials presented at its meetings or submitted to its publications is properly available for general dissemination to the audiences these activities are organized to serve. It is the responsibility of the authors, not ACES, to determine whether disclosure of their material requires the prior consent of other parties and if so, to obtain it. Furthermore, ACES must assume that, if an author uses within his/her article previously published and/or copyrighted material that permission has been obtained for such use and that any required credit lines, copyright notices, etc. are duly noted.

AUTHOR/COMPANY RIGHTS

If you are employed and you prepared your paper as a part of your job, the rights to your paper initially rest with your employer. In that case, when you sign the copyright form, we assume you are authorized to do so by your employer and that your employer has consented to all of the terms and conditions of this form. If not, it should be signed by someone so authorized.

NOTE RE RETURNED RIGHTS: Just as ACES now requires a signed copyright transfer form in order to do "business as usual", it is the intent of this form to return rights to the author and employer so that they too may do "business as usual". If further clarification is required, please contact: The Managing Editor, R. W. Adler, Naval Postgraduate School, Code EC/AB, Monterey, CA, 93943, USA (408)656-2352.

Please note that, although authors are permitted to re-use all or portions of their ACES copyrighted material in other works, this does not include granting third party requests for reprinting, republishing, or other types of re-use.

JOINT AUTHORSHIP

For jointly authored papers, only one signature is required, but we assume all authors have been advised and have consented to the terms of this form.

U.S. GOVERNMENT EMPLOYEES

Authors who are U.S. Government employees are not required to sign the Copyright Transfer Form (Part A), but any co-authors outside the Government are.

Part B of the form is to be used instead of Part A only if all authors are U.S. Government employees and prepared the paper as part of their job.

NOTE RE GOVERNMENT CONTRACT WORK: Authors whose work was performed under a U.S. Government contract but who are not Government employees are required so sign Part A-Copyright Transfer Form. However, item 5 of the form returns reproduction rights to the U. S. Government when required, even though ACES copyright policy is in effect with respect to the reuse of material by the general public.
January 2002

APPLIED COMPUTATIONAL ELECTROMAGNETICS SOCIETY JOURNAL
http://aces.ee.olemiss.edu

INFORMATION FOR AUTHORS

PUBLICATION CRITERIA

Each paper is required to manifest some relation to applied computational electromagnetics. **Papers may address general issues in applied computational electromagnetics, or they may focus on specific applications, techniques, codes, or computational issues.** While the following list is not exhaustive, each paper will generally relate to at least one of these areas:

1. **Code validation.** This is done using internal checks or experimental, analytical or other computational data. Measured data of potential utility to code validation efforts will also be considered for publication.

2. **Code performance analysis.** This usually involves identification of numerical accuracy or other limitations, solution convergence, numerical and physical modeling error, and parameter tradeoffs. However, it is also permissible to address issues such as ease-of-use, set-up time, run time, special outputs, or other special features.

3. **Computational studies of basic physics.** This involves using a code, algorithm, or computational technique to simulate reality in such a way that better, or new physical insight or understanding, is achieved.

4. **New computational techniques**, or new applications for existing computational techniques or codes.

5. **"Tricks of the trade"** in selecting and applying codes and techniques.

6. **New codes, algorithms, code enhancement, and code fixes.** This category is self-explanatory, but includes significant changes to existing codes, such as applicability extensions, algorithm optimization, problem correction, limitation removal, or other performance improvement. **Note: Code (or algorithm) capability descriptions are not acceptable, unless they contain sufficient technical material to justify consideration.**

7. **Code input/output issues.** This normally involves innovations in input (such as input geometry standardization, automatic mesh generation, or computer-aided design) or in output (whether it be tabular, graphical, statistical, Fourier-transformed, or otherwise signal-processed). Material dealing with input/output database management, output interpretation, or other input/output issues will also be considered for publication.

8. **Computer hardware issues.** This is the category for analysis of hardware capabilities and limitations of various types of electromagnetics computational requirements. Vector and parallel computational techniques and implementation are of particular interest.

Applications of interest include, but are not limited to, antennas (and their electromagnetic environments), networks, static fields, radar cross section, shielding, radiation hazards, biological effects, electromagnetic pulse (EMP), electromagnetic interference (EMI), electromagnetic compatibility (EMC), power transmission, charge transport, dielectric, magnetic and nonlinear materials, microwave components, MEMS technology, MMIC technology, remote sensing and geometrical and physical optics, radar and communications systems, fiber optics, plasmas, particle accelerators, generators and motors, electromagnetic wave propagation, non-destructive evaluation, eddy currents, and inverse scattering.

Techniques of interest include frequency-domain and time-domain techniques, integral equation and differential equation techniques, diffraction theories, physical optics, moment methods, finite differences and finite element techniques, modal expansions, perturbation methods, and hybrid methods. This list is not exhaustive.

A unique feature of the Journal is the publication of unsuccessful efforts in applied computational electromagnetics. Publication of such material provides a means to discuss problem areas in electromagnetic modeling. Material representing an unsuccessful application or negative results in computational electromgnetics will be considered for publication only if a reasonable expectation of success (and a reasonable effort) are reflected. Moreover, such material must represent a problem area of potential interest to the ACES membership.

Where possible and appropriate, authors are required to provide statements of quantitative accuracy for measured and/or computed data. This issue is discussed in "Accuracy & Publication: Requiring, quantitative accuracy statements to accompany data," by E. K. Miller, *ACES Newsletter,* Vol. 9, No. 3, pp. 23-29, 1994, ISBN 1056-9170.

EDITORIAL REVIEW

In order to ensure an appropriate level of quality control, papers are refereed. They are reviewed both for technical correctness and for adherence to the listed guidelines regarding information content.

JOURNAL CAMERA READY SUBMISSIN DATES

March issue	deadline 8 January
July issue	deadline 20 May
November issue	deadline 20 September

Uploading an acceptable camera ready article after the deadlines will result in a delay in publishing this article.

STYLE FOR CAMERA-READY COPY

The ACES Journal is flexible, within reason, in regard to style. However, certain requirements are in effect:

1. The paper title should NOT be placed on a separate page. The title, author(s), abstract, and (space permitting) beginning of the paper itself should all be on the first page. The title, author(s), and author affiliations should be centered (center-justified) on the first page.

2. An abstract is REQUIRED. The abstract should be a brief summary of the work described in the paper. It should state the computer codes, computational techniques, and applications discussed in the paper (as applicable) and should otherwise be usable by technical abstracting and indexing services.

3. Either British English or American English spellings may be used, provided that each word is spelled consistently throughout the paper.

4. Any commonly-accepted format for referencing is permitted, provided that internal consistency of format is maintained. As a guideline for authors who have no other preference, we recommend that references be given by author(s) name and year in the body of the paper (with alphabetical listing of all references at the end of the paper). Titles of Journals, monographs, and similar publications should be in italic font or should be underlined. Titles of papers or articles should be in quotation marks.

5. Internal consistency shall also be maintained for other elements of style, such as equation numbering. As a guideline for authors who have no other preference, we suggest that equation numbers be placed in parentheses at the right column margin.

6. The intent and meaning of all text must be clear. For authors who are NOT masters of the English language, the ACES Editorial Staff will provide assistance with grammar (subject to clarity of intent and meaning).

7. Unused space should be minimized. Sections and subsections should not normally begin on a new page.

MATERIAL, SUBMITTAL FORMAT AND PROCEDURE

The preferred format for submission and subsequent review, is 12 point font or 12 cpi, double line spacing and single column per page. All submissions should be uploaded to ACES server through ACES web site (http://aces.ee.olemiss.edu) by using the upload button, journal section. Only pdf files are accepted for submission. The file size should not be larger than 5MB, otherwise permission from the Editor-in-Chief should be obtained first. The Editor-in-Chief will acknowledge the electronic submission a few minutes after the upload process is successfully completed

Only camera-ready electronic files are accepted for publication. The term **"camera-ready" means that the material is neat, legible, and reproducible.** The preferred style is Times Roman 10 point (or equivalent) such as that used in this text. A double column format similar to that used here is required. Full details can be found on ACES site, Journal section.

ACES reserves the right to edit any uploaded material, however, this is not generally done. It is the author(s) responsibility to provide acceptable camera ready pdf files. Incompatible or incomplete pdf files will not be processed, and authors will be requested to re-upload revised acceptable version.

COPYRIGHTS AND RELEASES

Each primary author must sign a copyright form and obtain a release from his/her organization vesting the copyright with ACES. Copyright forms are available at ACES, web site (http://aces.ee.olemiss.edu). To shorten the review process time, the executed copyright form should be forwarded to the Editor-in-Chief immediately after the completion of the upload (electronic submission) process. Both the author and his/her organization are allowed to use the copyrighted material freely for their own private purposes.

Permission is granted to quote short passages and reproduce figures and tables from and ACES Journal issue provided the source is cited. Copies of ACES Journal articles may be made in accordance with usage permitted by Sections 107 or 108 of the U.S. Copyright Law. This consent does not extend to other kinds of copying, such as for general distribution, for advertising or promotional purposes, for creating new collective works, or for resale. The reproduction of multiple copies and the use of articles or extracts for commercial purposes require the consent of the author and specific permission from ACES. Institutional members are allowed to copy any ACES Journal issue for their internal distribution only.

PUBLICATION CHARGES

ACES members are allowed 12 printed pages per paper without charge; non-members are allowed 8 printed pages per paper without charge. Mandatory page charges of $75 a page apply to all pages in excess of 12 for members or 8 for non-members. Voluntary page charges are requested for the free (12 or 8) pages, but are NOT mandatory or required for publication. A priority courtesy guideline, which favors members, applies to paper backlogs. Authors are entitled to 15 free reprints of their articles and must request these from the Managing Editor. Additional reprints are available to authors, and reprints available to non-authors, for a nominal fee.

ACES Journal is abstracted in INSPEC, in Engineering Index, and in DTIC.